SPIN MANIPULATION IN FUNCTIONAL MATERIALS: STUDY FROM FIRST PRINCIPLES

Thesis

Submitted in partial fulfillment of the requirements for the degree of

DOCTOR OF PHILOSOPHY

by

Indukuru Ramesh Reddy

DEPARTMENT OF PHYSICS

NATIONAL INSTITUTE OF TECHNOLOGY KARNATAKA

SURATHKAL, MANGALORE - 575025

March, 2021

To my family

DECLARATION

By the Ph.D. Research Scholar

I hereby *declare* that the Research Thesis entitled **SPIN MANIPULATION IN FUNCTIONAL MATERIALS: STUDY FROM FIRST PRINCIPLES** which is being submitted to the **National Institute of Technology Karnataka, Surathkal** in partial fulfillment of the requirements for the award of the Degree of **Doctor of Philosophy** in **Physics** is a *bonafide report of the research work carried out by me* under the guidence of Dr. Kartick Tarafder, Assistant Professor, Department of Physics, National Institute of Technology Karnataka, Surathkal. The material contained in this Research Thesis has not been submitted to any University or Institution for the award of any degree.

Rameshreddy
Indukuru Ramesh Reddy
Reg. No.: 165082 PH16F04
Department of Physics

Place: NITK, Surathkal.
Date: March 12, 2021

CERTIFICATE

This is to *certify* that the Research Thesis entitled **SPIN MANIPULATION IN FUNCTIONAL MATERIALS: STUDY FROM FIRST PRINCIPLES** submitted by **Indukuru Ramesh Reddy**, (Reg. No.: 165082 PH16F04) as the record of the research work carried out by him, is *accepted as the Research Thesis submission* in partial fulfillment of the requirements for the award of degree of **Doctor of Philosophy**.

(Dr. Kartick Tarafder)
Research Supervisor

Chairman - DRPC

ASSOCIATE PROFESSOR & HEAD
Physics Department
NITK Surathkal, Mangalore-575025
KARNATAKA

ACKNOWLEDGMENTS

At the end of my Ph.D, I would like to take the opportunity to express my heartfelt appreciation to all those people who made this possible for me. First of all, I would like to express my sincere gratitude to my supervisor Dr. Kartick Tarafder for his guidance, endless enthusiasm, and constant push at every step which helped me to successfully conclude my thesis. He has given ample freedom to carry out research on my own and also provided generous support at challenging times, both academically and personally. It has been my privilege to work with him. Apart from regular discussions on research, I have had a great time with him at our particular tea point.

I would like to thank Professor Peter M. Oppeneer for useful discussions and suggestions. I feel privileged to start my research life under the mentorship of Dr. Rajeev Shesha Joshi. Thank you, Rajeev, for always being there as my dear friend. Thank you very much for your encouragement and support.

I am fortunate to have Manju, Prashanth, Chenna Keshav, Sai Srikar, Ashok, Swetalin, as my friends, and I really appreciate their care and support. I would like to thank Ramana Reddy, Raveendra Kiran, Srijyothi, Naveen Reddy, Sruthi and Vijay for making my stay comfortable and creating the lively environment at the NITK campus.

Above all, I would like to thank the special person with whom I share all my good and bad moments. Thank you, Swathi, for all your love and support.

I wish to express my gratitude to my uncle B. V. Ramana Reddy for his unconditional moral and financial support to pursue my higher studies, thank you so much, Venky Mama. I owe a lot to my family, especially my parents and grandparents, for their boundless support and encouragement. I would like to thank my sister and my brother-in-law for taking care of my parents in my absence.

Place: NITK, Surathkal — Indukuru Ramesh Reddy

Date: March 12, 2021

ABSTRACT

The thesis investigates an intriguing phenomenon, namely the Spin Crossover (SCO) that has recently been observed in many functional materials. A detailed theoretical investigation of SCO phenomena in newly synthesized materials has been carried out by employing first-principles density functional theory +U calculations. The spin state switching of a class of square-planar magnetic molecules and their interactions to the metal surfaces has been investigated. The SCO triggered by an electric polarization was observed in the perovskite Sr_2CoO_3F (SCOF) system. In a hybrid perovskite heterostructure, where SCOF is sandwiched between two ferroelectric $BaTiO_3$ (BTO) layers, the spin state of the Co atom in SCOF can be switched systematically from a high-spin to a low-spin by altering the polarization direction of the BTO with respect to SCOF. A giant magnetoelectric coupling has also been observed in this system. Pressure-driven SCO has been observed in Hofmann clathrate, namely ($Fe\{OS(CH_3)_2\}_2\{Ag(CN)_2\}_2$), while applying the hydrostatic pressure. The study shows that under a relatively low isotropic hydrostatic pressure, the complex exhibits a reversible spin switching. The investigation reveals that the system undergoes a structural phase transition when the pressure is anisotropic. The transition pressure for the spin-state transition and structural transformation has been estimated from first-principles calculations. In the final stage of this work, the spin crossover in metal-organic molecules and their interactions with magnetic metal substrates have been investigated. The structural, electronic, and magnetic properties of Ni-quinonoid and Ni-dinuclear molecules have been studied upon adsorption on Co(001) substrate. The study shows that these molecules undergo a spin state switching when they adsorbed on the Co(001) surface. The exchange couplings between the magnetic centers are carefully investigated. Further, the spin state and magnetic anisotropy energy of Ni atom in the Ni-dinuclear molecule adsorbed on a Co(001) substrate has tailored by using adatom as an axial ligand to the central transition metal (TM) atoms in the molecule.

Keywords: Spin crossover, Spin state transition, Spin-interface, Hofmann clathrate, Perovskite oxide/oxyhalide, TM-quinonoid, Magneto-chemical method, Magnetoelectric coupling, Magnetic anisotropy energy.

Contents

Abstract i

List of Figures vi

List of Tables xiv

Acronyms and Abbreviations xvi

List of Symbols xix

1 Introduction **1**

1.1 Spin Crossover 5

1.1.1 Crystal Field Theory vs Molecular Orbital Theory 6

1.1.2 Types of SCO Behavior 8

1.1.3 Potential Applications of Spin Crossover Materials 9

1.2 Types of SCO Materials 10

1.3 Perovskite Oxide Materials 10

1.3.1 Perovskite Oxyhalides 14

1.4 Metal-Organic Frameworks 18

1.4.1 Hofmann-Type Like Complexes 19

1.5 Single Molecule Spintronics 20

1.5.1 Behavior of Organic Molecules at Interface 23

1.5.2 Spinterface 24

1.5.3 Advantages of Organic Molecules for Spintronics 27

1.6 Scope and Objectives of the Proposed Work 28

1.7 Overview of Present Thesis 30

2 Computational Methodology **33**

2.1 First-Principles Calculations 33

2.2 Many-body Hamiltonian 34

2.3 Basics of Density Functional Theory 38

2.3.1 The Hohenberg-Kohn Theorems 39

2.3.2 The Kohn-Sham Formalism 42

2.4 Exchange-Correlation 45

2.4.1 E_{XC} - Approximations 46

2.4.2 Local Density Approximation (LDA) 47

2.4.3 Generalized Gradient Approximation (GGA) 48

2.4.4 Hybrid Functionals 49

2.4.5 Beyond LDA/GGA: LDA+U/GGA+U 50

2.5 The Plane Wave and Pseudopotential Implementation of DFT 52

2.5.1 Bloch's theorem 52

2.5.2 Kohn-Sham Equations in Plane Wave Form 52

2.5.3 Pseudopotentials 53

2.5.4 The Projector Augmented Wave Method 56

2.6 Technical Aspects 57

3 Route to Achieving Giant Magnetoelectric Coupling in $BaTiO_3/Sr_2CoO_3F$ Perovskite Heterostructures 59

3.1 Introduction 59

3.2 Computational Details 62

3.3 Results and Discussions 63

3.3.1 Heterostructure geometries 63

3.3.2 Magnetoelectric Coupling Coefficient (α_s) 64

3.3.3 Electronic Structure 66

3.4 Conclusion 70

4 Pressure-Driven Structural and Spin State Transition in a Hofmann Clathrate Coordination Polymer 71

4.1 Introduction 71

4.2 Computational Details 73

4.3 Results and Discussions 74

4.3.1 Optimized Crystal structure 74

4.3.2 Electronic Structure and Density of States 79

4.4 Conclusions 82

5 Interfacial Spin Manipulation of Nickel-Quinonoid Complex Adsorbed on Co(001) Substrate 83

5.1 Introduction 83

5.2 Computational Details 86

5.3 Results and Discussions 87

5.3.1 Optimized Geometry 87

5.3.2 Electronic Structure and Magnetic Properties 90

5.4 Conclusions 95

6 Unprecedented Magnetic Interaction of Chemisorbed Ni^{II}-Dinuclear Quinonoid Molecule on a Co(001) Substrate 97

6.1 Introduction 97

6.2 Computational Details 98

6.3 Results and Discussions 100

6.3.1 Magnetic Anisotropy Energy 106

6.4 Conclusions 107

7 Summary and Outlook 109

A Physisorption of Nickel-Quinonoid Complex on Co(001) Substrate 113

Bibliography 115

List of Figures

1.1 Schematic representation of the SCO phenomena of a molecular system, where various external perturbations (pressure, temperature, light irradiation, magneto-chemical method, magnetic field) drive the change in the magnetic moment (M) or spin state. 4

1.2 Schematic representation of the HS state (left) and LS state (right) of an octahedral complex of d^6 configuration materials. 6

1.3 Different types of SCO behavior in terms of the molar fraction of HS molecules (γ_{HS}) as a function of external perturbation is represented schematically, **(a)** gradual, **(b)** abrupt, **(c)** hysteretic, **(d)** multi-step, and **(e)** incomplete. 8

1.4 A schematic picture illustrating the structure of the perovskite oxides in the centre, where the A, B and O atoms are represented by green, blue, and red spheres, respectively. Also, demonstrating the various properties of complex perovskite oxides. Figure adapted from Zubko, P. *et al.*, Annu. Rev. Condens. Matter Phys., 2(1):141-165 (2011). . . . 12

1.5 The evolution of crystal field splitting energy (CFSE) of a transition metal cation on the choice of anion and anion concentration in octahedral coordination. **(a)** and **(b)** The CFSE under a tetragonal distortion within a specific octahedral configuration for trans-[MO_4F_2] and trans-$_4N_2$, respectively, and the corresponding octahedral configurations are illustrated in the respective graphs. **(c)** The CFSE for a transition metal cation in the octahedral coordination, MO_xF_{6-x} (x=1-6) with varying anion concentration (or configuration) and without bond distortions. Figure adapted from Harada, J. K. *et al.*, Advanced Materials, 31(19):1805295 (2019). 16

1.6 Representative view of 2D and 3D Hofmann clathrates. **(a)** A 2D Hofmann clathrate [Fe(3-Fpy)$_2$Pt^{II}(CN)$_4$] (3-Fpy: 3-fluoropyridine) and **(b)** a 3D Hofmann clathrate [Fe(pz)Pt^{II}(CN)$_4$] (pz: pyrazine). Fe, Pt, N and C atoms are represented with green, light blue, blue and black color spheres, respectively. The Hydrogen atoms are not shown in the figure for clarity. Figure adapted from Polyzou, C. D. & Tangoulis, V., Journal of Coordination Chemistry, 72(3):389-418 (2019) (Polyzou and Tangoulis, 2019). 20

1.7 Schematic representation of the molecular device with graphene electrodes, where the TbPc$_2$ single-ion magnet located in the junction. A lateral gate electrode approaches the nano-gap. Figure adapted from Lumetti, S. *et al.*, Dalton Transactions, 45:16570-16574 (2016). 21

1.8 Illustration of the behavior of **(a)** an inorganic material at the metal surface interface, **(b)** organic molecules at the metal interface. When we brought the isolated molecule near to the metal surface, the initial discrete levels of the isolated molecule (here, HOMO and LUMO) are broadened and shift relative to the density of states of the metal substrate. 23

1.9 Schematic representation of molecular adsorption on a magnetic surface, **(a)** the discrete energy levels of an isolated molecule (left), and softly broaden energy levels of a molecule upon physisorption (right), **(b)** chemisorption of a planar molecule on the surface. Up and down arrows represent the spin-up and spin-down density of states. 25

2.1 Algorithmic flowchart representing the iterative procedure to solve the Kohn-Sham equations. 45

2.2 Schematic representation of pseudopotential formalism. The dashed line shows the pseudopotential $v_{ion}^{PS}(\vec{r})$ and corresponding pseudo wavefunction $\psi^{PS}(\vec{r})$, while the solid line represents all-electronic wavefunction $\psi^{AE}(\vec{r})$ and ionic potential, $v_{ion}^{AE}(\vec{r})$. The cut-off radius (r_c) represented by the vertical dashed line, at this point the pseudo quantities ($\psi^{PS}(\vec{r})$ and $v_{ion}^{PS}(\vec{r})$) matches with the all-electron quantities ($\psi^{AE}(\vec{r})$ and $v_{ion}^{AE}(\vec{r})$). 54

3.1 Optimized structure of bulk unit cell of SCOF. 63

3.2 Optimized structures three types of BTO-SCOF-BTO multilayer configurations stacked along [001] direction. **(a)** Nonpolar system (NP), where the BTO composition is pseudo-cubic with no polarization, **(b)** polar system (P1), the polarization direction of BTO is toward SCOF, and **(c)** polar system (P2) where the polarization is away from SCOF. Arrows in **(b)** and **(c)** indicate the polarization orientation. 63

3.3 Atom projected DOS of Co (black), O (red), and F (green lines) in **(a)** bulk SCOF, **(b)** NP, **(c)** P1, and **(d)** P2 configurations. The solid vertical magenta bars indicate the Co–ligand hybridization which causes the crystal-field splitting in the P1 configuration. Spin-up and spin-down partial DOS are shown by positive and negative values, respectively. The Fermi energy level (E_F) is set at $E = 0$. 67

3.4 Calculated bond angle and bond lengths of the Co2 octahedron in the P1 and P2 configurations. The atoms are labelled by the corresponding colors. 68

3.5 The $3d$-orbital projected DOS of the Co2 atom in **(a)** bulk SCOF, **(b)** NP, **(c)** P1, and **(d)** P2 configurations. The $3d$ orbitals are depicted by the different colors and spin-up and spin-down DOS are shown as positive and negative values, respectively. 69

3.6 Schematic diagram of electron occupancy in the high-spin and low-spin state configuration of Co2. 70

4.1 The optimized crystal structure of $[Fe\{OS(CH_3)_2\}_2\{Ag(CN)_2\}_2]$ complex. The Fe, N, O, Ag, S, C and H atoms are represented with the orange, blue, red, silver, green, black, and cyan color balls, respectively. 75

4.2 Computed variation of the aspect ratio with applied pressure. Red triangle and blue sphere symbols represent the calculated values of the b/a and c/a ratios respectively. 76

4.3 The computed total energy of the $[Fe\{OS(CH_3)_2\}_2\{Ag(CN)_2\}_2]$ complex versus variation of volume of the unit-cell volume, showing the energy minima at both the HS and IS states. 77

4.4 Structural phase transition from Monoclinic-I to Monoclinic-II in the unit cell of $[Fe\{OS(CH_3)_2\}_2\{Ag(CN)_2\}_2]$ complex. **(a)** static enthalpy difference as a function of pressure for two magnetic configurations HS (red) and IS (blue) of Fe atoms. **(b)** The calculated pressure versus volume of the unit cell at HS (red) and IS (blue) state. The data points are represented with symbols, whereas lines represent the fitted curves obtained from fitting with the Birch–Murnaghan isothermal equation of state. 78

4.5 Atom-projected partial DOS of the $[Fe\{OS(CH_3)_2\}_2\{Ag(CN)_2\}_2]$ complex, for **(a)** the Monoclinic-I structure with HS state magnetic configuration, and **(b)** the Monoclinic-II structure with IS state magnetic configuration. The positive and negative values of the DOS corresponding to the spin-up spin-down channel, respectively. The Fermi energy (E_F) is set at zero of the energy. 79

4.6 The 3d-orbital projected DOS of Fe atom in the $[Fe\{OS(CH_3)_2\}_2\{Ag(CN)_2\}_2]$ complex, for **(a)** the system is in the Monoclinic-I phase, and Fe atom is in HS state, and **(b)** system is in Monoclinic-II phase, and the Fe atom is in the IS state configuration. The positive and negative values of DOS corresponding to the spin-majority spin-minority channel, respectively. The Fermi energy (E_F) is set at zero of the energy. 81

5.1 The optimized structure of the NiQ molecule. Ni, O, N, C, and H atoms are represented through the orange, red, blue, black, and magenta colored balls, respectively. 87

5.2 Top and side view of the chemisorbed NiQ molecule on the surface of Co(001), in the HOLLOW configuration. The NiQ atoms are represented in the same way as in Figure 5.1, and green and grey coloured spheres represent the Co atoms. To make the Co positions in the second layer (hollow site) clearer, these Co atoms are represented with gray color and their bonds with other layer Co atoms are not shown. 88

5.3 Top and side view of the chemisorbed NiQ molecule on the surface of Co(001), in the TOP configuration. The color code of the atoms is done in the same way as in Figure 5.2. 88

5.4 Calculated relative total energy (ΔE) versus the molecule–surface distance. The total-energy curve displays its energy minima at 1.8 Å, which corresponds to chemisorption of the NiQ molecule on the Co(001) substrate in HOLLOW configuration. 90

5.5 *d*-orbital projected DOS of Ni atom in (**a**) gas phase NiQ; (**b**) chemisorbed in HOLLOW configuration; and (**c**) chemisorbed in TOP configuration. d_{xy}, $d_{yz}, d_{zx}, d_{z^2-r^2}$ and $d_{x^2-y^2}$ are shown as black, green, red, blue and orange line respectively. Positive and negative values, respectively show Spin-up and spin-down DOS. 91

5.6 Atom-projected partial DOS of chemisorbed NiQ molecule on Co(001): (**a**) NiQ adsorbed in HOLLOW configuration; and (**b**) NiQ adsorbed in TOP configuration. Positive and negative values, respectively show Spin-up and spin-down DOS. 93

5.7 Computed charge density (depicted by the light green hypersurface) of NiQ: (**left**) in HOLLOW configuration; and (**right**) in TOP configuration. The charge densities reveal that hybridization between the surface and molecule occurs only through the quinonoid ligands. 93

5.8 Partial magnetization density computed for an energy window indicated with two arrow marks in the spin-down channel of the PDOS plot for the HOLLOW configuration (Figure 5.6a). The magnetization density clearly shows the ferromagnetic coupling between molecule and surface, and also that an indirect superexchange mechanism is more dominant than the direct exchange interaction. The bright yellow and light blue hypersurfaces depict the positive and negative magnetization densities, respectively. 94

5.9 Computed total magnetization density of NiQ molecule chemisorbed in the TOP configuration. The magnetization density on ligand N and C atoms points to a ferromagnetic coupling between the molecule and substrate through a direct exchange path. The bright yellow and light blue hypersurfaces depict the positive and negative magnetization densities, respectively. 95

6.1 Optimized molecular structure of the Ni^{II}-dinuclear molecule in without-Cl **(left)** and with-Cl **(right)** configurations in the gas phase. Ni, O, N, Cl, C, and H atoms are represented by orange, red, blue, green, black, and magenta colored balls, respectively. 100

6.2 Top and side view of the chemisorbed Ni-dinuclear molecule on the surface of Co(001). The Ni, O, N, C, and H atoms in the molecule are represented in the same way as in Figure 1. To make the hollow site Co atom positions clearer, the top and hollow site of the Co atoms are represented by cyan, and grey coloured spheres, respectively, and the bonds of hollow site Co atoms with the other top site Co atoms are not shown. 100

6.3 Top and side view of the chemisorbed Ni^{II}-dinuclear molecule (with-Cl configuration) on the surface of Co(001). The molecule and substrate atoms are represented in the same way as in Figure 1. and Figure 2. . . 101

6.4 d-orbital projected DOS of Ni atom in the gas phase molecule, (a) without-Cl configuration, and (b) with-Cl configuration. (c) and (d) are the d-orbital projected DOS of Ni atom in the chemisorbed molecules on Co(001) in without-Cl and with-Cl configurations, respectively. The Fermi level (E_F) is set at E=0. 103

6.5 Computed magnetization density of chemisorbed molecule in without-Cl configuration (Top) and with-Cl configuration (Bottom). The bright yellow and light blue hypersurfaces represents the positive and negative magnetization densities, respectively. 105

A.1 (**Left**) DFT+U calculated relative total energy (ΔE) of NiQ on Co as a function of the Ni atom-substrate distance. The curve clearly shows a shallow energy minima at 3.5 Å, which corresponds to physisorption of the NiQ molecule on Co(001) substrate in TOP configuration. (**Right**) top view of the physisorbed NiQ molecule on the surface of Co(001), in TOP configuration. Ni, O, N, C, H and Co atoms are represented with orange, red, blue, black, magenta and green colored balls. Gray colored balls represent second layer (hollow site) Co atoms. 114

A.2 Calculated charge density (**left**) and magnetization density (**right**) of physisorbed NiQ molecule on Co(001) in the TOP configuration. The computed magnetization density shows that there is no magnetization density present on the molecule. 114

List of Tables

3.1 *Ab initio* calculated magnetic moments (in μ_B) on the Co atoms in bulk SCOF, and in the NP, P1, and P2 configurations of the heterostructures. 65

4.1 Fe-ligand bond-lengths (in Å) computed for the optimized HS and IS states of the [Fe{OS(CH_3)$_2$}$_2${Ag(CN)$_2$}$_2$] clathrate complex, as well as Ag chain bond lengths. The N1 and N4 atoms are also connected to N–C–Ag–C–N chains, while the O1 and O2 atoms are connected to the dimethyl sulphoxide (see Figure 4.1). 80

5.1 Ni–O and Ni–N bond lengths (in Å) of NiQ in the gas phase, and chemisorbed in HOLLOW and TOP configurations. 89

5.2 The magnetic moment on Ni and total molecular moment (in μ_B) of NiQ in the gas phase, and chemisorbed in HOLLOW and TOP configurations. 89

6.1 The Ni-ligand lengths (in Å) and magnetic moment on Ni (in μ_B) (in parentheses, Ni_2 atom values) of the molecule in the gas phase and chemisorbed in without-Cl and with-Cl configurations. 102

6.2 MAE of the Ni atoms in the chemisorbed molecule in without-Cl and with-Cl configurations. 107

Acronyms and Abbreviations

AFM	Antiferromagnetic
BTO	$BaTiO_3$
CB	Conduction band
CFSE	Crystal field splitting energy
DFT	Density functional theory
DOS	Density of states
FM	Ferromagnetic
GGA	Generalized gradient approximation
GKA	Goodenough-Kanamori-Anderson
GMR	Giant magneto-resistance
HF	Hartree-Fock
HOMO	Highest occupied molecular orbital
HS	High spin
IS	Intermediate spin
LDA	Local denisty approximation
LF	Ligand field
LS	Low spin
LUMO	Lowest unoccupied molecular orbital
MAE	Magnetic anisotropy energy
MeOH	Methanol

MOF	Metail-organic framework
MR	Magneto-resistance
NCCP	Norm-conserving pseudopotentials
NiQ	Ni(II)-Quinonoid
NP	Non polar
PAW	Projector augmented wave
SCO	Spin crossover
SCOF	Sr_2CoO_3F
SMM	Single molecule magnet
TM	Transition metal
VB	Valence band

List of Symbols

Symbol	Explanation
Å	Angstrom
α_s	Magnetoelectric coupling constant
B_0	Bulk modulus
$B_0^{'}$	Pressure derivative of B_0
Δ_0	Crystal field splitting energy
ΔE	Relative total energy
ΔM	Change in the magnetization per unit surface area
$\mathscr{E}_c$	Coercive field of $BaTiO_3$
E^{ex}	Magnetic exchange interaction energy
eV	Electron volt
μ_0	Vacuum permeability
μ_B	Bohr magneton

Chapter 1

Introduction

Spin electronics which is widely abbreviated as spintronics exploits electron's intrinsic spin degrees of freedom and its associated magnetic moment, in addition to its fundamental electronic charge. Mott expressed the two-fluid theory and recognized the importance of the intrinsic degree of freedom, the electron spin a long time ago (Mott, 1936). It states that, in a magnet, the velocities of electrons with different spins are different, therefore the current in a magnet can be characterized by having different spins, which forms the basis of spintronics (Sanvito, 2011; Rocha et al., 2005). Spintronics was born in 1988 with the discovery of giant magneto-resistance (GMR) effect by A. Fert (Baibich et al., 1988) and P. Grünberg (Binasch et al., 1989). Both the scientists were rewarded with the Noble Prize in Physics in 2007. The invention of GMR revolutionized the computation and data storage industries. The read head of the magnetic hard drives is one of the most well-known applications of GMR. There are many efficient devices such as magnetic field sensors, racetrack memories, non-volatile magnetic random access memory, etc., which are available in the market are based on the spintronics effect. Also, there are possibilities for designing numerous advanced devices by exploiting this effect (Chappert et al., 2007; Žutić et al., 2004; Wolf et al., 2001). Thus, the spintronics discipline has gained enormous research interest in recent days both from the fundamental aspect as well as the technological applications point of view.

In general, spintronic systems exert the fact that the electron current is made of spin-up and spin-down carriers, which carry the encoded information and interact differently with magnetic material. There are several advantages of exploiting the spin degrees of freedom in the device. The information encoded in the electron's spins of material can be written using low energies, can be manipulated with or without using magnetic fields, and can also be preserved when the device is switched off. The continuous effort in understanding and improvement of spin injection, spin manipulation, and spin detection in the magnetic systems in the last two decades, led to the technological revolution. At present, the ability to detect the spin state of a moving electron leads the whole magnetic data storage industry.

Spintronics has been studied first in transition metals, and later the focus was shifted to inorganic semiconductors and organic materials. Several theoretical and experimental works suggest that spintronic devices making with organic materials can offer similar or better performance than metals and inorganic semiconductors. On the other hand, the electronic properties of traditional organic insulating materials have gained increasing interest in the 1970s with the discovery of conductive polymers by A.J. Heeger. Afterword, A. MacDiarmid and H. Shirakawa discovered the organic semiconductor using doped polymer (Chiang et al., 1977). The discovery of conductive polymers opened up possibilities of using organic materials to fabricate low-cost electronic components that have the potential to replace conventional silicon-based technology. This discovery was rewarded with Noble Prize in Chemistry in 2000. Organic devices based on active thin-film are already in the market. Organic Light-Emitting Diodes (OLEDs) for bright and colorful thin displays, Organic Photovoltaic (OPV) for low-cost solar energy generation, and Organic Field-Effect Transistors (OFETs) are few examples in which organic compounds are used. This technology is promising for an entirely new generation of ultra-low-cost, light-weight and flexible electronic devices in the near future. Organic electronics have already passed the nano-scale and tending towards the miniaturization of electronic devices to its ultimate molecular scale limit. Therefore, in this current situation the molecular electronics is a very active field of research, looking at the ultimate downscale the device using single or few molecules. In 1971, B. Mann and H. Kuhn studied the electronic properties of an insulating molecule by measuring the tunnel current through the molecule (Mann and Kuhn, 1971). In 1974, M. Ratner and A. Aviram proposed a method to make a rectifier based on a single organic molecule (Aviram and Ratner, 1974). Their work administers the idea that it is possible to incorporate an appropriate molecule for each electric component of the device if it is practicable to relate the chemical structure of a molecule to its electrical behavior. This could overcome the possible down-scaling limitations in silicon-based technology and lead us to the ultimate miniaturization for devices dimension. On the other hand, altering the electrical properties of molecules with proper chemical modifications will provide a wide variety and possibilities to design functional devices based on the single molecular properties.

The spintronics and the molecular electronics have already been revolutionized the electronics device applications. In this context, a new research area ‘molecular spintronics’ is emerging to link these two novel disciplines. Molecular spintronics, a research field that has aimed to explore how the unique features of the organic materials can be exploited to develop the magneto-electronic devices that can fulfill the requirement of spintronic devices (Bogani and Wernsdorfer, 2008). A relatively new approach towards molecular spintronics has been investigated theoretically using the spin state of the molecule in which the information of the spin state transformed into electrical current (Pemmaraju et al., 2009). Thus, to employ this aspect of spintronics, the systems need to exhibit feasible spin states, which can be controlled by external stimuli. An intriguing phenomenon that has been observed to manipulate the spin state in the materials, especially those containing transition metal ions is spin crossover (SCO) phenomenon. Further, the ability to functionalize the SCO phenomenon at the single-molecule level will have a strong advantage over the switchable materials. The miniaturization in the information processing devices can be achieved by exploiting the SCO associated with hysteresis and magnetic/optical bistability at the single-molecule level, which will provide a very high-density data storage. On the other hand, tuning the magnetic moment of a TM in the materials by using the electric-field (electric polarization) may provide the substantial application possibilities to address the current challenges in the conventional magnetic data storage, such as achieving high-speed switching, low power consumption, and high operational stability simultaneously (Eerenstein et al., 2006; Troiani and Affronte, 2011). In this regard, switching the spin state of magnetic material by using electric polarization can be a possible way to address these challenges. However, spin manipulation and efficient spins detection are critical issues in spintronics, be it traditional spintronics or molecular spintronics. Therefore, looking forward to the possibilities, this thesis aims is to study the spin manipulation in the different functional materials.

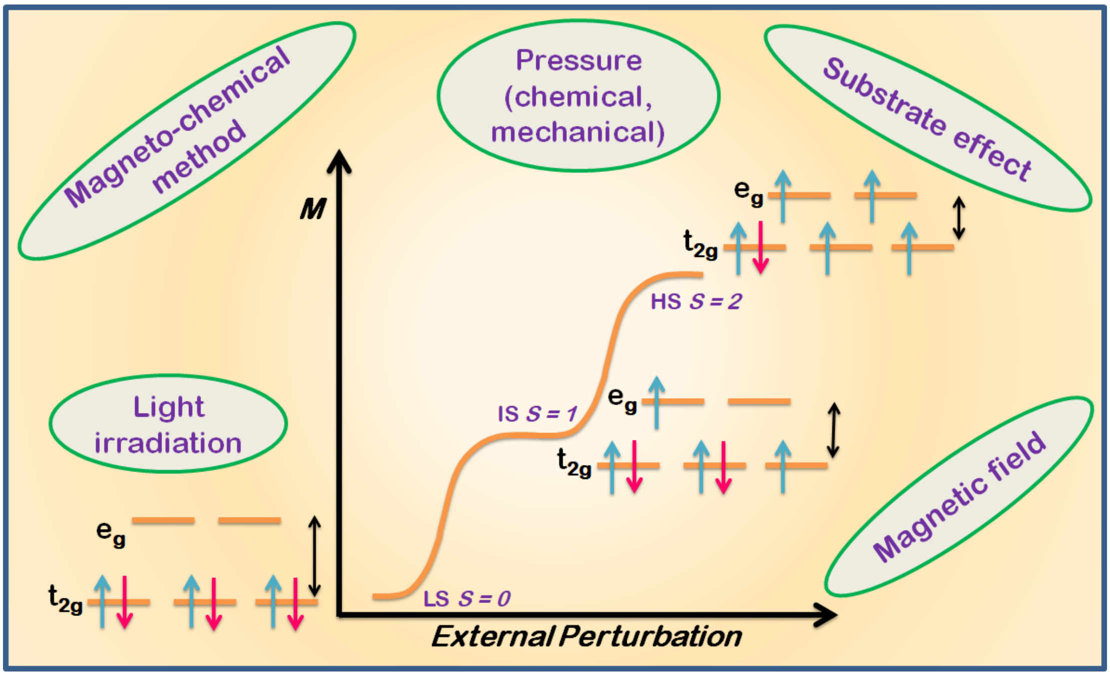
Magneto-chemical method
Pressure (chemical, mechanical)
Substrate effect
M
e_g
t_{2g}
HS $S = 2$
IS $S = 1$
Light irradiation
Magnetic field
LS $S = 0$
External Perturbation

Figure 1.1 Schematic representation of the SCO phenomena of a molecular system, where various external perturbations (pressure, temperature, light irradiation, magneto-chemical method, magnetic field) drive the change in the magnetic moment (M) or spin state.

The spin state of the magnetic materials can be controlled by external parameters such as pressure, temperature, electric/magnetic field, light irradiation, magneto-chemical methods, etc., as shown in Figure 1.1. In general, the SCO materials possess complex structural, electrical, and magnetic properties. There are several transition metals and ligand atoms present in the unit cell, which involve in the SCO phenomena with several different degrees of freedom. In this regard, understanding of the SCO phenomenon in such complex materials needs a highly accurate theory that can detect subtle changes in the crystal structure as well as the electronic structure during the spin state transition upon application of external perturbation. For example, in the case of SCO materials, the relative free energy difference between the two different spin states is very small. Employing an ab-initio based calculations would be a feasible route to understand observed novel SCO phenomena, and its cooperativity in extended systems like coordination polymers. This is a powerful tool to investigate the material properties as well as designing the new materials with desirable properties using the knowledge of existing materials. The major advantage of an ab-initio method is, one can proceed in a complete parameter freeway. The only inputs required in these methods is the information of constituents atoms and the approximate geometric structure of the systems. Hence it is also called the first-principles method, which is a very reliable, accurate approach (Saha-Dasgupta and Oppeneer, 2014).

In the present thesis, the complex SCO phenomenon has been investigated mainly in three class of materials by using the first-principles electronic structure calculations in terms of Density Functional Theory (DFT) calculations. A brief introduction to the SCO and the class of materials that have been studied in this thesis is described in the following section.

1.1 Spin Crossover

The SCO compounds are a well-known class of switchable materials. The SCO phenomenon was first observed in the 1930s by Cambi and co-workers in Fe(III) dithiocarbamate derivative (Cambi and Szegö, 1931). Later it was observed in Di-, Tri-, Tetra-, Penta- and Hexa-nuclear clusters, coordination polymers, and hybrid perovskites (Halcrow, 2013; Hogue et al., 2018). The SCO phenomena describe the spin state switching between different values due to an external perturbation such as pressure, temperature, light irradiation, electric field, or magnetic field. The materials that exhibit SCO have been suggested as promising materials for display, optical switching, sensors, information technology, and memory devices. Complexes that includes transition metal (TM) ion with $3d^4 - 3d^7$ configuration are potential materials to exhibit the SCO behavior, in which one can rearrange the valence electrons of TM ion either in the high spin (HS) state or in the low spin (LS) state. For example, the HS and LS states of TM ion having d^6 configuration (such as Fe(II) or Co(III) complexes), the valence electrons may have the following energy orientations shown Figure 1.2.

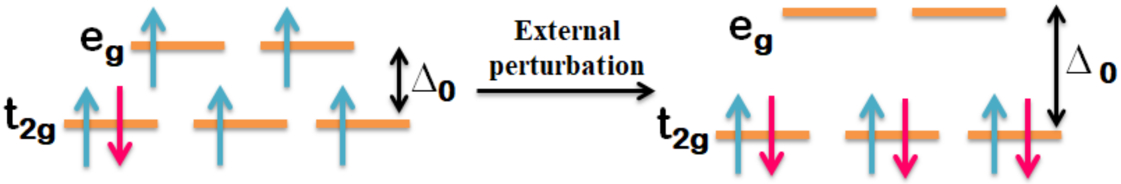

Figure 1.2 Schematic representation of the HS state (left) and LS state (right) of an octahedral complex of d^6 configuration materials.

The octahedral coordination compounds of $d-$orbital energies split into anti-bonding (e_g) and non-bonding (t_{2g}) orbitals due to the ligand field potential. The HS and LS state of the system depends on the energy difference between these t_{2g} and e_g orbitals. The energy difference between the t_{2g} and e_g orbitals also called the crystal field splitting energy or ligand field strength Δ_0. In the case of Fe^{2+}, all six electrons occupy the t_{2g} and e_g orbitals in accordance with Hund's rule, when spin repulsion is stronger than Δ_0 and shows an HS magnetic behavior. In contrast, all six electrons will nicely pile in t_{2g} orbitals, when spin repulsion is weaker than Δ_0 (singlet state or LS). In general, the SCO phenomena observed in octahedrally or tetrahedrally coordinated TM-complexes in which transition metal ions are in $d^4 - d^8$ electronic configurations. However, octahedrally coordinated Fe(II) SCO materials are a particular interest, since it may exist in diamagnetic (LS, S=0) and paramagnetic states (HS, S=2) (Gütlich et al., 2000). The SCO has also been observed less commonly in $3d^8$ and square-planar complexes (Kar et al., 2017). Many different class of SCO materials have recently been reported in which the SCO has been achieved using different external stimulation.

1.1.1 Crystal Field Theory vs Molecular Orbital Theory

Each transition metal (TM) has five degenerated d-orbitals. When the negatively charged ligands surround the metal ion, some of the d-orbitals interact with the ligands. The electrostatic interactions between the ligands and d-orbital electrons lift the degeneracy of the metal d-orbitals, which allows electrons to occupy either lower energy or higher energy levels depending on the orientation and nature of the ligands. For example, in an octahedral geometric structure of the molecule, ligands approach the TM ion along x, y, and z directions. As a result, the orbitals which lie along these directions (e_g orbitals) experience more repulsion than the other orbitals (t_{2g}). As a result, $d-$orbital energies split into sets of anti-bonding (e_g) and non-bonding (t_{2g}) orbitals. HS or LS state of a system are depending on the energy difference between t_{2g} and e_g orbitals, i.e. ligand field or crystal field splitting energy (Δ_0). The spectrochemical series vary from lower ligand fields (favoring, HS state) to higher ligand field (favoring, LS state), the ligands are $\mathrm{I}^- < \mathrm{Br}^- < \mathrm{S}^{2-} < \mathrm{SCN}^- < \mathrm{Cl}^- < \mathrm{NO}^{3-} < \mathrm{N}^{3-} < \mathrm{F}^- < \mathrm{OH}^- < \mathrm{C_2O_4^{2-}} <$ $\mathrm{H}_2O <$ NCS$^-$ < MeCN < pyridine < NH$_3$ < ethylenediamine < 2,2'-bipyridine < 1,10-phenanthroline (phen) < NO^{2-} < PPh$_3$ < CN$^-$ < CO and the metal ions $\mathrm{Mn}^{2+} <$ $\mathrm{Ni}^{2+} < \mathrm{Co}^{2+} < \mathrm{Fe}^{2+} < \mathrm{V}^{2+} < \mathrm{Fe}^{3+} < \mathrm{Co}^{3+} < \mathrm{Mn}^{4+} < \mathrm{Mo}^{3+} < \mathrm{Rh}^{3+} < \mathrm{Ru}^{3+} <$ $\mathrm{Pd}^{4+} < \mathrm{Ir}^{3+} < \mathrm{Pt}^{4+}$. However, the ligand field only induces the splitting in d-orbitals, but there are no clear energetic preferences for the HS or LS states.

Since crystal field theory is based on ligands symmetry around a metal ion and purely electrostatic model, it does not account for the covalent interactions and has limited applications. Therefore, Molecular Orbital (MO) theory is applied to account for both ionic and covalent bonding in TM complexes. The energy of the ligand orbitals determine the size of Δ_0, a strong σ-donor gives strong metal-ligand overlap, results in the higher energy anti-bonding e_g orbitals, whereas the t_{2g} orbitals remain localized and non-bonding, since the ligand atomic orbitals have different symmetry than that of t_{2g} orbitals, this leads to a larger Δ_0. The π-symmetry orbitals of π-donor ligands (with filled π-orbitals) have lower energy than the metal d orbitals, result in decreasing the size of Δ_0. On the contrary, π-acceptor ligands (with empty π-orbitals) have greater energy than the metal $d-$orbitals and are available for occupation, results in a greater value of the Δ_0. Using these as thumb rules it is possible to explain the order of the ligands in the spectrochemical series which have orbitals with π-bonding in addition to σ-bonding.

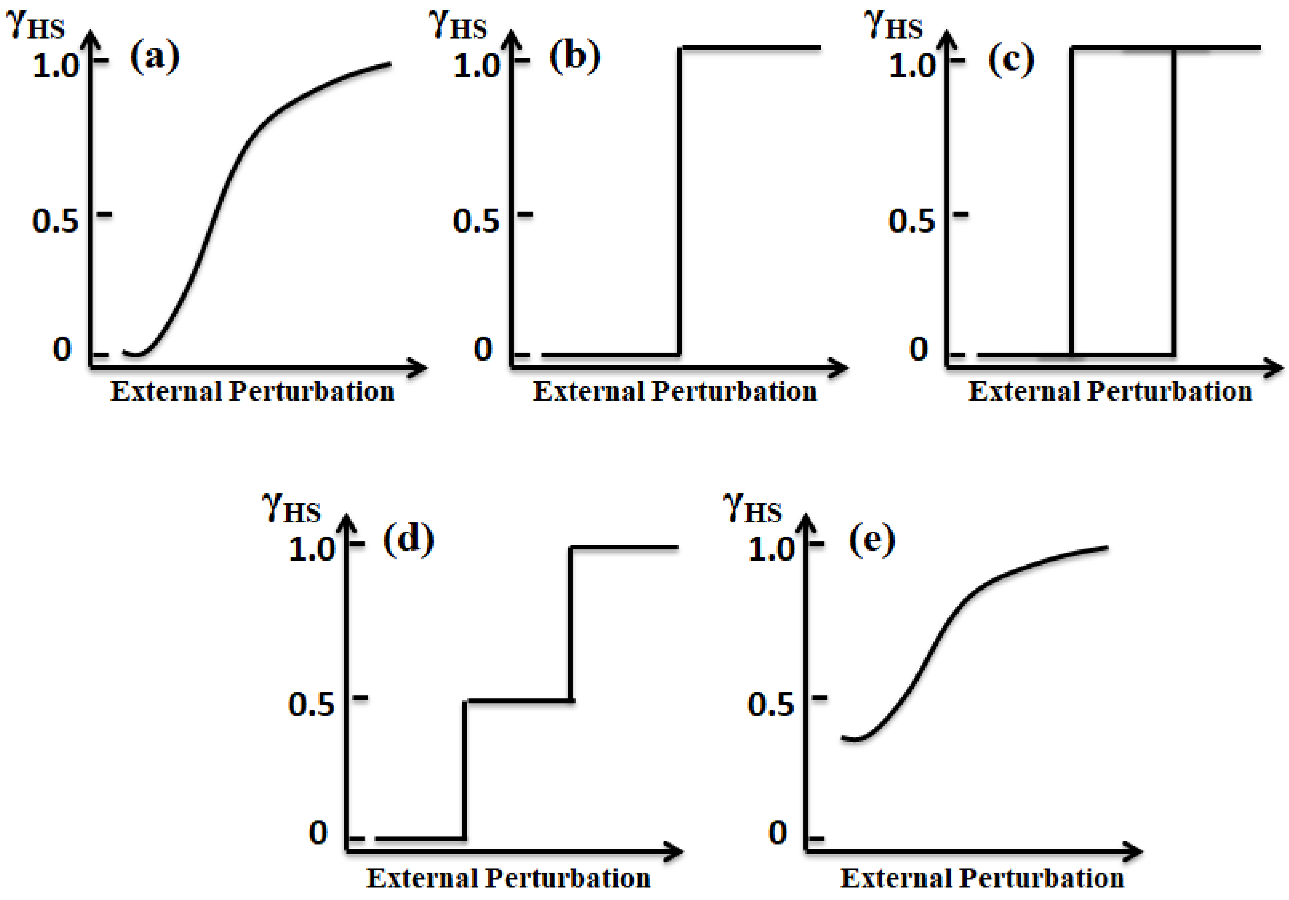

Figure 1.3 Different types of SCO behavior in terms of the molar fraction of HS molecules (γ_{HS}) as a function of external perturbation is represented schematically, **(a)** gradual, **(b)** abrupt, **(c)** hysteretic, **(d)** multi-step, and **(e)** incomplete.

1.1.2 Types of SCO Behavior

The SCO behavior in materials has been observed in different forms, such as abrupt, gradual, hysteresis, multi-step, and incomplete SCO (See Figure 1.3.). The materials which exhibit abrupt, gradual, and hysteresis SCO are bistable materials. In addition to the bistability, the hysteresis may exist between two stable states at the same external perturbation. The multi-step SCO materials have more than two stable states. Incomplete SCO appears when the material exists in a mix of HS and LS states at either maximum or minimum applied perturbation. SCO materials possessing bistable states that exhibits hysteresis behavior due to an external perturbation are potential materials in the memory storage devices. Easily triggered abrupt SCO materials with hysteresis loop centered at room temperature are the ideal candidates for storage devices. To date, the data stored in optical disks or magnetic storage are in binary format as a switchable series of zeros and ones. The storage efficiency can be enhanced significantly by using the multi-step SCO materials which exhibit hysteresis. Hua Li *et al.* demonstrated a non-volatile ternary data storage device, which can record data as zeros, ones, and twos (Li et al., 2010). Recently, four and eight-step SCO materials have also been reported (Zhang et al., 2020; Peng et al., 2020).

1.1.3 Potential Applications of Spin Crossover Materials

The molecular sensitivity to the applied perturbation, in combination with measurable effects on the bulk properties of SCO compounds, shows tremendous potential for molecular spintronics with a wide range of applications, including memory storage, electrical switches, display and sensor devices.

The bistable SCO materials with a hysteresis loop can be used in data storage devices. Since the spin relaxation time in organic molecules is in general very large, the desired spin state among the two stable states can be maintained for a relatively long time. This essentially means that such molecules have an intrinsic non-volatile nature. Materials exhibiting abrupt SCO behavior to the external pressure, temperature, light irradiation, or magnetic field, can act as molecular switches, where the conversion between two stable HS and LS states differentiates between the ‘on’ and ‘off’ states and may serve as NOT operators in logic operations. Since SCO occurs due to the atomic relaxation and internal charge rearrangement, the two different molecular states show completely different electronic structures. Consequently, one could expect two different I-V curves for the conductivity measurement in a two-terminal device. Thus the spin state is electrically readable. The abrupt SCO materials can also be used in colour displays. The pressure, temperature, or chemical induced SCO materials can be used for sensor applications. A sensor that can detect any two parameters among the pressure, temperature, and chemical changes would be highly advantageous and can be used to detect the change in one parameter while the other parameter being constant.

1.2 Types of SCO Materials

Several types of SCO families have been reported, among them an example, perovskites (inorganic, organic, and hybrid), coordination polymers, TM-triazoles, square-planar molecules, Hofmann clathrates are well-known. In the present thesis, three different classes of materials have been considered to study the complex SCO phenomenon by using Density Functional Theory (DFT) based on first-principles electronic structure calculations. The class of materials that have been focused in this work are given below,

1. Perovskite oxide materials
2. Metal-organic Hofmann clathrates
3. Metal-organic square-planar molecules

The motivation to study the SCO phenomena in these class of materials is that they have the potential to create promising research axes to address the current challenges in the conventional data storage industry (perovskite materials, i.e. multiferroic materials) (Eerenstein et al., 2006), as well as to develop various SCO based applications, particularly multi-step SCO with hysteresis (Hofmann clathrates) (Peng et al., 2020), and to realize the single-molecule spintronic applications (square-planar molecules) (Wende et al., 2007).

1.3 Perovskite Oxide Materials

Complex oxides are inorganic crystalline materials that contain both the metal and oxygen ions and represent a specific category of the well-known metal oxides. The metal oxides can be termed as complex oxides when a structural unit cell of the material contains a group of ions from two or more different metal groups or the same metal with two or more different oxidation states along with oxygen ions. These oxide materials have gained enormous interest in both fundamental and application-oriented research due to their several interesting physical and chemical properties, e.g. High-Tc superconductivity, Mott transition, spin state transition, multi-ferocity, colossal magnetoresistance, etc.. The perovskite family is one of the largest class of oxide materials and has played a major role in the field of solid-state chemistry and physics, e.g. superconductivity, ferroelectricity, and photocatalytic activity. The structural, electronic, and magnetic properties of perovskite materials have been reviewed extensively in the last few decades (Mitchell, 2002).

Gustav Rose discovered the first perovskite-based mineral $CaTiO_3$ in the Ural mountains of Russia in 1839. The perovskite name was given after famous Russian mineralogist Lev Perovski Alexevich Perovski (De Graef and McHenry, 2012). Victor Goldschmidt first described perovskite's crystal structure in 1926 in his work on tolerance factors (Goldschmidt, 1926; Liu et al., 2009). The class of compounds which have the same $CaTiO_3$ crystal structure are known as the perovskite structure, e.g. $FeSiO_3$ and $MgSiO_3$ (Wenk and Bulakh, 2016). The general formula for perovskite oxide structure is ABO_3 (A = alkaline or rare-earth cation; B = transition metal cation). The perovskite structure is shown in Figure 1.4. It consists of an array of corner-sharing BO_6 octahedral units with A cations occupy (sitting) an interstitial site in between the octahedral units. In general, the perovskite oxide structures are derived from the cubic structure, however, the structures could be non-cubic due to the common distortions in the structure. Moreover, many compounds exist with lower symmetry structures (tetragonal, orthorhombic or hexagonal symmetries) at low temperatures, for example, $BaTiO_3$ is tetragonal at room temperature and adopts orthorhombic and rhombohedral structure if it is cooled below room temperature, it has cubic structure only above 120°C.

The A and B sites in the perovskite structures can adopt a large number of metal cations. Thus, one can finely tune the metallic cation sites and control the chemical compositions, subsequently the electronic and magnetic properties, for example, magnetoresistive manganite and superconducting cuprate (Moritomo et al., 1996; Tokura and Nagaosa, 2000; Cava, 2000; Dagotto, 1994). In spite of having the possibility to tune the chemical composition of the perovskite structure, the tolerance factor (t), i.e. the ratio of the A-site and B-site cations of the stable structure may be in the range of 0.75-1.0, the 't' can be calculated as (Pena and Fierro, 2001)

$$t = \frac{R_A + R_O}{\sqrt{2}(R_B + R_O)} \tag{1.1}$$

where, R_A, R_B, and R_O are the ionic radii of A and B site cation elements and an oxygen

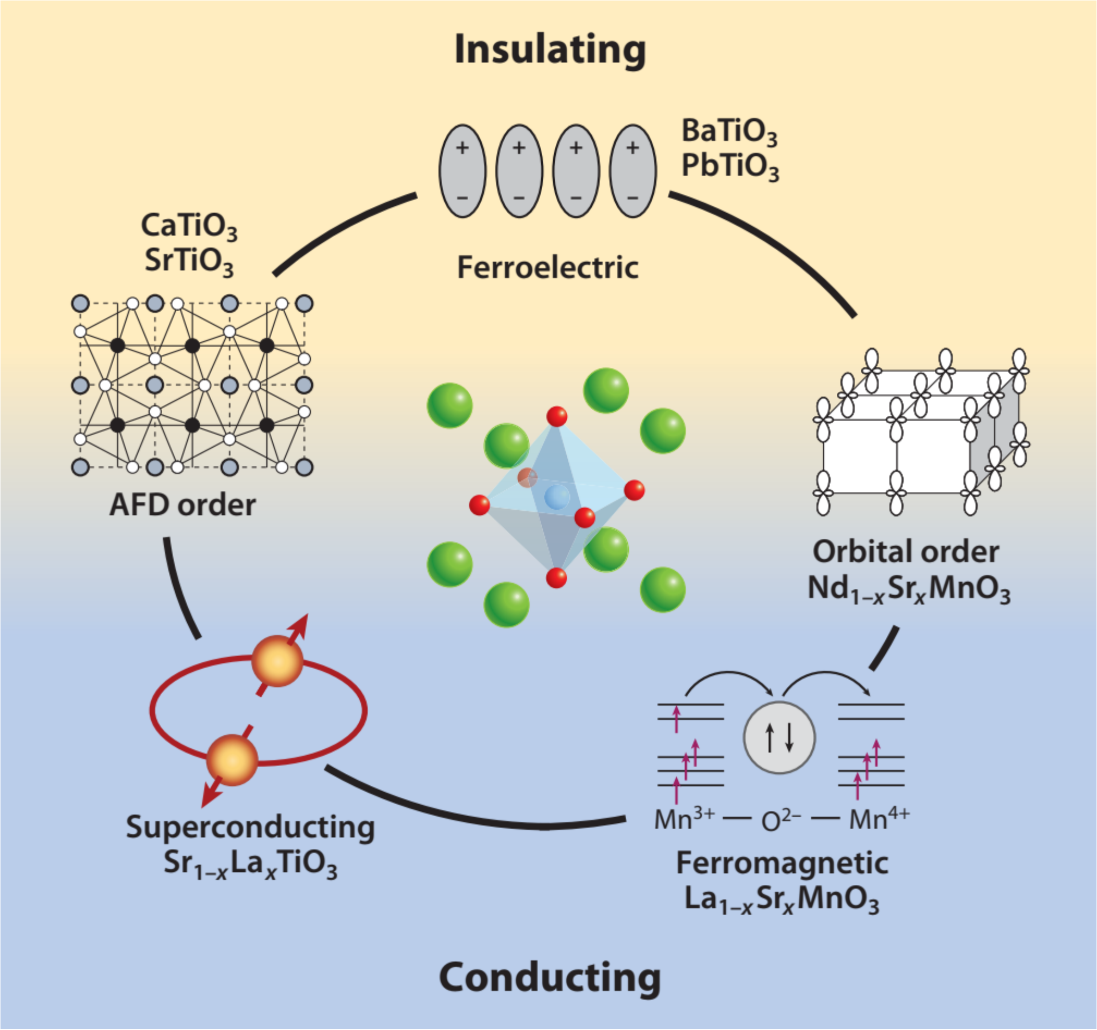
Insulating
BaTiO$_3$
PbTiO$_3$
Ferroelectric
CaTiO$_3$
SrTiO$_3$
AFD order
Orbital order
Nd$_{1-x}$Sr$_x$MnO$_3$
Superconducting
Sr$_{1-x}$La$_x$TiO$_3$
Mn^{3+} — O^{2-} — Mn^{4+}
Ferromagnetic
La$_{1-x}$Sr$_x$MnO$_3$
Conducting

Figure 1.4 A schematic picture illustrating the structure of the perovskite oxides in the centre, where the A, B and O atoms are represented by green, blue, and red spheres, respectively. Also, demonstrating the various properties of complex perovskite oxides. Figure adapted from Zubko, P. *et al.*, Annu. Rev. Condens. Matter Phys., 2(1):141-165 (2011).

atom, respectively. In the ideal cubic unit cell of a perovskite structure, the A cation, B cation and O atom sit at cube-corner positions (0,0,0) and body center position (0.5, 0.5, 0.5), and face-centered positions (0.5,0.5,0), respectively, as shown in Figure 1.4. The ideal ratio value of the tolerance factor for the stability of the cubic structure is 1. However, the relative ion size requirements for the ideal value of the tolerance factor (for the stability of the cubic structure) are quite difficult. Thus, slight buckling and distortion can result in tilted BO$_6$ octahedral in perovskites (several lower-symmetry distorted versions) or transformations to other non-perovskite structures.

The Perovskite structures may be extended to the layered perovskite inter-growth systems, where thin sheets of the other materials separate the ABO_3 structure. Based on the chemical composition of the intrusion or interpenetration, the layered perovskites can be classified into three different types, which are defined as

1. Ruddlesden-Popper (RP) phase: The general formula of this phase is $A_2A'_{n-1}B_nO_{3n+1}$, where n is the number of perovskite block. This phase happens to be the simplest one among other phases. In this phase, the intercalating layer occurs between every one (n = 1) or two (n = 2) perovskite block of the ABO_3. Usually, the RP phases are possible when two different types of A-site cations exist with different in size (or charge).

2. Dion-Jacobson (DJ) phase: In this particular phase, the inter-penetrating (or separating) layer is composed of an alkali metal (M) for every n ABO_3 layers. The general composite formula is $M^{10+}A_{n-1}B_nO_{3n+1}$.

3. Aurivillius (AV) phase: In this phase, the inter-penetrating layer is composed of rock salt $(Bi_2O_2)^{2+}$ layer, occurring every n ABO_3 layers. The general composite formula is $(Bi_2O_2)A_{n-1}B_nO_{3n+1}$.

Perovskite materials exhibit many interesting structural, electronic, and magnetic properties from both the theoretical and the application point of view. The intriguing interplay between the charge, spin and orbital degrees of freedom leading to a broad spectrum of functional properties; for instance, colossal magnetoresistance, ferroelectricity, superconductivity, charge, spin transport, metal-to-insulator transitions, and insulator-to-superconductor transitions (for strongly correlated compounds), see Figure 1.4 (Zubko et al., 2011). These compounds are used as sensors and catalyst electrodes in certain types of fuel cells and are candidates for memory devices and spintronics applications.

Many superconducting ceramic materials have perovskite-like structures, often with three or more metals including copper, and some oxygen positions left vacant. One prime example is Yttrium Barium Copper Oxide which can be insulating or superconducting depending on the oxygen content. There has been considerable progress in the field of solid-state chemistry and physics after the discovery of a high-T_C superconducting cuprate by Bednorz and Muller (Bednorz and Müller, 1986).

1.3.1 Perovskite Oxyhalides

Metal-oxygen polyhedra (octahedra, pentagonal bipyramid, trigonal bipyramid, tetrahedra, square pyramid, square-planar, etc.) is the basic structural unit in metal-oxide or metal-oxide based perovskite materials. The strongly correlated electrons within $d-$ and $f-$ orbitals, i.e. each electron in this orbitals has an individual influence on the neighboring electrons of oxygen atoms, that often exhibit the multiferroic, piezoelectric, high-T_C superconductivity properties. In perovskite materials, the TM atoms are surrounded by strong electronegative oxygen atoms that remove the s electrons from the TM atoms. As a result, the $d-$orbitals of TM experience an anisotropic field, known as the crystal field. Subsequently, the TM based perovskites exhibit spin state transition and/or SCO when the $d-$orbitals of the TM atoms are subjected to a sufficient crystal-field splitting, see Section 1.1.

Most of the examined members of the perovskite family, which has played a large role within the realm of solid-state chemistry and materials are oxide based perovskites. The majority of studies have been done in these systems were to control the structural and physical properties by influencing (or manipulating) the cation sites. The efforts to control the structural and physical properties of the perovskites by manipulating anion sites. i.e. substituting oxygen atom by other anions such as fluoride, nitride, hydride, chloride, etc. has recently started to gain great attraction (Kobayashi et al., 2018), as the incorporation of anions allow us to design new materials by introducing coordination geometry environment (metal-anion polyhedra) into the system. Further, the anions with different covalency, ionic radius, valence state than that of oxides, strongly affect the electronic states near the Fermi energy by changing the chemical interactions between p states of ligand (i.e. anion) and d states of the TM. The choice of anion and degree of anion order greatly alter the band dispersion, size of insulating band gaps, orbital hybridization, crystal field splitting, and d electron filling, which gives rise to a wide variety of unprecedented physical and chemical properties.

On the other hand, the incorporation of cation can be more easily realized compared to the incorporation of the anion. The size, electronegativity, valence and structural compatibility of the incorporating anion has to be considered carefully to achieve successful chemical substitution. Thus, researchers can routinely incorporate oxide ions with similar neighboring nitride, fluoride, and sulfide anions to alleviate the size and electronegativity challenges of anion incorporation in perovskite oxides. The discussion herein does not seek to rigorously explain the synthetic techniques, structural, electronic and magnetic properties of oxyhalide (or mixed-anion) based perovskites, instead only in a short description of motivation for choosing oxyhalide based perovskites over oxide-based perovskites. It is worth noting that more detailed discussions on the choice of selecting anion and their comparison to design and control the structural, physical and chemical properties have been extensively reviewed recently (Tsujimoto et al., 2012b; Harada et al., 2019).

The choice of anion and degree of anion order has a significant effect on Crystal Field Splitting Energy (CFSE) in mixed-anion perovskite compounds. The electrostatic fields generated by the different ligands modify the amount of energy difference between the d-orbitals of TM and the spectrochemical series approximates this energy from the weakest ligand to the strongest ligand. For example, Harada *et al.* demonstrated the evolution of CFSE on the choice of anion and concentration of anion within the specific octahedral configuration of a TM cation in an oxyfluoride compound AMO_xF_{6-x}, where the TM coordinated by different ligands (anions), see Figure 1.5.

The evolution of CFSE on the choice of anion within a specific octahedral configuration, and in a lattice under tetragonal distortion is shown in Figure 1.5a and 1.5b. Here only the electrostatic effect is included and excluded the hybridization. In the $\mathrm{MO_6}$ configuration, the substitution of fluoride ion at the apical sites can result in the trans-[$\mathrm{MO_4}F_2$] configuration. Since fluoride is a weaker ligand compared to the oxygen, the fluoride anions at apical sites reduce the electrostatic repulsion experienced by out-of-plane orbitals, subsequently lowering the energy level of $d_{z^2-r^2}$ orbital compared to that of the $d_{x^2-y^2}$ orbitals, see Figure 1.5a. On the other hand, the substitution of stronger ligand (N^{3-}) at apical sites instead of fluoride, i.e. trans-[$\mathrm{MO_4}N_2$] results in increasing the electrostatic repulsion along the z-direction thus rising the $d_{z^2-r^2}$ orbital

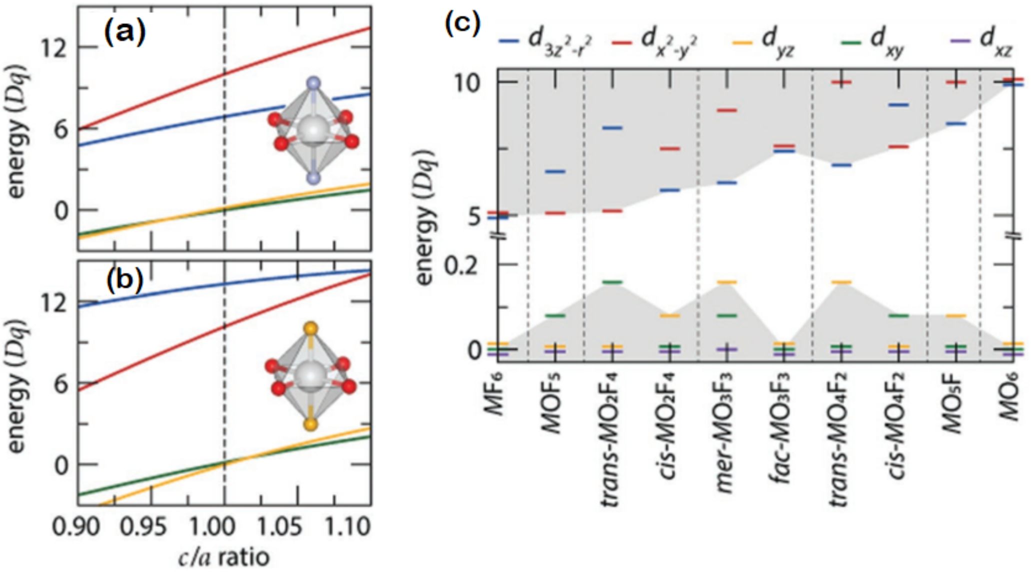

Figure 1.5 The evolution of crystal field splitting energy (CFSE) of a transition metal cation on the choice of anion and anion concentration in octahedral coordination. **(a)** and **(b)** The CFSE under a tetragonal distortion within a specific octahedral configuration for trans-[MO_4F_2] and trans-$_4N_2$, respectively, and the corresponding octahedral configurations are illustrated in the respective graphs. **(c)** The CFSE for a transition metal cation in the octahedral coordination, MO_xF_{6-x} (x=1-6) with varying anion concentration (or configuration) and without bond distortions. Figure adapted from Harada, J. K. *et al.*, Advanced Materials, 31(19):1805295 (2019).

compared to the $d_{x^2-y^2}$ orbital, see Figure 1.5b.

The evolution of CFSE for a TM cation octahedrally coordinated by oxide and fluoride ions with varying anion configurations in a cubic lattice is shown in Figure 1.5c. In general, the CFSE varies linearly with the concentration of anion in a hypothetical AMO_xF_{6-x} compound, where the anion sub-lattice possesses a statistical distribution of oxide and fluoride ions. However, in the case of mixed-anion polyhedra order the CFSE relationship with anion concentration is considerably different rather varying linearly. Since the ligands are pointed directly towards e_g ($d_{x^2-y^2}$ and $d_{z^2-r^2}$) orbitals, the e_g orbitals exhibit stronger electrostatic repulsion compared to the t_{2g} (d_{xy}, d_{yz} and d_{zx}) orbitals. According to the spectrochemical series, the CFSE energy between the e_g and t_{2g} orbitals is larger (10 Dq) for the oxide [MO_6] unit compared to the fluoride [MF_6] unit (5 Dq). Further, the set of e_g and t_{2g} orbitals are degenerate for the homoleptic oxide and fluoride compounds in an ideal octahedral geometry. However, the electrostatic anisotropy ascribed from the ordering of oxide and fluoride ions lifts the degeneracy of the orbitals in the e_g and t_{2g}. Harada *et al.* assert that the hierarchy of orbitals is dependent on the anion configuration, for example, the energy splitting between t_{2g} and e_g is straddled by d_{yz} and $d_{z^2-r^2}$ for cis-[MO_2F_4], d_{xy} and $d_{x^2-y^2}$ orbitals for trans-[MO_2F_4] configurations (see Figure 1.5c). In addition to this, the authors also assert that the evolution of the CFSE is significantly different for oxyfluoride compared to the oxynitride under tetragonal distortion. These features suggest that reliable control of anion order in mixed-anion perovskite materials provides a way to engineer the band-structure. Moreover, the strong influence of crystal field effect with the possibility of wide range anions provides a new way to control the spin state transition and/or SCO phenomena in mixed-anion systems, whereas obtaining the SCO phenomena in conventional perovskite oxide materials is a rare possibility (Bang et al., 2014).

The incorporation of the anion is an appropriate way to add the functionalities to the perovskite systems. In general, using conventional solid-state reactions, stabilizing the system with mixed-anions is very difficult compared to the systems with single anion (oxide, nitride, sulfide, etc.). Thus, to develop the stabilized mixed-anion materials, most of the mixed-anion materials have been synthesized using topotactic, hydrothermal, or high-pressure synthetic techniques (Leblanc et al., 2015). The covalent interactions between the metal center and its mixed-anion ligands are at the heart of the trade-off between charge, spin, and orbital degrees of freedom, leading to interesting emergent physical properties, such as helical spin order in $MnTaO_2N$ (Tassel et al., 2015), superconductor $Sr_2CuO_2F_2$ (Hiroi et al., 1994; Ai-Mamouri et al., 1994), hydride-ion conductors $LaSrCoO_3H$ (Hayward et al., 2002), high Neel temperature $SrCrO_2H$ (Tassel et al., 2014), high mobility van der Waals Semiconductor $Bi_4O_4SeCl_2$ (Gibson et al., 2019), to name a few. Despite developing a number of mixed-anion perovskite materials in various applications such as optical, photocatalytic, ionic conductivity, dielectric, polar, magnetic transport and chemical transform applications, the SCO phenomena have been studied in only one mixed anion compound, i.e. Sr_2CoO_3F, theoretically and experimentally. The SCO phenomena in mixed-anion perovskite compounds by using different external perturbations are yet to explore. In future studies, manipulation of atoms (cations and/or anion sites) in a compound and/or applying other external perturbations such as temperature, electric, and magnetic field etc. may induce electromagnetic properties such as superconductivity, ferromagnetism and magnetoelectric coupling into the system. Thus, it will be interesting to assess the potentiality of mixed-anion perovskite compounds in the development of functional materials for spintronic applications.

1.4 Metal-Organic Frameworks

A new set of conventional material has gained considerable attention, these include ferroelectric insulators that show spontaneous electrical polarization and magnetic semiconductors that offer spin-selectivity to a tunnel current (Sanvito, 2011). While molecular magnetic materials, in particular, single molecular magnets (SMMs) have gained considerable attention among the new organic materials due to their extremely long spin relaxation time (at least at low temperatures reaching years). A new field is emerging using these magnetic molecules to combine the ideas and advantages of spintronics, and molecular electronics are named molecular spintronics (Bogani and Wernsdorfer, 2008). Researchers have got ample freedom to design functional molecules for spintronics due to the diversity and flexibility of molecular synthesis. These include molecular magnets, spin-filter molecules, spin-crossover molecules, molecular batteries, molecular conductors, molecular switches, and spacer layers for organic spin valves and magnetic tunnel junctions (Raman et al., 2013).

Metal-Organic Frameworks (MOFs) are a class of chemical compounds in which metal centers are connected through an organic linker and form porous coordination polymers. MOFs have gained particular research interest due to their enormous porosity and very large internal surface area. They have been extensively studied for the last two decades because of their possible application in gas storage and separation, particularly utilizing hydrogen as an energy carrier in storage (Zhou and Kitagawa, 2014). Moreover, the extraordinary degree of variability in organic ligands and inorganic components offers to form various types of MOF structures, i.e. dense systems, isolated molecular systems, or porous coordination polymers. These could be interesting functional materials for multifarious applications. Among the several types of MOFs, this work primarily focused on studying the SCO phenomena on cyanide-bridged complexes, i.e. Hofmann-type-like complexes and square-planar molecules. A general introduction of Hofmann-type complexes and square-planar molecules.

1.4.1 Hofmann-Type Like Complexes

The first Hofmann-type MOF was $[Ni(CN)_2(NH_3)]$.benzene, and it was synthesized by Hofmann and Kuspert in 1897 (Hofmann and Küspert, 1897). Later, Kitazawa *et al.* synthesized the first two-dimensional (extends in a plane) SCO compound of Hofmann clathrate family, i.e. $[Fe(pyridine)Ni(CN)_4]$ (Kitazawa et al., 1996). A few years later, Niel *et al.* changed the pyridine ligand in the same two-dimensional compound to pyrazine and synthesized the first three-dimensional (extends in all three-dimensions) SCO compound $[Fe(pyrazine)M^{'}(CN)_4]$, where M is Ni, Pd, Pt (Niel et al., 2001). In general, the cyanide-bridged bi-metallic coordination polymer complexes (or Hofmann-like networks) have a molecular structure similar to $[M(L)_2M^{'}(CN)_4]$, where M is the metal atom (for example, Mn^{2+}, Fe^{2+}, Co^{2+}, Ni^{2+}, Cu^{2+}, Zn^{2+}, and Cd^{2+}), $M^{'} = Pd^{2+}$, Pt^{2+}, Ni^{2+} and L = ligand (bpac ($4,4^{'}$-bis(pyridyl)acetylene), azpy (4,4-azopyridine), dpsme ($4,4^{'}$-di(pyridylthio)methane), etc.). The ligand could be either unindented or bridged, depending on that it forms two or three-dimensional compounds, respectively. A large space remains in between the layers of these complexes have the potential to accommodate the guest molecules inside the MOFs that could eventually modulate SCO response of the system. Apart from this, the compounds that host the guest molecules can be used in gas storage and drug delivery applications (Deshmukh et al., 2013; Mandal et al., 2017).

The SCO phenomena in Hofmann-type MOFs have been studied by using one-shot laser pulse, small guest molecules, oxidative addition of elemental halogens (Cl_2, Br_2, I_2) as external stimuli in addition to the pressure, temperature, electric, and magnetic field. The SCO transition temperature can be systematically controlled by modulating the halogen content (Ohtani et al., 2011). Taking advantage of the possibility in varying the organic ligand and TM atom, several 2D and 3D heterobimetallic Hofmann-

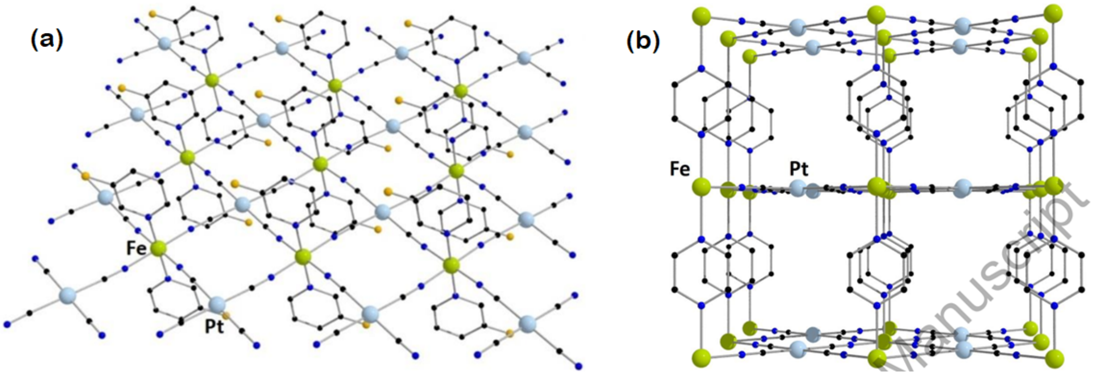

Manuscript

Figure 1.6 Representative view of 2D and 3D Hofmann clathrates. **(a)** A 2D Hofmann clathrate $[Fe(3\text{-}Fpy)_2Pt^{II}(CN)_4]$ (3-Fpy: 3-fluoropyridine) and **(b)** a 3D Hofmann clathrate $[Fe(pz)Pt^{II}(CN)_4]$ (pz: pyrazine). Fe, Pt, N and C atoms are represented with green, light blue, blue and black color spheres, respectively. The Hydrogen atoms are not shown in the figure for clarity. Figure adapted from Polyzou, C. D. & Tangoulis, V., Journal of Coordination Chemistry, 72(3):389-418 (2019) (Polyzou and Tangoulis, 2019).

type MOFs (Hofmann clathrates) have been synthesized. The Hofmann clathrate exhibit SCO behavior at room temperature. $[Fe(L)_2(NCS)_2]$(L=2,5-di-(2-pyridyl-1,3,4-thiadiazole)) and $[Fe(dpoda)\{Ag(CN)_2\}_2]$(dpoda=2,5-di-(pyridyl-1,3,4-oxadiazole)) Hofmann-type MOFs exhibit four-step SCO (Clements et al., 2016; Zhang et al., 2020). More recently, $[Fe(4\text{-}abpt)\{Au(CN)_2\}_2]$.2DMF.EtOH (4-abpt=4-amino-3,5-bis (4-pyridyl)-1,2,4-triazole) Hofmann-type MOF exhibit asymmetric seven/eight-step SCO (Peng et al., 2020). Thus, the Hofmann clathrates exhibit unique SCO behavior induced by external stimuli.

In this work, the context of the study of Hofmann-type MOFs is to explore the newly synthesized materials which are suitable for SCO.

1.5 Single Molecule Spintronics

One of the major challenges in molecular spintronics is to achieve magnetism at a single molecular level. It is essential to design magnetic molecules, which are stable at higher temperatures due to its technological relevance in data storage, sensor, quantum computing, and other single molecular spintronic applications (Rocha et al., 2005). The magnetic molecules react on a metallic surface, and some molecules may lose their magnetic properties by coupling with electrodes, even if they remain intact (Sanvito, 2011). In this regard, the molecular interactions with surface need to be understood well before its technological applications.

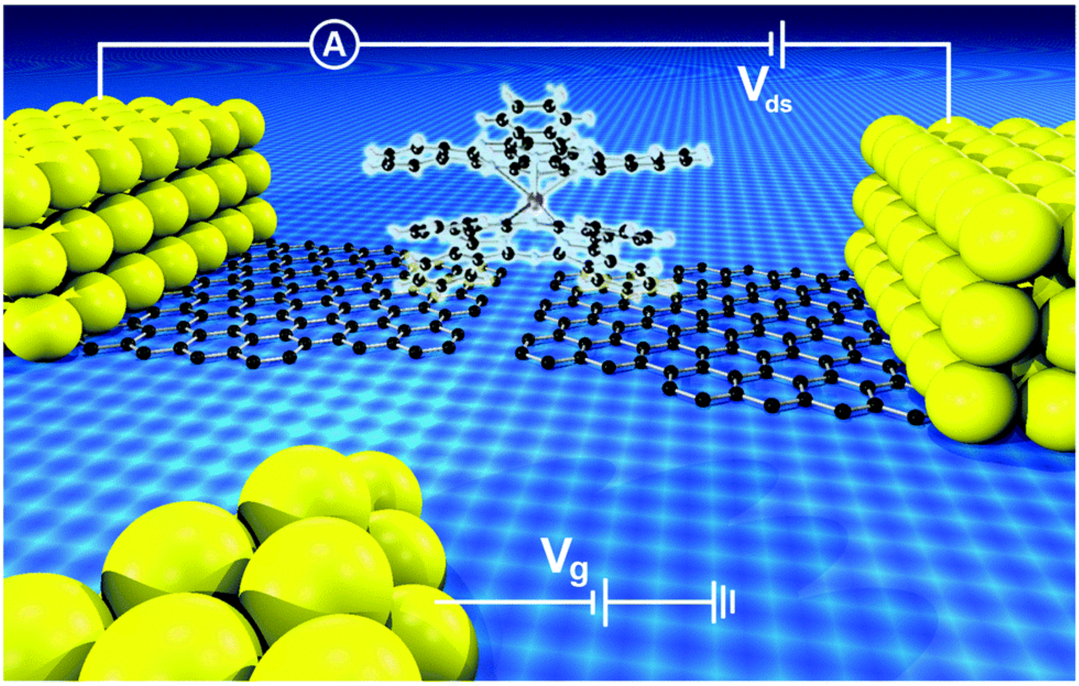

Figure 1.7 Schematic representation of the molecular device with graphene electrodes, where the $TbPc_2$ single-ion magnet located in the junction. A lateral gate electrode approaches the nano-gap. Figure adapted from Lumetti, S. *et al.*, Dalton Transactions, 45:16570-16574 (2016).

Further, placing the single molecules in electronic circuits is a major technical challenge to be solved to accomplish mass production of single-molecule devices (Lörtscher, 2013). Conventionally, gold has been used as the electrodes for the devices. However, the high atomic mobility of gold limits the device's mechanical stability and their operation at room-temperature. Graphene is an alternative material to fabricate stable molecular-scale electrodes (Sun et al., 2014). Production of graphene on a large scale fulfils the pre-requisite for the production of large scale complex architectures. The fabrication of 2D graphene electrodes reduces the size mismatch between molecules and electrodes, and the covalent bond-structure of graphene enhances the stability of the devices up to higher temperatures. Figure 1.7 shows the schematic illustration of a single-molecule device with graphene electrodes (Lumetti et al., 2016).

At an initial stage of molecular spintronics research, molecules have been used as a spin-transport medium and experiments were focused on spin-transport in molecular films to replace the inorganic semiconductor films that already existed in magnetic tunnel junctions and spin valves devices. Some organic materials have negative magneto-resistance (MR) sign, and some materials have both positive and negative MR (example, LSMO). These results contradicted the existed spin transport knowledge and well-established spin polarization sign of the ferromagnetic electrode. Initially, this contradiction was attributed to the different thickness of the organic layer, but later researchers showed that the sign of MR is independent on the thickness of the organic layer. The sign can be changed by changing the bias voltage (Vinzelberg et al., 2008). Finally, it was shown that the interface of ferromagnetic/molecule layer plays a key role in the origin of MR and the spin polarization of the ferromagnetic material can be tuned by molecular bonding (Sanvito, 2010). It has given a new direction to the spintronic research, namely ‘spin-interface’.The spin-to-charge conversion due to the Rashba–Edelstein effect, spin-orbit coupling and the spin–momentum locking at the surface of topological insulators have arisen mainly from interfacial properties, rather than the bulk of the constituent materials (Cinchetti et al., 2017).

On the other side, an intuitive theoretical model proposed by McConnell generated a strong research interest to investigate magnetism in organic molecules from the past five decades (McConnell, 1963; Verdaguer, 1996; Miller and Gatteschi, 2011). The extension work of this model led to the development of molecule-based materials that exhibit cooperative magnetic phenomenon, for instance, charge-transfer complexes with alternating donor-acceptor radical chains (Miller et al., 1988, 1993). As a result, today, ferromagnetism in molecular solids at room temperature is observed (Manriquez et al., 1991). However, achieving magnetism at a single molecular level is still a challenging activity. In MOFs, localized d- and f- state spin-dependent metal centers, which are stable up to room temperature are considered to be a potential class of materials for single molecular spintronic applications (Mannini et al., 2009; Rocha et al., 2005). In single molecular magnets (SMMs), the localized spin centers are stabilized by single-ion anisotropy of the molecular framework and demonstrate the magnetization hysteresis (Bogani and Wernsdorfer, 2008; Chudnovsky, 1996; Mannini et al., 2010).

1.5.1 Behavior of Organic Molecules at Interface

To understand the major advantages brought by organic semiconductors over conventional inorganic materials, it is essential to note the considerable difference that exists between organic and inorganic compounds (see Figure 1.8).

The electrons in inorganic materials are delocalized and form bands due to continuum energy levels. On the contrary, the energy levels in organic materials are discrete, and each level is corresponding to a molecular orbital. These molecular orbitals are highly localized. The two separated HOMO and LUMO orbitals in organic materials can be compared to the VB and CB in inorganic materials, respectively.

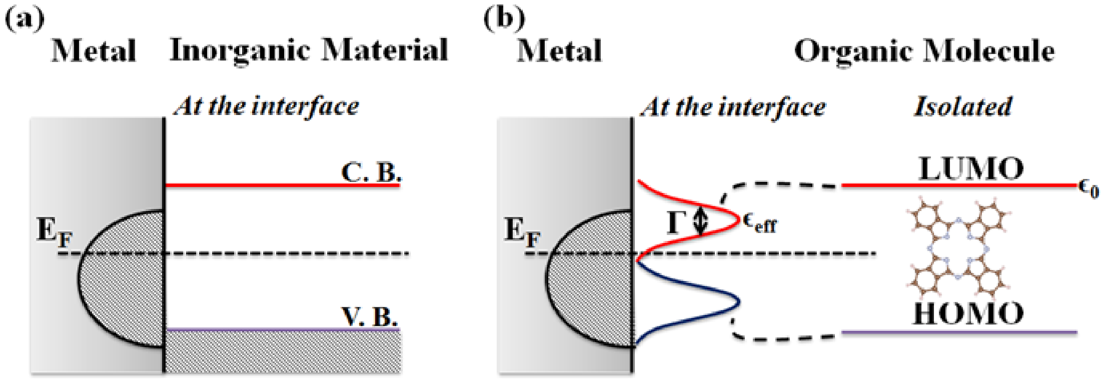

Figure 1.8 Illustration of the behavior of **(a)** an inorganic material at the metal surface interface, **(b)** organic molecules at the metal interface. When we brought the isolated molecule near to the metal surface, the initial discrete levels of the isolated molecule (here, HOMO and LUMO) are broadened and shift relative to the density of states of the metal substrate.

An isolated molecule has an infinity lifetime, and accurate energy ε_0 (according to Heisenberg uncertainty principle). When we brought this isolated molecule near to the metal substrate/electrode, the discrete levels of the isolated molecule gets hybridized at the interface by interacting with the metal orbitals and leads to two significant effects. Firstly, the lifetime of the discrete molecular levels will become finite. As a result, the energy δE is not accurate and gives the energy broadening at the molecular level with a finite width $\Gamma \approx \frac{1}{\tau}$ (for example, see LUMO of Figure 1.8b). This width is proportional to the metal Density of States (DOS). The broadening can be varied from meV to eV, depending on the strength of the interaction between the molecule and substrate (Vázquez et al., 2004).

Secondly, the molecule substrate interaction gives rise to a shift in molecular energy levels from ε_0 to ε_{eff}. The energy shift is dependent on the DOS of substrate/electrode, interfacial dipoles and image forces (Perrin et al., 2013). The types of adsorption of a molecule on the surface and the chemistry at the interface are described in the following section.

1.5.2 Spinterface

The isolated molecule which is at a relatively large distance from the surface/electrode (or in the gas phase) has discrete molecular energy levels. The bonding interaction may occur when one brought this molecule near to the surface/electrode. These bonding interactions vary from weak physisorption to strong chemisorption and considerably change the electronic structure of the molecules. In physisorption, the discrete molecular electronic levels are weakly broadened due to its proximity to the spatially extended metallic states. As a result, there will be no significant change in the electronic structure of the molecule and surface. Such a molecule-surface interaction may rearrange the electron density and Coulomb interaction between electron and hole associated with HOMO and LUMO. The renormalization of the electronic levels is also possible, and that could considerably modify the alignment of HOMO and LUMO frontier orbitals compared to the free molecular electronic levels. The existence of these weak interactions could be described theoretically as a linear combination of atomic orbitals of its constituents, and that can be confirmed experimentally through spectroscopic studies.

In chemisorption, electronic levels of adsorbate are broadened due to strong interaction with extended states of a metal surface, possible mixing of charge and strong hybridization. As a result, atomic orbitals are strongly overlapping spatially across the interface, and new hybridized interface states are formed, which are the combinations

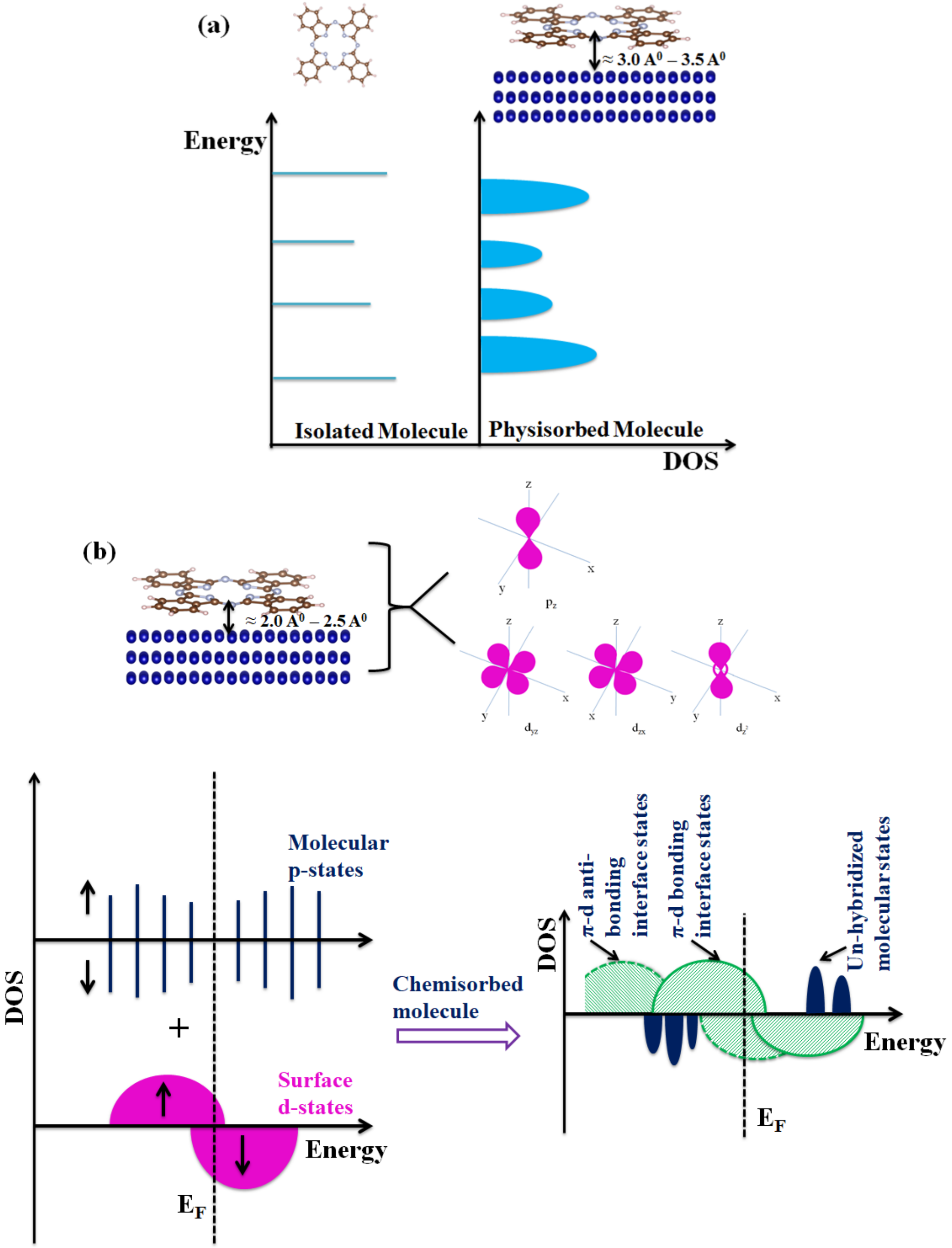
(a)
≈ 3.0 A⁰ – 3.5 A⁰
Energy
Isolated Molecule
Physisorbed Molecule
DOS
(b)
≈ 2.0 A⁰ – 2.5 A⁰
z
x
y
p_z
d_{yz}
d_{zx}
d_{z^2}
DOS
Molecular p-states
+
Surface d-states
Energy
E_F
Chemisorbed molecule
DOS
π-d anti-bonding interface states
π-d bonding interface states
Un-hybridized molecular states
Energy
E_F

Figure 1.9 Schematic representation of molecular adsorption on a magnetic surface, **(a)** the discrete energy levels of an isolated molecule (left), and softly broaden energy levels of a molecule upon physisorption (right), **(b)** chemisorption of a planar molecule on the surface. Up and down arrows represent the spin-up and spin-down density of states.

of participating atomic orbitals. Subsequently, the structural, electronic, magnetic, and chemical properties are changed at the interface. Orbital symmetry and overlap at the interface lead to a stronger interaction of the out-of-plane d- and p-orbitals (see Figure 1.9b, top right) forming spin-resolved hybridized π-d interface electronic states, while in-plane orbitals interact weakly. These interactions are depending on molecular structure, morphology, chemical sensitivity of the molecule, van der Waals interactions, and image potentials at the interface (Atodiresei et al., 2013).

The extent and the shape of the atomic wave-functions and atomic coordination at the surface are different from the bulk (Siegmann, 1992). The chemical environment at the interface also plays a key role in modifying the magnetism in both the surface and molecule. All the above effects at the surface can effectively change the magnetic exchange coupling, surface magnetic anisotropy and magnetic moment of the surface atoms. The molecule adsorption on a surface provides a different chemical environment at the interface that may further weaken the surface symmetry and affects the spin-resolved DOS. Notably, one can observe many exciting effects such as an enhancement or weakening of the surface magnetic anisotropy (K_{sur}), inter-planar magnetic exchange coupling between the surface and the bulk (J_S), in-plane surface magnetic exchange coupling $(J_{S//})$, or even cause a non-magnetic TM surface to become magnetic.

Furthermore, the magnetic interaction between the absorbed molecule and surface may alter the magnetic order, magnetic exchange coupling and magnetic anisotropy. The spin-orbit coupling in organic molecules is negligible. Therefore, the induced magnetic exchange interactions due to π-d hybridized states across the interface can be controlled. This could also lead to room temperature ferromagnetism in these systems. Hence, the magnetic interface properties that arise due to interface chemistry of molecule and surface demand a careful study with the help of advanced computational tools.

Growing molecules on magnetic as well as inert surfaces are the approaches to develop the pseudo-SMMs that show magnetic stability at higher temperatures with the help of substrate-induced magnetic exchange coupling as well as substrate-induced magnetic anisotropy (Scheybal et al., 2005; Cornia et al., 2011). In general, the non-planar molecules interact weakly with the surface than planar molecules; this is due to steric hindrance. However, in the case of chemically active elements (for example, sulfur, nitrogen, oxygen, etc.) attached either to the surface or to the molecule, the local chemistry might dominate the interface interaction irrespective of the structural form of the molecule. In this regard, more studies have been done using planar-molecules, such as metal-phthalocyanines and metal-porphyrins (Gottfried, 2015). These molecules are promising to manipulate or tailor the substrate-induced spin stability and spin-anisotropy of the TM centers. For example, Wende *et al.* observed the magnetic hysteresis response of Fe-porphyrin molecules coupled with the bottom magnetic Ni surface up to room temperature (Wende et al., 2007). The observed magnetic anisotropy in these molecules are relatively weak and shows paramagnetic behavior at high temperatures. The maximum anisotropy barrier of 30 K was observed for the case of Terbium(III) bis-phthalocyanine ($TbPc_2$) molecule (Malavolti et al., 2013). Several reports have shown the possibility to tailor and engineer the spin states of the TM centers using in-situ magnetochemistry (controlled adsorption/desorption of ligands to the molecule causing a change in the spin moment of the TM center) (Bernien et al., 2009; Barth, 2009; Wäckerlin et al., 2012; Herper et al., 2013). However, such mechanisms provide limited scope in selectively addressing single-molecule switching. Hence, the search for room temperature SMMs is an ongoing activity.

1.5.3 Advantages of Organic Molecules for Spintronics

There are several advantages of using organic molecules in spintronics:

1. Spin relaxation or spin lifetime is very long in organic materials due to weak spin-orbit interactions in the materials. Spin-orbit interaction scales as Z^4 (Z=atomic number), most organic molecules are made up of elements in the top rows of the periodic table. These low atomic number atoms give weak spin-orbit interaction in organic molecules. On the other hand, hyperfine interaction is not efficient in organic materials since only a few elements possessing nuclear spins. In general, the transport typically occurs through π-orbitals and the spin of mobile carrier is weakly sensible to the nuclear spins in the molecule. As a result, the spin of a

carrier interacts weakly with the organic environment and the spin information can be retained for a long time.

2. The organic semiconductors show potential for a flexible electronic application. The organic materials can be easily deposited on flexible substrates. Moreover, role to role ink printing technology with a low production cost and easy processing over a large area will provide flexible electronics device applications (Cinchetti et al., 2017). The possibility to combine spintronic devices with flexible substrates was first proposed in 1992 and has been already demonstrated with prototype devices (Parkin et al., 1992).

3. Advance molecular engineering brought the chemical versatility and opens the tailoring opportunities to design the new and desire organic compounds for spintronics applications, which could not be achievable with conventional inorganic materials. The unlimited choice of the molecules and its derivatives, with chemical versatility, may help us to find molecules with desire functionalities.

1.6 Scope and Objectives of the Proposed Work

The advantages of organic molecules and the diversity and flexibility of molecular synthesis has given ample freedom to researchers to explore and design molecules with new functionalities. Spin-interface research started to explain the puzzling results of spin transport in molecular devices, but now it is expanded from surface magnetism and emerged as a sub-field of molecular spintronics. The energy shift and broadening of molecular states while making the interface determine the nature of the device. The orbital interaction of the metal substrate and molecule forms hybridized states at the interface that leads to a significant change in the properties of the molecule, and it even changes the intrinsic properties of an inorganic material such as metals. One can also tailor the hybridized states by external stimuli such as light, temperature, chemical, electric and magnetic field. Hence, activating spin-interface by exploring new molecular designs and device schemes with tunable properties could be a promising way to develop future molecular spintronic devices.

On the other hand, SCO is an old phenomenon, but still fascinating us due to their peculiar switching properties, which conferring SCO complexes are potential candidates in several fields of technology, such as, data storage, sensors etc.. Moreover, the ability to functionalize the SCO complex properties at the single-molecule level will have a strong advantage over the switchable materials. Therefore, a single SCO complex represents a realistic molecular switch that can perform a certain function upon a certain stimulus in a reversible manner. Multi-step SCO molecules, which are the potential candidates to build multi-state memories, need to be explored in more molecules. In current research efforts, the significance of this single-molecule aspect seems to be underestimated, which may change in the near future. In this thesis, the broad objectives are the following.

Objectives

- Study and analyze the SCO phenomena in newly synthesized materials by applying external perturbation such as pressure, temperature, or electric field.

  As described in the previous section, the SCO phenomena is a fascinating one due to different spin states with an external perturbation and have great technological importance. The bistable, multi-step, and hysteresis type of SCO behavior compounds are particular interest to design memory storage devices. However, one should capture the minute energy difference that exists between the different spin states. DFT calculations provide a microscopic understanding of the SCO compounds. Hence, the DFT calculations have been employed to study and analyze the SCO phenomena in newly synthesized compounds, which may exhibit bistable or hysteresis SCO behavior by applying pressure, temperature or electrical field as an external perturbation.

- Study the magnetic properties of a group of magnetic molecules and their interactions with the metal surfaces.

  Metal-organic molecules have gained enormous interest in molecular spintronics. In general, non-planar molecules would bind weakly on a metal surface due to steric hindrance. Hence, planar metal-organic molecules (for example, phthalocyanines, porphyrins and quinonoid molecules) are particular interest to study the magnetic interactions between the adsorbed molecule and metal surface. Moreover, the adsorbed planar molecules will have one free ligand vacancy on the top side of the molecule that will allow us to tune the magnetic properties of the molecule through ligation. The proper understanding of the molecule-metal surface is essential to inject the spin into the molecule. A new planar metal-organic molecule has been proposed here to study the molecule-substrate interactions by employing DFT calculations.

1.7 Overview of Present Thesis

In this thesis, the SCO phenomena have been studied in four different compounds which belongs to three different class of materials. The first part of the thesis deals with exotic properties derived from the SCO phenomena in perovskite oxyhalide material and perovskite oxide structures, and the second part deals with the novel SCO properties in metal-organic complexes. In perovskite oxyhalide and oxide heterostructure, a detailed investigation has been done for $Sr_2CoO_3F/BaTiO_3$ heterostructures. The magnetic configuration and its change due to different electrostatic environment have been studied. Among metal-organic complexes, three different compounds have been considered, (a) metal-organic framework in Hofmann clathrate material, (b) the substrate-induced SCO phenomena in a square-planar molecule like Ni-quinonoid, followed by Ni-dinuclear square-planar molecule.

The first-principles calculations based on DFT have been carried out in conjunction with the analytical approaches on the materials mentioned above in order to understand the novel properties and exciting SCO phenomena from the microscopic point of view. The contents of the various chapters of this thesis have been organized as follows:

- **Chapter 2:** In this chapter, the methodology that has been used to perform the DFT calculations thesis shall be discussed. To start with, the fundamental concepts of DFT shall be discussed, followed by a prescription of how to apply the DFT method to obtain accurate electronic structure information of materials.

- **Chapter 3:** This chapter deals with the investigation of magnetic properties of a perovskite strontium cobalt oxyfluoride Sr_2CoO_3F (SCOF) in a hybrid perovskite heterostructure, where SCOF is sandwiched between two ferroelectric $BaTiO_3$ (BTO) layers. The focus will be to explain the electric polarization induced SCO phenomena in perovskite oxyhalide.

- **Chapter 4:** In this particular chapter, the investigation of SCO phenomena in MOF system by applying external pressure shall be discussed. The MOF system in this study is a Hofmann-type like 2D coordination polymer considered, namely $Fe\{OS(CH_3)_2\}_2\{Ag(CN)_2\}_2$. The pressure-driven spin state switching of the Fe atom in the complex is observed to be associated with structural transformation.

- **Chapter 5:** The substrate-induced SCO phenomena for a recently synthesized square-planar Ni(II)-quinonoid complex has been studied in this chapter. The structural, electronic, and magnetic properties of Ni(II)-quinonoid complex upon adsorption on a magnetic Co(001) substrate shall be discussed in detail.

- **Chapter 6:** In this chapter, the substrate-induced spin state switching in a Ni-dinuclear square-planar molecule has been studied. An unprecedented anti-ferromagnetic coupling of the Ni-dinuclear molecule to the ferromagnetic Co(001) substrate has been observed in this work. Detail description of the magnetic coupling mechanism for such magnetic interaction shall be discussed. Further, tuning the spin state and magnetic anisotropy energy of Ni atom in a chemisorbed molecule by adding an axial ligand (Cl atom) to the Ni atom in the molecule, i.e. magneto-chemical method shall be discussed.

- **Chapter 7:** This particular chapter deals with the summary and most important findings of the spin manipulation study on the different functional materials which has been studied in this work. Here, the possibilities of future directions for this work shall be discussed.

Chapter 2

Computational Methodology

In this chapter, the theoretical framework that has been used to carry out the work presented in this thesis shall be discussed. In the first step, the first-principles calculations have been overviewed briefly and explained how the physics of condensed matter could be described using the many-electron Schrödinger equation. In the next step, an alternative method, i.e. Density Functional Theory (DFT) to perform many-electron quantum mechanical calculations shall be described, followed by the Kohn-Sham method of dealing with DFT. The discussion herein does not seek rigorous proof of all the mathematical theorems behind DFT, instead only the salient concepts, equations, and common approximations. The implementation of the Kohn-Sham equations with a plane wave basis set as well as the issue of exchange and correlation in DFT shall be discussed subsequently. Next, the GGA+U method shall be discussed. The GGA+U method is a promising technique to capture the strong electron-electron correlation effect that exists in the partially filled 3d shell of TM atoms and the missing correlation effect beyond the plain GGA.

2.1 First-Principles Calculations

Condensed matter physics deals with the macroscopic and microscopic physical properties of matter. Study of physical and chemical properties of condensed matter from theoretical methods or computational point of view can be a very challenging activity because of the complexity of the system. There are two different approaches one can perform a theoretical investigation of condensed matter systems. In the first approach, empirical or semi-empirical models can be built with the help of a set of parameters to describe the observed experimental results. This often provides a good understanding of the system under study and can also predict the behavior of similar systems that are to be yet tested experimentally. The second approach is to perform first-principles calculations that start from basic atomic information of the constituents. The interactions between atomic nuclei and an electron-atomic nucleus which determine the chemical interactions and molecular bonding interactions between atoms, Coulomb interaction between electrons, and the properties of condensed matter systems (mainly electronic properties) are non-empirically calculated. As a result, the first-principles calculations may provide accurate electronic behavior of the complex systems. However, the first-principles calculations are challenging to solve due to the numerical formulation size of the problem. Hence, the development of accurate and efficient theoretical models or computational techniques is essential to understand the properties of the many particles systems.

2.2 Many-body Hamiltonian

In principle, the quantum mechanical wavefunction gives all the information about a given condensed matter system. One has to solve the many-body Schrödinger equation in order to get a wavefunction of systems composed of the interaction between negatively charged electrons and positively charged nuclei. The many-body Schrödinger equation for a complete system of N_i electrons and N_I nuclei is given as

$$[\hat{T}+\hat{V}]\psi_{MB} = -i\frac{d\Psi_{MB}}{dt} \tag{2.1}$$

where ψ_{MB} is the many-body wavefunction that contains the quantum probability amplitude for every possible configuration of electrons and nuclei, i.e. $\psi_{MB} = \psi_{MB}(\vec{r}_{i_1}, \vec{r}i_2, ...\vec{r}_{i_N}, \vec{R}_{I_1}, \vec{R}_{I_2}, ...\vec{R}_{I_N})$, where $\vec{r}_{i_N}$ and $\vec{R}_{i_N}$ are the coordinates including the spin degree of freedom as well as the position of the electron and nuclei, respectively.

The Hamiltonian for the corresponding many-body Schrödinger equation can be written as

$$
\begin{aligned}
\hat{H} \;=\; & -\sum_i \frac{\hbar^2}{2m_e}\nabla^2_{\vec{r}_i} - \sum_I \frac{\hbar^2}{2M_I}\nabla^2_{\vec{R}_I} + \frac{1}{2}\sum_{i\neq j}\frac{1}{(4\pi\varepsilon_0)}\frac{e^2}{\mid \vec{r}_i - \vec{r}_j \mid} \\
& -\sum_{i,I}\frac{1}{(4\pi\varepsilon_0)}\frac{Z_I e^2}{\mid \vec{r}_i - \vec{R}_I \mid} + \frac{1}{2}\sum_{I\neq J}\frac{1}{(4\pi\varepsilon_0)}\frac{Z_I Z_J e^2}{\mid \vec{R}_I - \vec{R}_J \mid} \qquad (2.2)
\end{aligned}
$$

where the lower and upper case italic subscripts represent electrons and nuclei, respectively, m_e is mass of the electron, M_I and Z_I are the mass and atomic number of I^{th} nucleus, respectively, e is the electron charge and $\hbar$ is the reduced plank's constant.

In order to treat the correlation between the N number of electrons requires the many-body equation to contain 3N variables, in solid-state systems (with N $\approx 10^{23}$ electrons). Thus, unfortunately, it is very difficult to solve the Schrödinger equation for the many-body system. The approximations have been devised to solve the exact many-body equation. In this regard, Born–Oppenheimer approximation is the most basic approximation to separate the motion of the electron and nuclei in a system. The physical basis for this approximation is on the fact that the mass of the nucleus is much larger than that of electron mass ($M_I >> m_e$) and the inverse masses of the nuclei are very small ($\approx 5.4\times10^{-4} m_e^{-1}$ in the case of hydrogen). As a result, the nuclei in a system move very slow as classical particles that move on a time scale much longer than that of the electrons. Hence, it is a good approximation to treat nuclei to be static in space and to exclude kinetic energy terms of the nuclei, i.e. considering only electrons motion in Eq. 2.2. Hence the positions of nuclei, $\vec{R}_I$ become external parameters rather than dynamical variables turns the many-body problem to many-electron problem where the electrons are moving in an external potential which was created by the positively charged nuclei fixed at $\vec{R}_I$. The Schrödinger equation for a many-electron system with many-electron wavefunction (ψ) is

$$
[\hat{T} + \hat{V}]\psi = -i\frac{d\psi}{dt} \qquad (2.3)
$$

Since this many-electron wavefunction (ψ) contains all the information about the electrons in a system, it is an essential object in electronic structure calculations. It gives the probability amplitude for finding the system of electrons in a given configuration, i.e. ψ = $\psi(\vec{r}_1, \vec{r}_2, ...\vec{r}_i)$, where $\vec{r}_i$ is the coordinates of the electrons including the position and as well as spin, i.e. $\vec{r}$ = (x,y,z,σ), where σ is spin coordinate and can take the values of

$\uparrow$ (spin-up) or $\downarrow$ (spin-down). Now the Hamiltonian for the electronic-structure is given by

$$\hat{H} = -\sum_i \frac{\hbar^2}{2m_e}\nabla^2_{\vec{r}_i} + \sum_i V_{ext}(\vec{r}_i) + \sum_{i\neq j} \frac{1}{(4\pi\varepsilon_0)} \frac{e^2}{\mid \vec{r}_i - \vec{r}_j \mid} + V_{I-I} \tag{2.4}$$

Here

$$V_{ext}(\vec{r}_i) = -\sum_{i,I} \frac{1}{(4\pi\varepsilon_0)} \frac{Z_I e^2}{\mid \vec{r}_i - \vec{R}_I \mid} \tag{2.5}$$

is the external potential due to the nuclei located at $\vec{R}_I$, and V_{I-I} is the classical electrostatic potential energy due to the mutual repulsion of the positively charged nuclei which is given by $\frac{1}{2}\sum_{I\neq J} \frac{1}{(4\pi\varepsilon_0)} \frac{Z_I Z_J e^2}{|\vec{r}_I - \vec{R}_J|}$. The solutions of many-electron Schrödinger equation must satisfy the following two constraints.

1. The total probability for every possible configuration of electrons is equal to 1, i.e. normalization.

2. The wavefunction is anti-symmetric with respect to the exchange of any two electrons coordinates (including spin), which must be the case for any system of identical fermions description, i.e. exchange symmetry.

In most of the cases, the actual interest is only the electronic system. The lowest energy solution of the time-independent many-electron Schrödinger equation is

$$(\hat{T} + \hat{V})\psi = E\psi \tag{2.6}$$

where $\hat{T}$ is the many-electron kinetic energy operator, i.e. $\hat{T} = -\sum_i \frac{\hbar^2}{2m_e}\nabla^2_{\vec{r}_i}$, $\hat{V}$ is the many-electron potential operator, i.e. $\sum_i V_{ext}(\vec{r}_i) + \sum_{i\neq j} \frac{e^2}{|\vec{r}_i - \vec{r}_j|}$, and E is the ground-state energy of the system of electrons. The calculations involving in the solution of the Eq. 2.4 and Eq. 2.6 are known as electronic structure calculations.

Even though the nuclei were treated as static in space from the point of view of the electrons to minimize the complexity of the many-body system, one can consider the configuration of nuclei that gives the lowest total energy for the complete system, as this is the configuration that a real system will naturally tend to adopt at low temperature. If one can solve the solution of this many-electron Schrodinger equation for a given external potential, the solution gives the ground-state energy, E. One can consider this energy to be a function of the nuclear coordinates E = E($\vec{R}_1, \vec{R}_2, \ldots, \vec{R}_I$). This energy only includes the internal energy of the electrons as well as the energy ascribed due to the interaction of the electrons with the nuclei, but it does not include V_{I-I}. Therefore, the total energy of the system is a function of the nuclear coordinates and governs the motion of the nuclei, i.e. $E_{tot} = E + V_{I-I}$. Note that the force on each nuclei can be obtained from the electron distribution, which is the solution of electronic Hamiltonian using Hellmann-Fynmann theorem. Hence a subsequent structural optimization can be performed for the system using a suitable algorithm.

Therefore, the Born-Oppenheimer approximation changes the system from many-body to many-electrons. Using the many-electron Schrödinger equation one can predict the motion of the atoms in any condensed matter system at a temperature in which the electrons can be considered to remain in their ground-state.

Obtaining an analytic as well as the numeric solution of the N-electron Hamiltonian is very difficult, as it consists of 3N mutually connected dynamical variables. Since most of the ground-state properties of a system can be express in terms of electron density, a density-based method is more appropriate to study the many-electron system. Therefore, the electron density, $\rho(\vec{r})$ is an essential quantity in the density functional theory (DFT) that shall be discussed in the next section. The $\rho(\vec{r}_i)$ which gives the probability density for finding an electron at position $\vec{r}_i$ is given by:

$$\rho(\vec{r}_i) = N\sum_{\sigma}\int d\vec{r}_1, d\vec{r}_2, ...d\vec{r}_{i-1}, d\vec{r}_{i+1}...\int d\vec{r}_N \psi^*(\vec{r}_1,\vec{r}_2,...,\vec{r}_N)\psi(\vec{r}_1,\vec{r}_2,...,\vec{r}_N) \tag{2.7}$$

And, the electron pair density which gives the probability density for simultaneously finding one electron at position i and another electron at position j is given by

$$\begin{aligned}\rho(r_i r_j) = N(N-1)\sum_{\sigma\sigma'}\int d\vec{r}_1, d\vec{r}_2, ...d\vec{r}_{i-1}, d\vec{r}_{i+1}...d\vec{r}_{j-1}, d\vec{r}_{j+1} \\ \int d\vec{r}_N \psi^*(\vec{r}_1,\vec{r}_2,...,\vec{r}_N)\psi(\vec{r}_1,\vec{r}_2,...,\vec{r}_N)\end{aligned} \tag{2.8}$$

The kinetic energy, T, is given by

$$T =< \psi \mid \hat{T} \mid \psi >= -\int d\vec{r}_1, d\vec{r}_2, .., \int d\vec{r}_N \psi^* \sum_i \frac{\hbar^2}{2m_e}\nabla^2_{\vec{r}_i}\psi \tag{2.9}$$

and the potential energy, V, is given by, $V =< \psi \mid \hat{V} \mid \psi >=< \psi \mid \hat{V_{int}} + \hat{V_{ext}} \mid \psi >$. The potential energy due to electron-electron repulsion, i.e. internal potential energy is given by

$$V =< \psi \mid \hat{V_{int}} \mid \psi >= \int d\vec{r}_1, d\vec{r}_2, .., \int d\vec{r}_N \psi^* \sum_{i \neq j} \frac{e^2}{\mid \vec{r}_i - \vec{r}_j \mid}\psi \tag{2.10}$$

and the energy due to the external potential, i.e. external potential energy is given by

$$V =< \psi \mid \hat{V_{ext}} \mid \psi >= \int d\vec{r}_1, d\vec{r}_2, .., \int d\vec{r}_N \psi^* \sum_i v_{ext}(\vec{r}_i) \psi = \int d\vec{r} v_{ext}(\vec{r}) \rho(\vec{r}) \quad (2.11)$$

One can also define the internal electronic energy (F) as the sum of the kinetic energy and internal potential energy, which is given by

$$F =< \psi \mid \hat{F} \mid \psi >=< \psi \mid \hat{T} + \hat{V_{int}} \mid \psi >= T + V_{int} \quad (2.12)$$

DFT gives a very convenient scheme to change the complex many-electron Hamiltonian (Eq. 2.4) with a much simpler non-interacting one-electron problem. The ground-state can be equivalently described by the one-particle charge density $\rho(\vec{r})$, and this observation is the central point of DFT. This theory started with two theorems of Hohenberg and Kohn (Hohenberg and Kohn, 1964) and subsequently formulated by Kohn and Sham (Kohn and Sham, 1965b).

2.3 Basics of Density Functional Theory

As discussed earlier, the many-electron Schrödinger equation reduces the complexity of the many-body Schrödinger equation, but practically it is not possible to obtain the analytical solution for the many-electron Schrödinger equation. Although the numerical solution is perfectly possible in theory, it is impossible to obtain the numerical solution in practice for more than a handful of electrons due to the limited computer resources such as speed and memory. In this regard, Thomas and Fermi were given one of the earliest prescriptions to calculate the solution for the many-electron Schrödinger equation in terms of the electron density rather than the wavefunction. However, in the Thomas-Fermi equation, the kinetic energy is approximate and does not include the inaccuracy exchange energy of an atom as a conclusion of the Pauli exclusion principle. Although, Dirac added a term for the exchange energy to the Thomas-Fermi model, i.e. Thomas–Fermi–Dirac theory, still remained inaccurate for most of the applications. In other words, representation of the kinetic energy, exchange energy, and complete neglect of electron-electron correlation are the major drawbacks of the Thomas-Fermi model. Later, Hohenberg and Kohn have given two remarkably powerful theorems by establishing the electron density as the central quantity to describe electron interactions and provides the solution of the many-electron Schrödinger equation to calculate the ground-state energy. This exact ground-state method known as density functional theory (DFT). Although, some of the alternative methods to DFT such as quantum Monte-Carlo (Foulkes et al., 2001) and configuration interaction methods (Bartlett and Stanton, 1994) give more accurate results than present DFT formulations, but demand more computational resources. However, the present DFT formulations are strike between the computational feasibility and accuracy. Hence, at present, DFT is the most popular method to perform first-principles calculations on extended systems.

2.3.1 The Hohenberg-Kohn Theorems

The introduction of DFT starts with the two Hohenberg-Kohn theorems:

Theorem 1:

For any system consisting of interacting electrons that are moving under the influence of an external potential $V_{ext}(\vec{r})$, the ground-state external potential $V_{ext}(\vec{r})$, and hence the ground-state total energy of the system is a unique functional of the ground-state electron density $n_0(\vec{\vec{r}})$ apart from trivial additive constant.

Hohenberg-Kohn Theorem 1 states that there is a one-to-one mapping between the ground-state electron density $n_0(\vec{r})$ and the external potential of the nuclei $V_{ext}(\vec{r})$, it means that for each non-degenerate ground-state electron density there exists exactly one external potential. In principle, one can obtain the electron density if one knows the external potential, and subsequently, one can solve the many-electron system bypassing the solution of Schrödinger equation and can obtain the information of the system. Or in other words, the ground-state energy can be obtained for a given external potential without dealing with a many-electron wave function, which is the solution of the Schrödinger equation and described as follows:

Using Eq. 2.6 and Eq. 2.12, one can express the internal electronic energy (F) of a system in its ground-state as

$$F = E - V_{ext}(\vec{r}) \tag{2.13}$$

where $V_{ext}(\vec{r}) = \int n(\vec{r}) v_{ext}(\vec{r}) d\vec{r}$. Since E and $V_{ext}(\vec{r})$ in Eq. 2.13 are functionals of the electron density, it follows that F is also a functional of the electron density. Further, the energy functional E[n($\vec{r}$)] can be written as

$$E[n(\vec{r})] = \int n(\vec{r}) v_{ext}(\vec{r}) dr + F[n(\vec{r})] \tag{2.14}$$

Correspondingly, a Hamiltonian ($\hat{H}$) for the system can be written as the electron wavefunction (ψ) that minimizes the expectation value of the $\hat{H}$ and gives the ground-state energy, E[n($\vec{r}$)] (assuming a non-degenerate ground-state),

$$E[n(\vec{r})] = \langle \psi | \hat{H} | \psi \rangle \tag{2.15}$$

where $\hat{H}$ is $\hat{F} + \hat{V_{ext}}$. Since the internal electron energy operator ($\hat{F}$) is the same for all N-electron systems, it follows that $\hat{H}$ can be completely defined by the number of electrons N, and the external potential $V_{ext}(\vec{r})$.

To derive the proof of the first theorem, let us consider that there are two different external potentials, $V_{ext1}(\vec{r})$ and $V_{ext2}(\vec{r})$, that give rise to the same ground-state electron density $n_0(\vec{r})$. The associated Hamiltonian, $\hat{H}_1$ and $\hat{H}_2$, therefore will have different ground-state wavefunctions, ψ_1 and ψ_2, respectively, that each yield ground-state electron density $n_0(\vec{r})$. Using the variational principle and $E[n(\vec{r})] = \langle \psi | \hat{H} | \psi \rangle$ together yields,

$$E_1^0 < \langle \psi_2 | \hat{H}_1 | \psi_2 \rangle = \langle \psi_2 | \hat{H}_2 | \psi_2 \rangle + \langle \psi_2 | \hat{H}_1 - \hat{H}_2 | \psi_2 \rangle = E_2^0 + \int n_0(\vec{r}) [v_{ext1}(\vec{r}) - v_{ext2}(\vec{r})] d\vec{r} \tag{2.16}$$

and,

$$E_2^0 < \langle \psi_1 | \hat{H}_2 | \psi_1 \rangle = \langle \psi_1 | \hat{H}_1 | \psi_1 \rangle + \langle \psi_1 | \hat{H}_2 - \hat{H}_1 | \psi_1 \rangle = E_1^0 + \int n_0(\vec{r}) [v_{ext2}(\vec{r}) - v_{ext1}(\vec{r})] d\vec{r} \tag{2.17}$$

where E_1^0 and E_2^0 are the ground-state energies of $\hat{H}_1$ and $\hat{H}_2$, respectively. Adding Eq. 2.16 and Eq. 2.17 result that

$$E_1^0 + E_2^0 < E_2^0 + E_1^0 \tag{2.18}$$

The contradiction in the above equation gives proof that the ground-state electron density uniquely determines the external potential $V_{ext}(\vec{r})$, to within a trivial additive constant. Finally, the proof of this first theorem states that the position of the nuclei and all ground-state electronic properties determined by the electrons because the point as mentioned earlier, $\hat{H}$ is completely defined by $v_{ext}(\vec{r})$ and N.

Theorem 2:

The ground-state energy can be obtained variationally: the density that minimizes the total energy is the exact ground-state density. A universal functional for the energy E[n($\vec{r}$)] can be defined in terms of the density. The exact ground state is the global minimum value of this functional.

The proof of the second theorem is as follows: As shown in the first theorem, the $V_{ext}(\vec{r})$ is uniquely determined by the $n(\vec{r})$, and since $V_{ext}(\vec{r})$ and N (N is the number of electrons), uniquely completely determines $\hat{H}$ (except in degenerate situations), therefore in turn uniquely determines the ground-state wavefunction, ψ. It means that ψ is a functional of $n(\vec{r})$. Since ψ is a functional of $n(\vec{r})$ and F is also a functional of $n(\vec{r})$ (See Eq. 2.13), then the expectation value of $\hat{F}$ is also a functional of $n(\vec{r})$, which is given by

$$F[n(\vec{r})] = \langle\psi|\hat{F}|\psi\rangle \tag{2.19}$$

The total energy of the system can be written as,

$$E[n(\vec{r})] = F[n(\vec{r})] + \int n(\vec{r})v_{ext}(\vec{r})d\vec{r} \tag{2.20}$$

where the functional F[n($\vec{r}$)] describes the kinetic energy and all the electron-electron interactions, i.e. internal electronic energy (Eq. 2.13). Since the treatment of internal electron energy is same for all systems and also it does not depend on the $V_{ext}(\vec{r})$, the F[n($\vec{r}$)] is a universal functional (has to be ideally the same for any system). In the ground-state the energy is defined by the unique ground-state density, $n(\vec{r})$, A density that is a ground-state density of some external potential, $V_{ext}(\vec{r})$ and associated with a Hamiltonian ($\hat{H}$), is known as V-representable and the energy functional associated with it can be written as,

$$E_v[n(\vec{r})] = \langle\psi|\hat{H}|\psi\rangle = F[n(\vec{r})] + \int n(\vec{r})V_{ext}(\vec{r})d\vec{r} \tag{2.21}$$

And, using the variational principle, a different density ($n'(\vec{r})$) which is not related to $V_{ext}(\vec{r})$, associated with a Hamiltonian ($\hat{H'}$) will necessarily give higher energy, i.e.

$$E_v[n'(\vec{r})] = \langle\psi^{'}|\hat{H}'|\psi^{'}\rangle = F[n'(\vec{r})] + \int n'(\vec{r})v_{ext}(\vec{r})dr > E_v[n(\vec{r})] \tag{2.22}$$

where ψ and $\psi^{'}$ are the wavefunction associated with the density $n(\vec{r})$ and $n'(\vec{r})$, respectively. From the above equation, the variational principle of the second theorem is obtained, and it follows that one can find the total energy of the system in the ground-state by minimizing the $V_{ext}(\vec{r})$ with respect to $n(\vec{r})$. The correct density for $V_{ext}(\vec{r})$ is the density that minimizes the energy is then the ground-state density. However, the Hohenberg-Kohn theorem does not provide any means to compute the ground-state of a system in practice and also do not offer a way of determining the exact form of the universal functional. Later, Kohn and Sham proposed a simple method for using DFT in practical calculations. This method is described in the following section.

2.3.2 The Kohn-Sham Formalism

The attempt was made to obtain the ground-state energy of interacting electron system as a functional of the ground-state density. In practice, it is not easy due to the lack of accurate approximations for the F[n($\vec{r}$)]. The Kohn-Sham formulation of DFT overcome this problem and gives good approximations to F[n($\vec{r}$)] (Kohn and Sham, 1965b). The key idea of Kohn-Sham formulation is essentially to map the interacting system with a non-interacting system. In general, the wavefunction of the non-interacting electrons is different from that of the interacting one; as a result, the density of the interacting electrons system and non-interacting electrons systems are also different. However, in the Kohn-Sham approach, a fictitious auxiliary system of non-interacting electrons system was introduced in such a way that its density is the same as that of the interacting electrons system and that can minimize energy functional of the true many-electronic system. In this fictitious system, the electron moves within a fictitious potential, which is known as effective Kohn-Sham potential, μ_{KS}. The Kohn-Sham method is still exact since it assumes the ground-state density of a non-interacting system same as the true ground-state density of an interacting system or real system. Considering the fact that there are no interactions between the electrons in the Kohn-Sham method, one can write the ground-state wavefunction in terms of simple single-particle wavefunctions which are known as Kohn-Sham orbitals. This wavefunction is far less complicated than the true, interacting or real system. However, one should make sure that the wavefunctions must follow the exchange anti-symmetry, and one can do this by placing the wavefunctions in a Slater determinant form (Slater, 1951)

$$\psi_{KS} = \frac{1}{\sqrt{N!}} \begin{vmatrix} \phi_1(\vec{r}_1) & \cdots & \phi_1(\vec{r}_N) \\ \vdots & \ddots & \vdots \\ \phi_N(\vec{r}_1) & \cdots & \phi_N(\vec{r}_N) \end{vmatrix} \tag{2.23}$$

$$\psi_{KS} = \frac{1}{\sqrt{N!}} \mid \phi_1(\vec{r}_1)\phi_2(\vec{r}_2)\cdots\phi_N(\vec{r}_N) \mid \tag{2.24}$$

where $\phi_i(\vec{r}_i)$ are the N lowest energy orbitals which are also known as Kohn-Sham orbitals corresponding to energy eigenvalues ε_i, satisfying the single-particle Schrödinger equation, i.e.

$$-\frac{1}{2}\nabla^2\phi_i(\vec{r}) + \mu_{KS}(\vec{r})\phi_i(\vec{r}) = \varepsilon_i\phi_i(\vec{r}) \tag{2.25}$$

The ground-state density (n($\vec{r}$)) can be obtained by solving the N one-electron Schrödinger equations, n($\vec{r}$) is

$$n(\vec{r}) = \sum_{i=1}^{N} \phi_i^*(\vec{r})\phi_i(\vec{r}) = \sum_{i=1}^{N} \mid \phi_i(\vec{r}) \mid^2 \tag{2.26}$$

According to the Hohenberg-Kohn theorem 2, one can extract the universal functional F[n($\vec{r}$)] by using the ground-state density. Using Eq. 2.12 and Eq. 2.19 the F[n($\vec{r}$)] can be written as

$$F_{KS}[n(\vec{r})] = \langle\psi_{KS}|\hat{F}|\psi_{KS}\rangle = \langle\psi_{KS}|\hat{T}+\hat{V}_{int}|\psi_{KS}\rangle = T_{KS} + V_{int}^{KS} \tag{2.27}$$

where T_{KS} and V_{int}^{KS} are the non-interacting kinetic energy and non-interacting internal potential energy, respectively. The T_{KS} and V_{int}^{KS} in terms of the Kohn-Sham orbitals is given by,

$$T_{KS} = -\frac{1}{2}\sum_{i=1}^{N}\int \phi_i^*(\vec{r})\nabla^2\phi_i(\vec{r})d\vec{r} \tag{2.28}$$

$$V_{int}^{KS} = V_H + V_{XC} \tag{2.29}$$

where $V_H(\vec{r})$ is classical electrostatic (Hartree) potential of the electrons and $V_{XC}(\vec{r})$ is the exchange-correlation potential. The $V_H(\vec{r})$ and $V_{XC}(\vec{r})$ is given by

$$V_H(\vec{r}) = \frac{e^2}{4\pi\varepsilon_0}\int d\vec{r'}\frac{n(\vec{r'})}{\mid \vec{r}-\vec{r'} \mid} \tag{2.30}$$

$$V_{XC}(\vec{r}) = \frac{\delta E_{xc}}{\delta n(\vec{r})} \tag{2.31}$$

and its corresponding exchange-correlation energy is E_{XC}. The E_{XC} is a combination of exchange energy (E_X) and correlation energy (E_C). The exchange of any two identical particles (electrons) results the anti-symmetric wavefunction, and that gives the E_X. E_C is the difference between exact many-body internal energy and F_{KS}. The E_X and E_C are given by

$$E_X = \frac{e^2}{4\pi\varepsilon_0}\sum_{i=1}^{N}\int d\vec{r}\int d\vec{r'}\frac{\phi_i^*(\vec{r})\phi_i(\vec{r'})\phi_j^*(\vec{r'})\phi_j(\vec{r})}{\mid\vec{r}-\vec{r'}\mid} \tag{2.32}$$

$$E_C = F - F_{KS} = T[n(\vec{r})] - T_{KS}[n(\vec{r})] + E_{ee}[n(\vec{r})] - E_H[n(\vec{r})] \tag{2.33}$$

From Eq. 2.32 & 2.33, $E_{XC}[n(\vec{r})]$ is

$$E_{XC}[n(\vec{r})] = T[n(\vec{r})] - T_{KS}[n(\vec{r})] + E_{ee}[n(\vec{r})] - E_H[n(\vec{r})] + E_X[n(\vec{r})] \tag{2.34}$$

The exact expression of F within the Kohn-Sham formulation is

$$F = T_{KS}[n(\vec{r})] + E_H[n(\vec{r})] + E_{XC}[n(\vec{r})] \tag{2.35}$$

Therefore, the energy functional E[n($\vec{r}$)] in the second theorem of Hohenberg-Kohn can be rewritten as

$$E[n(\vec{r})] = T_{KS}[n(\vec{r})] + E_H[n(\vec{r})] + \int v_{ext}(\vec{r})n(\vec{r})d\vec{r} + E_{XC}[n(\vec{r})] \tag{2.36}$$

If one knows the form of E_{XC} exactly, then the Kohn-Sham formulation gives the exact ground-state of an interacting many-body system. The E_{XC} and its approximations shall be discussed in the following section. The exchange-correlation energy includes all the important quantum-mechanical many-body effects and is a universal functional, valid for any external potential and any number of electrons. Using the variational principle, one can get the minimum value of the exact form the energy functional expressed in terms of the density of the non-interacting electron system. By varying over the orbitals $\phi(\vec{r})$ instead of the density n($\vec{r}$) itself, subject to the constraint $\langle\phi_i||\phi_j\rangle = \delta_{ij}$, and obtain the effective one-electron KS equation given by

$$H_{KS}\phi_i(\vec{r}) = [-\frac{\hbar^2}{2m_e}\nabla^2 + V_{ext}(\vec{r}) + \frac{e^2}{4\pi\varepsilon_0}\int\frac{n(\vec{r'})}{\mid\vec{r}-\vec{r'}\mid}d\vec{r'} + \frac{\delta E_{xc}}{\delta n(\vec{r})}]\phi_i(\vec{r}) \tag{2.37}$$

Since the potentials V_H and V_{XC} depend on the density, the KS equation may be solved by using the self-consistent numerical method, as shown in Figure 2.1, starting from an initial guess for the charge density. Using the initial charge density, one can determine the Hamiltonian by constructing V_H and V_{XC}. Then, one can find a new charge density by solving this Hamiltonian. These steps are iterated until the self-consistency condition is satisfied. Typically, the self-consistency check is done for the total energy or charge density (Martin, 2004).

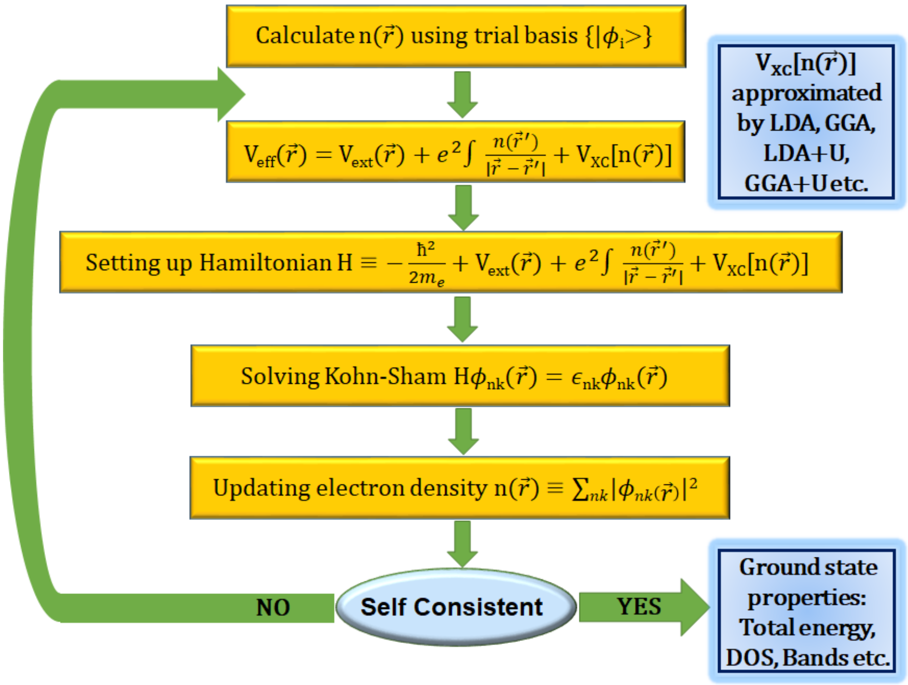
Calculate n($\vec{r}$) using trial basis {|ϕ_i>}
$V_{eff}(\vec{r}) = V_{ext}(\vec{r}) + e^2\int \frac{n(\vec{r}')}{|\vec{r}-\vec{r}'|} + V_{XC}[n(\vec{r})]$
$V_{XC}[n(\vec{r})]$ approximated by LDA, GGA, LDA+U, GGA+U etc.
Setting up Hamiltonian $H \equiv -\frac{\hbar^2}{2m_e} + V_{ext}(\vec{r}) + e^2\int \frac{n(\vec{r}')}{|\vec{r}-\vec{r}'|} + V_{XC}[n(\vec{r})]$
Solving Kohn-Sham $H\phi_{nk}(\vec{r}) = \epsilon_{nk}\phi_{nk}(\vec{r})$
Updating electron density $n(\vec{r}) \equiv \sum_{nk}|\phi_{nk}(\vec{r})|^2$
NO
Self Consistent
YES
Ground state properties: Total energy, DOS, Bands etc.

Figure 2.1 Algorithmic flowchart representing the iterative procedure to solve the Kohn-Sham equations.

2.4 Exchange-Correlation

The Kohn-Sham formulation explicitly separates the non-interacting physical properties (T_{KS} and V_H) from the remaining interacting part exchange-correlation functional. One should solve the many-body Schrödinger equation to exactly describe the correlation properties. Moreover, the computational evolution of E_X is more expensive than computing T_{KS} and E_H. Therefore, approximating the exchange and correlation energy is a good choice in practical calculations. The approximation usually groups the exchange and correlation energy into the $E_{XC}[n(\vec{r})]$.

The electron-electron coupling constant (λ) is established between the non-interacting system and interacting system. The value of λ varies in the range of $0 \leq \lambda \leq 1$. Each value of λ generates one system starting from the non-interacting system (λ=0) to the true interacting system (λ=1). Since the external fictitious potential will be added to make sure that the ground-state density is equal to n($\vec{r}$) for all values of λ, the density unchanged, and hence the continues path between the two systems is called the adiabatic connection. The $E_{XC}[n(\vec{r})]$ is given by,

$$E_{XC}[n(\vec{r})] = \frac{1}{2}\int n(\vec{r})d\vec{r}\int \frac{n_{xc}(\vec{r},\vec{r'})}{\mid \vec{r}-\vec{r'} \mid}d\vec{r'} \tag{2.38}$$

where $n_{xc}(\vec{r},\vec{r'})$ is the coupling factor averaged exchange-correlation hole which is given by

$$n_{xc}(\vec{r}) = \int_0^1 n_{xc}^{\lambda}(\vec{r},\vec{r'})d\lambda \tag{2.39}$$

From Eqns. 2.38 and 2.39, one can define the exchange-correlation energy per particle or exchange-correlation density, ε_{xc}:

$$\varepsilon_{xc}[n(\vec{r})] = \int \frac{n_{xc}(\vec{r},\vec{r'})}{\mid \vec{r}-\vec{r'} \mid}d\vec{r'} \tag{2.40}$$

The exchange-correlation hole can be separated into the summation of two parts such as exchange and correlation holes, known as Fermi hole and Coulomb hole, respectively.

$$n_{xc}(\vec{r},\vec{r'}) = n_x(\vec{r},\vec{r'}) + n_c(\vec{r},\vec{r'}) \tag{2.41}$$

whereby the exchange hole (Fermi hole) and correlation hole (Coulomb hole) is defined as

$$n_x(\vec{r},\vec{r'}) = n_{xc,\lambda=0}(\vec{r},\vec{r'}) \tag{2.42}$$

$$n_c(\vec{r},\vec{r'}) = n_{xc}(\vec{r},\vec{r'}) - n_x(\vec{r},\vec{r'}) \tag{2.43}$$

The exchange hole, n_x can be defined from the Hartree-Fock expression of the exchange energy.

$$E_x[n(\vec{r})] = \frac{1}{2}\int n(\vec{r})d\vec{r}\int \frac{n_x(\vec{r}\vec{r'})}{\mid \vec{r}-\vec{r'} \mid} \tag{2.44}$$

Thus, using Eq. 2.40 & Eq. 2.44, the simple or general form of exchange-correlation functional can be written as,

$$E_{XC}[n(\vec{r})] = \int n(\vec{r})\varepsilon_{xc}[n(\vec{r})]d\vec{r} \tag{2.45}$$

The exact ground-state can be reached if one has known the exact form of the exchange-correlation density.

2.4.1 E_{XC} - Approximations

In practical calculations, the unknown form of exchange-correlation energy directs to approximate the exchange-correlation energy functional. This exchange-correlation functionals can be characterized by the way in which the density surrounding each electron is sampled, which requires the construction of $\varepsilon_{xc}[n(\vec{r})]$. There exist several exchange-correlation functionals and are classified into two types, one is empirical or semi-empirical functionals, and another one is non-empirical functionals. In the empirical functionals, some of the information used to define them is derived from experimental results on particular materials or chemicals, and the non-empirical functionals are defined purely from the results of first-principles calculations. Some of the approximated functionals are described below.

2.4.2 Local Density Approximation (LDA)

The first-ever, simplest, most important and commonly used form of exchange-correlation functional was proposed by Hohenberg-Kohn (Hohenberg and Kohn, 1964), i.e. Local Density Approximation (LDA). In this approximation, the exchange-correlation energy of a system associated with the homogeneous electron gas of the same density n($\vec{r}$). And, the value of $\varepsilon_{xc}[n(\vec{r})]$ is simply a function of the density at the same point, $\vec{r}$ (or only dependent on the local density), which is given as,

$$E_{XC}^{LDA} = \int n(\vec{r})\varepsilon_{xc}^{hom}[n(\vec{r})]d\vec{r} \tag{2.46}$$

where ε_{xc}^{hom} is the exchange-correlation energy density of a homogeneous electron gas with density n($\vec{r}$). As mentioned earlier, E_{XC} is the combination of E_X and E_C, and hence one can decompose E_{XC} into the contribution of E_X and E_C. The E_X is analytically derived by Dirac (using Dirac exchange formula) given as (Dirac, 1930),

$$E_x[n(\vec{r})] = -\frac{3}{4}(\frac{9}{4\pi^2}^{1/3})\frac{1}{r_s} \approx -\frac{0.4582}{r_s} \tag{2.47}$$

where r_s is the Wigner-Seitz radius. And, another contribution E_C can be obtained from an interpolation formula (Hubbard, 1958), that basically connects the known form of $\varepsilon_c^{hom}[n(\vec{r})]$ at high and low density limits. An interpolation formula which is used commonly to obtain E_C was given by Perdew and Zunger (Perdew and Zunger, 1981), in this, the interpolation coefficients are derived from quantum Monte-Carlo data of homogeneous electron gas generated by Ceperley and Alder, which yield essentially exact results (Ceperley and Alder, 1980). The resultant E_{XC} has been fitted by a number of analytic forms all of which yield exact results (Perdew and Zunger, 1981; von Barth and Hedin, 1972; Vosko et al., 1980).

Although LDA is a simple approximation and works good for metallic systems, it gives relatively higher binding energy. LDA is not a good choice, particularly for semiconductors and molecules due to the overestimation of the binding energies. And also, it is not found to be successful in the crystal phase stability calculations, for example, in the case of SiO_2, it favors the high pressure phase than the zero pressure phase. In addition to this, it also underestimates the phase transition pressure in diamond, Si, Ge, etc..

2.4.3 Generalized Gradient Approximation (GGA)

Hohenberg and Kohn proposed improvement approximation over LDA, which is known as the gradient expansion approximation (GEA) (Hohenberg and Kohn, 1964). The GEA takes into account the higher-order density gradient expansion terms. The GEA does not integrate exchange-hole to -1; this leads to the violation of sum rule. The generalized gradient approximation (GGA) restores the sum rule, in which the GGA exchange-correlation hole construct by terminating the GEA exchange-correlation hole in real-space. To terminate this GEA exchange-correlation hole in real-space, Perdew et al. formulated a cut-off procedure using gradient functions (Perdew et al., 1992). The GGA can be conveniently written with the introduction of an analytic function which is known as the enhancement factor, $F_{XC}[n(\vec{r}), \nabla n(\vec{r})]$, that directly modifies the LDA energy density, and the GGA exchange-correlation energy is given by

$$E_{XC}^{GGA}[n(\vec{r})] = \int n(\vec{r}) \varepsilon_{xc}^{hom} F_{XC}[n(\vec{r}), \nabla n(\vec{r})] d\vec{r} \tag{2.48}$$

A non-empirical form of exchange enhancement factor in the GGA functional was provided by Perdew and Wang, later Perdew, Burke and Ernzerhof modified to give a simplified form to the exchange enhancement factor, known as PBE (Perdew et al., 1996). Although, GGA retain the correct features of LDA and also overcome some of the drawbacks in LDA with the improved results in atomic and molecular energies, the tendency to over binding error in solids and molecules, crystal phase stability, etc.. However, both GGA and LDA underestimate the bandgaps (for example, in the case of Mott insulators like transition metal compounds, rare earth compounds) due to the local nature of the functionals.

2.4.4 Hybrid Functionals

In hybrid functionals, the exchange-correlation energy approximated by combining Hartree-Fock (exact) exchange energy and with the rest of exchange and correlation energy from other sources such as LDA and GGAs, and it's general form is given as

$$E_{XC}^{hybrid} = \alpha(E_{XC}^{HF} - E_{X}^{GGA}) + E_{XC}^{GGA} \tag{2.49}$$

where α is the coefficient that determines the quantity of exact exchange mixing, which cannot be assigned from first-principles and its accurate value depends upon the (semi-empirical) fitting to the atomic and molecular data. Some of the most popular forms of hybrid functionals are B3LYP (Becke, three-parameter, Lee-Yang-Parr) and HSE (Heyd-ScuseriaErnzerhof) (Heyd et al., 2003). In 1993, Axel Becke introduced this hybrid approach to construct exchange-correlation (density functional) approximation with the exchange mixing (α) is $\frac{1}{2}$, which is known as half-and-half functional, given as (Becke, 1993)

$$E_{XC} = \frac{1}{2}E_{X}^{HF} + \frac{1}{2}E_{XC,\lambda=1}^{DF} \tag{2.50}$$

where $E_{XC,\lambda=1}^{DF}$ is obtained from a density functional approximation such as LDA.

In order to enhance the computational efficiency, the HSE exchange-correlation functional uses an error function screened Coulomb potential to calculate the exchange portion of the energy,

$$E_{XC}^{HSE} = \alpha E_{X}^{HF,SR}(\omega) + (1-\alpha)E_{X}^{PBE,SR}(\omega) + E_{X}^{PBE,LR}(\omega) + E_{C}^{PBE} \tag{2.51}$$

where ω is a variable parameter which controls the short-range interaction. $E_{X}^{HF,SR}(\omega)$ is the short range Hartree-Fock (exact) exchange functional, $E_{X}^{PBE,SR}(\omega)$ and $E_{X}^{PBE,LR}(\omega)$ are the short and long range components of the PBE exchange functional, respectively, and E_{C}^{PBE} is the correlation functional of PBE.

Hybrid functionals greatly improve the many molecular properties which are poorly described by LDA or GGA. Although, hybrid functionals give results with greater accuracy but not generally used in solid-state system because of the computational expense to calculate E_{X}^{HF}. One can use hybrid functionals to obtain the properties of solid-state systems with great accuracy, if not considering the huge computational resources. In spite of this, hybrid functionals are a good choice of functional to calculate molecular properties such as atomization energies, bond lengths and vibration frequencies.

2.4.5 Beyond LDA/GGA: LDA+U/GGA+U

As mentioned above, LDA/GGA provides a reliable ground-state electronic structure of the solid system but not adequate to provide an electronic structure of the systems which have the atoms that contain the partially filled d or f shells (valence electrons). For example, in the case of the transition metal oxides systems, the LDA predicts the metallic ground-states while experimentally observed to be insulators (Terakura et al., 1984b,a). In LDA, the energy functional depends on the number of electrons, N. Both E(N) and its derivative $\frac{\partial E}{\partial N}$ are continuous for an integral value of N. But the derivative which has a significant contribution in the bandgap has discontinuity for an exact functional. And also, the exchange-correlation potential is the same for both occupied and unoccupied states; as a result, it fails to reproduce orbital energies, $\varepsilon_i = \frac{\partial E}{\partial n_i}$ (where n_i is the orbital occupation numbers). Subsequently, LDA/GGA functionals tend to over-delocalize electrons and inadequate to describe the strong Coulomb repulsion that exists between the localized 3d or 4f electrons of metal ions (Hüfner, 1994). This inadequacy of strong Coulomb repulsion in the localized electrons can be resolved by incorporating explicit Coulomb interaction (U) of localized electrons in a Hartree-Fock (HF) like approach to the LDA, i.e. LDA+U method (Anisimov et al., 1991; Solovyev et al., 1994; Liechtenstein et al., 1995). This LDA+U method separates electrons into two subsystems. One is localized d or f electrons for which the explicit Coulomb d-d interaction has taken into account, and another one is delocalized s and p electrons, i.e. the wide band electrons described by using LDA or GGA. The correct energy functional can be defined in terms of density matrix elements, $\{\rho\}$, rather density,

$$E^{LDA+U}[n^{\sigma}(\vec{r}),\{\rho^{\sigma}\}] = E^{LDA}[n^{\sigma}(\vec{r})] + E^{U}[\{\rho^{\sigma}\}] - E^{dc}[\{\rho^{\sigma}\}] \tag{2.52}$$

where, $n^{\sigma}(\vec{r})$ is the charge density for electrons with spin σ. The first term is the Kohn-Sham energy functional, and the second term describes the electron-electron interactions in the HF correction to the functional (or describes the HF correction to the functional), expressed as,

$$\begin{aligned} E^{U}[\{\rho\}] =& \frac{1}{2}\sum_{\{m\},\sigma}\{\langle m,m''|V_{ee}|m',m'''\rangle\rho^{\sigma}_{mm'}\rho^{-\sigma}_{m''m'''} \\ &+ (\langle m,m''|V_{ee}|m',m'''\rangle - \langle m,m''|V_{ee}|m''',m'\rangle)\rho^{\sigma}_{mm'}\rho^{\sigma}_{m''m'''}\} \end{aligned} \tag{2.53}$$

where index m labels the localized states of the atomic site, I. Further, the matrix elements of the screened Coulomb interaction among the correlated electrons, i.e. V_{ee} in the above equation can be expressed in terms of Slater integrals F^k and the spherical harmonics.

$$\langle m,m^{''}|V_{ee}|m^{'},m^{'''}\rangle = \sum_k a_k(m,m^{'},m^{''},m^{'''})F^k \tag{2.54}$$

where,

$$a_k(m,m^{'},m^{''},m^{'''}) = \frac{4\pi}{2k+1}\sum_{q=-k}^{+k}\langle lm|Y_{kq}|lm^{'}\rangle\langle lm^{'}|Y^*_{kq}|lm^{'''}\rangle \tag{2.55}$$

and $0 \leq k \leq 2l$. The Slater integrals, F^k are often parameterized and expressed in terms of onsite Coulomb (U) and exchange (J) parameters.

Finally, the third term in the Eq. 2.52 is the double-counting term. Since the U value has been added explicitly for the localized electrons and the energy functional given by LDA already consists of a contribution from the electron-electron interaction, one has to remove the energy contribution of these orbitals included in the LDA energy functional.

$$E^{dc}[\{\rho^\sigma\}] = \frac{1}{2}Un_{tot}(n_{tot}-1) - \frac{1}{2}J[n^{\uparrow}(n^{\uparrow}-1)+n_{\downarrow}(n_{\downarrow}-1)] \tag{2.56}$$

where, $n_{tot} = Tr[\rho]$ and $n_\sigma = Tr[\rho\sigma]$.

The on-site Coulomb (U) parameter can be determined using the linear response method (Cococcioni and De Gironcoli, 2005). Briefly, the U parameter may be defined as the second-order derivative energy functional (E) with respect to the on-site occupation at the site I (n_I), $U = \partial^2E/\partial n_I^2$. It can be rewritten in terms of the first derivatives of the on-site occupation with respect to perturbations of the Kohn-Sham potential (α_J), U = (1/χ_0 – 1/χ), where χ_0 and χ are the non-interacting and interacting (self-consistent) density response matrices.

Drudarev et al. proposed a simplified expression of the LDA+U energy functional, given by (Dudarev et al., 1998)

$$E^{LDA+U}[n^\sigma(\vec{r}),\{\rho^\sigma\}] = E^{LDA}[n^\sigma(r)] + \frac{U_{eff}}{2}\sum_\sigma[(\sum_m \rho^\sigma_{mm}) - (\sum_{m,m^{'}} \rho^\sigma_{mm^{'}}\rho^\sigma_{m^{'}m})] \tag{2.57}$$

where U_{eff} is the difference between U and J parameters.

2.5 The Plane Wave and Pseudopotential Implementation of DFT

In this section, the plane wave pseudopotential approach to solve the Kohn-Sham equations shall be described. The plane wave basis set to represent the orbitals, and the key idea of the pseudopotential was to represent the nuclei and core electrons. This approach is well suitable to describe the infinite periodic solids and well established in the condensed matter physics community.

2.5.1 Bloch's theorem

Bloch's theorem state that the wavefunction of an electron ($\psi_{j,k}$) within a periodic potential can be chosen to have the form of a plane wave times a function with the periodicity of the periodic lattice (or Bravais lattice) $u_j(\vec{r})$ (Ashcroft and Mermin, 1976).

$$\psi_{j,\vec{k}} = u_j(\vec{r})e^{i\vec{k}.\vec{r}}, \tag{2.58}$$

where j represents the band index and $\vec{k}$ is continuous wavevector that is confined to the first Brillouin zone of the reciprocal lattice. And, $u_j(\vec{r}+\vec{R}) = u_j(\vec{r})$ for all $\vec{R}$ (crystal lattice vectors) in the Bravais lattice. Since $u_j(\vec{r})$ has the same periodicity as the direct lattice, it can be expressed in terms of a discrete plane wave basis set with wavevectors $\vec{G}$ that are reciprocal lattice vectors of the crystal, i.e.

$$u_j(\vec{r}+\vec{R}) = \sum_{\vec{G}} c_{j,\vec{G}} e^{i\vec{G}.\vec{R}} \tag{2.59}$$

where $\vec{G}.\vec{R}$ = 2πm (m is an integer) and $c_{j,\vec{G}}$ is the plane wave coefficients. From Eq. 2.58 and 2.59, the electron wavefunction can be expanded in terms of a linear combination of plane waves,

$$\psi_{j,\vec{k}} = \sum_{\vec{G}} c_{j,\vec{k}+\vec{G}} e^{i\vec{k}+\vec{G}.\vec{r}} \tag{2.60}$$

2.5.2 Kohn-Sham Equations in Plane Wave Form

There are several possible choices for the basis set, e.g. Gaussian functions, localized atomic like orbitals (atomic orbitals, muffin-tin orbitals), plane waves, etc.. The plane waves are a simple way of representing electron wavefunctions, and they offer a complete basis set that is independent of the type of crystal and treats all areas of space equally. Results, presented in this thesis are obtained from the plane wave based methods, where each Kohn-Sham wavefunction can be as a sum of plane waves, which can be expressed as,

$$\psi_{n\vec{k}}(\vec{r}) = \sum_{\vec{G}} c_{n\vec{k}}(\vec{G}) \times \frac{1}{\sqrt{\Omega}} e^{i(\vec{k}+\vec{G}).\vec{r}} \tag{2.61}$$

where $c_{n\vec{k}}$ are the expansion coefficients of the wavefunction in a plane wave basis $e^{i(\vec{k}+\vec{G}).\vec{r}}$, $\frac{1}{\sqrt{\Omega}}$ preserves the normalization of the wavefunction. $\vec{G}$ and $\vec{k}$ are the Bloch wave and reciprocal lattice vectors, respectively, and n is the band index.

And, using the above form of wavefunctions, the set of Kohn-Sham equations can be represented in a reciprocal-space (Payne et al., 1992),

$$\sum_{G^{'}} [\frac{\hbar^2}{2m_e} \mid \vec{k}+\vec{G} \mid^2 \delta_{GG^{'}} + V_{ext}(G-G^{'}) + V_H(G-G^{'}) + V_{XC}(G-G^{'})] c_{n\vec{k}}(\vec{G}) = \varepsilon_{n\vec{k}} c_{n\vec{k}}(G) \tag{2.62}$$

In this equation, left hand side, the kinetic energy term is diagonal, and the remaining three terms are the Fourier representation of external, Hartree and exchange-correlation potentials, respectively, which can be represented as,

$$V(G-G^{'}) = \frac{1}{\Omega} \int_{\Omega} V(\vec{r}) e^{-i(G-G^{'})}.\vec{r} d^3\vec{r} \tag{2.63}$$

The basis set with an infinite number of plane waves gives the complete exact result. Considering the fact that the lower end of the kinetic energy is most important, in practical, plane wave expansion can be truncated to a finite number of plane waves with a kinetic energy cut-off (E$_{cut}$),

$$\frac{\hbar^2}{2m} \mid k = \vec{G}_{max} \mid^2 \leq E_{cut} \tag{2.64}$$

The advantage of the plane wave basis set is the accuracy can be systematically improved by increasing the E$_{cut}$. And, the disadvantage is, a very large number of plane waves are required to describe the nodal structure of wavefunction in the core regions of atoms.

2.5.3 Pseudopotentials

The plane wave basis set expansion, and pseudopotential approximation has been widely used together from the early times of electronic-structure calculations (Pickett, 1989; Phillips, 1958; Phillips and Kleinman, 1959). The key idea behind using the pseudopotential is to minimize the size of the basis set. The reason for this is, in condensed matter systems, the orbitals tend to oscillate (nodal structure) very rapidly in the core region.

In order to describe this oscillation in the core regions, the number of basis set which maintains the orthogonality between the core and valance electrons is very large than would be required with a localized basis set. However, in general, the core-electrons are of minimal interest and also remain almost the same in different chemical environments. The pseudopotential approximation project out the chemically inert core electrons by replacing the strong ionic potential v$_{ion}(\vec{r})$ in the core region with a weaker pseudopotential $v_{ion}^{PS}(\vec{r})$ and retains their properties outside chosen cut-off radius (r$_c$) (Pickett, 1989). And also, the pseudo-wavefunctions ($\psi^{PS}(\vec{r})$) and the all-electron wavefunctions ($\psi^{AE}(\vec{r})$) are identical outside r_c. The $\psi^{PS}\vec{(r)}$ does not possess the nodal structure of wavefunction and can be described with a reasonable number of plane waves. The formalism of pseudopotential is shown schematically in Figure 2.2.

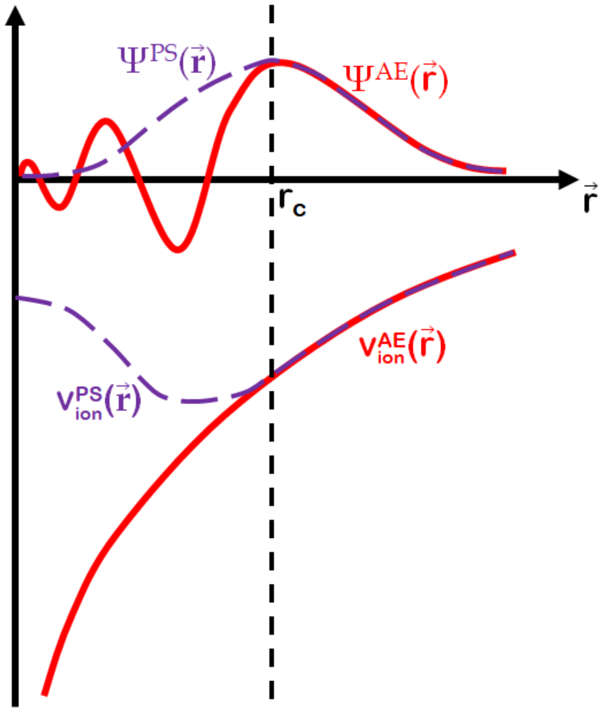

Figure 2.2 Schematic representation of pseudopotential formalism. The dashed line shows the pseudopotential $v_{ion}^{PS}(\vec{r})$ and corresponding pseudo wavefunction $\psi^{PS}(\vec{r})$, while the solid line represents all-electronic wavefunction $\psi^{AE}(\vec{r})$ and ionic potential, $v_{ion}^{AE}(\vec{r})$. The cut-off radius (r_c) represented by the vertical dashed line, at this point the pseudo quantities ($\psi^{PS}(\vec{r})$ and $v_{ion}^{PS}(\vec{r})$) matches with the all-electron quantities ($\psi^{AE}(\vec{r})$ and $v_{ion}^{AE}(\vec{r})$).

Among the various proposed methods to generate pseudopotentials (Phillips, 1958; Phillips and Kleinman, 1959), the pseudopotentials generated from empirical pseudopotentials, ab-initio pseudopotential schemes were successfully used to calculate the properties of the systems (Cohen and Bergstresser, 1966; Pickett, 1989). Currently, one of the most popular ab-initio pseudopotential schemes is the norm-conserving pseudopotentials (NCCP) scheme (Hamann et al., 1979). The NCCP is then constructed by satisfying the four conventional general desirable criteria: (i) $\psi^{AE}(\vec{r})$ and $\psi^{PS}(\vec{r})$ must be identical at outside the r_c (ii) the pseudo and all-electron valence eigenvalues must be equal for a chosen reference configuration (iii) norm conservation; the charge enclosed within r_c must be equal for both the pseudo and all-electronic wavefunctions, $\int_0^{r_c} \mid \psi_l^{PS}(\vec{r}) \mid^2 d\vec{r} = \int_0^{r_c} \mid \psi_l^{AE}(\vec{r}) \mid^2 d\vec{r}$, and is normalized, $\int_0^{\infty} \mid \psi_l^{PS}(\vec{r}) \mid^2 d\vec{r} = \int_0^{\infty} \mid \psi^{AE}(\vec{r}) \mid^2 d\vec{r}\vec{r} = 1$, (iv) there must be no nodes of the $\psi^{PS}(\vec{r})$. $\psi^{PS}(\vec{r})$ and it's first and second derivatives must be continues at r_c.

The NCCP formalism constructs the pseudopotential by following the above conditions and generate pseudo wavefunction, ψ_l^{PS}(r) which do not contain nodes and conserve the all-electron wavefunction, ψ_l^{AE}(r). Further, preserves all-electron eigenvalues, ε_l, for a given reference configuration, where subscript l represents the quantum numbers.

The ionic pseudopotential is generated by inverting the Shrödinger equation,

$$\begin{aligned}
[-\frac{\hbar^2}{2m_e}\nabla^2 &+ \frac{l(l+1)}{2\vec{r}^2} - \frac{Z}{\vec{r}} + v_H(\vec{r}) + v_{xc}(\vec{r})]\psi_l^{AE}(\vec{r}) = \varepsilon_l \psi_l^{AE}(\vec{r}) \\
\Rightarrow v^{PS}_{ion,l}(\vec{r}) &= \varepsilon_l - v_H^{PS}(\vec{r}) - v_{xc}^{PS}(\vec{r}) - \frac{(l(l+1))}{2\vec{r}^2} + \frac{1}{2\psi_l^{PS}(\vec{r})}\nabla^2\psi_l^{PS}(\vec{r}) \quad (2.65)
\end{aligned}$$

where $v_H^{PS}(\vec{r})$ and $v_{xc}^{PS}(\vec{r})$ are calculated from $\psi_l^{PS}(\vec{r})$, and the norm-conserving pseudopotentials have different radial components for each angular momentum (l). As a consequence of this procedure, there is a separate pseudopotential must be generated for each l, i.e. orbital dependent pseudopotential v_l^{PS}. The pseudopotential operator $\hat{V}(\vec{r})$ can be written in semi-local form (Hamann et al., 1979; Bachelet et al., 1982), that is local in the radial variable r, and non-local in the angular variables θ and φ,

$$\hat{V}^{PS}(\vec{r}) = v_{LOC}^{PS}(\vec{r}) + \sum_l \delta v_l^{PS}(\vec{r})\hat{P}_l \quad (2.66)$$

where v_{LOC}^{PS} is local potential and$\hat{P}_l$ project the angular moment component of the semi-local, δv_l^{PS}, the $\delta v_l^{PS} = v_{ion,l}^{PS}(\vec{r}) - v_{LOC}^{PS}(\vec{r})$. Kleinman and Bylander re-casted the pseudopotential procedure and observed the greater efficiency could be attained by extending the separable non-local form to the radial component which yields (Kleinman and Bylander, 1982),

$$\delta v^{PS}_{KB,l} = \frac{|\delta v^{PS}_l \Phi^0_l(\vec{r})\rangle \langle \Phi^0_l(\vec{r}) \delta v^{PS}_l(\vec{r})|}{\langle \Phi^0_l(\vec{r})| \, \delta v^{PS}_l(\vec{r}) \, |\Phi^0_l(\vec{r})\rangle} \tag{2.67}$$

where $\Phi^0_l(\vec{r})$ are the pseudo-wavefunctions for the atomic system calculated with $\delta v^{PS}_l(\vec{r})$. In general, the number of projections for each l state for a plane wave expansion of dimensional N_{pw} is $\sim (\frac{N^2_{pw}+N_{pw}}{2})$, whereas the KB-pseudopotential evaluates with the N_{pw} projections, that means linearly with the number of plane waves and reduces the computational cost.

2.5.4 The Projector Augmented Wave Method

The projector-augmented-wave (PAW) method was introduced by Blöchl in 1994 (Blöchl, 1994). This method elegantly combines the idea of the pseudopotential method and augmented wave method. It turned out to be an accurate method to calculate electronic structure and facilitate the DFT calculations to be performed with greater computational efficiency. This method reminiscent of the augmented wave method but with simpler energy and potential independent basis, as adapted in the pseudopotential method. The PAW approach addresses the nodal structure issue by transforming the rapidly oscillating true all-electron single particle KS wavefunction $|\tilde{\psi}_n\rangle$ into computationally convenient smooth pseudo wavefunction $|\psi_n\rangle$. In this formalism, the all-electron wavefunction $|\psi_n\rangle$ is derived from the pseudo wavefunction $|\tilde{\psi}_n\rangle$ by means of a linear transformation:

$$|\tilde{\psi}_n\rangle = |\tilde{\psi}_n\rangle + \sum_i (|\phi_i\rangle - |\tilde{\phi}_i\rangle) \langle \tilde{p}_i| \, |\tilde{\psi}_i\rangle \tag{2.68}$$

where, the index i is the atom site index at R_i, and the index n is a cumulative index for band, k-point and spin. All-electron partial waves ($|\phi_i\rangle$) are the solutions of the radial Schrödinger for the isolated atom. Beyond the augmentation, i.e. outside a core radius, r_c, the pseudo partial waves ($|\tilde{\phi}_i\rangle$) and ($|\phi_i\rangle$) are identical, i.e. $|\phi_i\rangle = |\tilde{\phi}_i\rangle$. The $|\phi_i\rangle$ and $|\tilde{\phi}_i\rangle$, and their derivatives are equal at the boundary r^l_c. Within the core radius, the projector function (p_i) for each $|\tilde{\phi}_i\rangle$ obeys the following relation.

$$\langle \tilde{p}_i| \, |\tilde{\phi}_i\rangle = \delta_{ij} \tag{2.69}$$

The all-electron charge density in the PAW method can be written as, $\rho = \tilde{\rho} + \rho^1 - \tilde{\rho^1}$. Where ρ is the smooth pseudo-charge density calculated directly from the pseudo wavefunctions on a plane wave grid, ρ^1 and $\tilde{\rho^1}$ are the on-site charge densities, which are treated on radial support grids localized around each atom. The ρ^1 and $\tilde{\rho^1}$ are identical within the augmentation spheres around each atom. An additional compensation charge density is added to both the pseudo density and all-electron density to vanish the multi-pole moments of the terms $\rho^1 - \tilde{\rho^1}$. Thus the electrostatic potential due to these terms vanishes outside the augmentation spheres around each atom. Similarly, the energy also can be written as a sum of three terms and one can derive the expressions of Kohn-Sham equations by functional derivatives of the total energy. In the PAW method, the core states are assumed to be unaffected by the ions' environment, i.e. frozen-core approximation. Although, the PAW method is accurate within DFT framework without some approximations, i.e. frozen-core approximation, the convergence of partial wave expansion, expansion of auxiliary wavefunction with finite plane waves, etc.. Despite these facts, the PAW method provides access to obtain the full wavefunction, charge density and spin density with a much simpler basis set.

2.6 Technical Aspects

The theoretical results presented in this thesis were calculated using the PAW method as implemented in the Vienna Ab-initio Simulation Package (VASP) (Kresse and Hafner, 1993; Kresse and Furthmüller, 1996). The technical details regarding the choice of exchange-correlation functional, cut-off energy of the plane wave, and on-site Coulomb (U) and exchange (J) parameters of transition metals are provided as necessary in the results chapters.

Chapter 3

Route to Achieving Giant Magnetoelectric Coupling in $BaTiO_3/Sr_2CoO_3F$ Perovskite Heterostructures

In this chapter, the spin state switching of Co atom in a perovskite oxyhalide Sr_2CoO_3F (SCOF) by means of altering polarization directions of the $BaTiO_3$ (BTO) shall be discussed, where SCOF is sandwiched between two ferroelectric BTO layers. Controlling the spin state of Co atom in SCOF from high-spin state to low-spin state by changing the relative orientation of the ferroelectric polarization of BTO with respect to SCOF gives rise to an unexpected, giant magnetoelectric coupling. Such spin manipulation (or spin switching) in magnetic materials by inducing the electric polarization opens possibilities to design and develop advanced spintronic devices, in particular, storage devices where the magnetic state can be controlled by an electric field.

3.1 Introduction

The multiferroic materials inherently exhibit both magnetic and electric polarization that make them to be potential candidates in magnetoelectric (ME) applications. Multiferroic materials with strong ME coupling may provide a solution to many of the current challenges in conventional magnetic storage media like achieving high-speed switching, low power consumption, and high operational stability simultaneously (Eerenstein et al., 2006; Trassin, 2015). A strong ME coupling in a material enables to control the magnetic properties by means of an electric field and *vice versa*, a functionality that is promising for a wide range of potential applications such as sensors, high-density non-volatile memory devices, and ME actuators (Scott, 2012; Hu et al., 2011, 2012; Wang et al., 2014). In transition metals, the partially filled *d* states are responsible for the occurrence of magnetism. On the other hand, the empty *d* states may exhibit ferroelectricity. Consequently, it is very difficult to observe the coexistence of ferroelectricity and magnetism at room temperature in an intrinsic material (Scott, 2007). Thus, the multiferroic heterostructures and composites that comprise both magnetic materials and ferroelectric oxides could be suitable alternatives to achieve the coexistence of ferroelectricity and magnetism that results in the strong ME coupling at room temperature, as was reported in recent years (Vaz et al., 2010; Scott, 2013; Lu et al., 2015; Ma et al., 2011; Stroppa et al., 2011; Fechner et al., 2012; Di Sante et al., 2013; Stroppa et al., 2013).

A heterostructure of two or more different crystalline semiconductor materials forms the interface between the layers or regions of these materials. In general, the molecular beam epitaxy, chemical vapor deposition, or pulsed laser deposition techniques are required to fabricate the heterostructures. These techniques enable to precisely control the deposition thickness and create a sharp lattice-matched abrupt interface between the layers of two different materials in the heterostructures. Heterostructures have found use in a variety of specialized applications such as lasers, junction, and field-effect transistors. The structural quality of heterostructures with the recent advancement in the deposition techniques enables to fabricate the artificial multifunctional materials which take the oxide electronics to a new level. The precisely controlled interfaces between two materials can give rise to novel physical phenomena and functionalities not exhibited by either of the constituent materials alone. As discussed in Chapter 1, the huge number of different types of perovskite structures and at the same time the tunability of cation and anion give rise to a wide variety of physical and biochemical properties (Assirey, 2019). The perovskite heterostructures are the potential materials for the applications of more exotic functionalities like magnetodielectric, magnetoelectric, colossal magnetoresistance and high-temperature superconductivity. A recent study shows that it is also possible to tune and enhanced Rashba spin-orbit coupling in perovskite heterostructures (Suraj et al., 2020).

In this study, the oxide and oxyhalide based perovskite materials have been considered to construct heterostructures and try to understand and manipulate spin, charge, and orbital order. In metal-oxide and oxyhalide based perovskites, the covalent interactions between the metal center and its oxide/halide ligand are at the heart of the trade-off between charge, spin, and orbital degrees of freedom, leading to interesting emergent physical properties, such as high-spin (HS) to intermediate/low-spin (IS/LS) state transition, metal-insulator transition, and magnetoresistance phenomenon, to name a few (Moritomo et al., 2000; Briceno et al., 1995). The recently synthesized perovskite layered structure of strontium cobalt oxyfluoride Sr_2CoO_3F (SCOF) represents an interesting coordination framework, wherein the coordination of the metal Co atom can be switched from octahedral to square pyramidal shape by applying pressure as external stimulation. A pressure-driven Spin Crossover (SCO) has been observed in layered SCOF. Tsujimoto *et al.* showed that the spin state of the Co^{3+} ion switches from HS to LS state with an applied pressure of 12 GPa. Shrinking of the Co–F bond length is the main mechanism behind the spin state switching of the Co atom with applied pressure, in which the coordination of the Co atom changes from square pyramidal (HS state) to octahedral (LS state), yet without structural phase transition of SCOF (Tsujimoto et al., 2016). Ou *et al.* showed that the spin state transition is still possible at a relatively low applied pressure (Ou et al., 2016a). Their first-principle calculations showed that the spin state switches from HS to IS state with an applied pressure $\sim$ 6 GPa. They also showed that the relative position of the fluorine atom plays a crucial role in determining the spin state of the Co atom. A different, so far unexplored route to perturb the local structure of SCOF and switch its spin state could be to place the material in a charged environment.

With this in view, the magnetic properties of a SCOF layer have been studied under the influence of induced polarization, created in a multiferroic heterostructure that consists of SCOF between two ferroelectric $BaTiO_3$ (BTO) perovskite layers. The key idea is to design seamlessly matching perovskite heterostructures and to use the internal polarization of BTO to drive the SCO in SCOF. First-principle calculations have been used to investigate the magnetic properties of the designed heterostructures. This work shows that the spin state of the Co^{3+} ion can be efficiently controlled by altering the direction of BTO polarization. Computing the ME coupling strength of the BTO-SCOF-BTO multiferroic heterostructure exhibits a giant ME coupling coefficient that is larger than current record values.

3.2 Computational Details

To investigate the magnetic properties of BTO-SCOF-BTO heterostructures, the density functional theory (DFT) calculations have been employed using the Vienna Ab-initio Simulation Package (VASP) (Kresse and Furthmüller, 1996). The Generalized Gradient Approximation (GGA) in the Perdew-Burke-Ernzerhof (PBE) parametrization was used for the exchange-correlation functional (Perdew et al., 1996). The DFT+U technique has been implemented to capture the strong electron-electron correlation, which exists in the partially filled 3d shell and is missing in the conventional GGA (Dudarev et al., 1998). This technique was proven to be an accurate technique to achieve the precise spin state of molecules and low-dimensional magnetic systems (Sarkar et al., 2011; Tarafder et al., 2012; Ou et al., 2016b). The value of on-site Coulomb and exchange parameters U and J were chosen to be 5.0 and 1.0 eV, respectively, for the Co atom. The electron-ionic-core interaction on the valence electrons was represented by projector-augmented-wave (PAW) potentials (Blöchl, 1994). A plane-wave cutoff energy of 400 eV was used in all the simulations for the heterostructures. The reciprocal space was sampled according to the Monkhorst-Pack scheme, and the convergence criterion was set to 10^{-5} eV for the self-consistent electronic energy minimization. Full structural optimization of all bulk structures was carried out using a $4 \times 4 \times 3$ k-point mesh until all residual inter-atomic forces were reduced to less than 0.01 eV/Å. Calculations of the polarized electrode's effect on the SCOF layer were done by minimizing the total energy of the whole system using a $11 \times 11 \times 1$ k-point mesh until all residual inter-atomic forces reduced to less than 0.01 eV/Å.

3.3 Results and Discussions

3.3.1 Heterostructure geometries

The BTO-SCOF-BTO heterostructures have been constructed in two steps. In the first step, the geometry of bulk SCOF was optimized, and its optimized crystal structure is shown in Figure 3.1. The calculated ground state of SCOF is a tetragonal structure with lattice parameters $a = b = 3.92$ Å and $c = 13.12$ Å which are close to the reported experimental values ($a = b = 3.83$ Å and $c = 13.21$ Å) (Tsujimoto et al., 2016). The initial lattice parameters and coordinates of the atoms of cubic and tetragonal BTO were obtained from previously reported studies (Wang et al., 2010; Megaw, 1962). Subsequently, full structural optimization of all bulk structures was carried out.

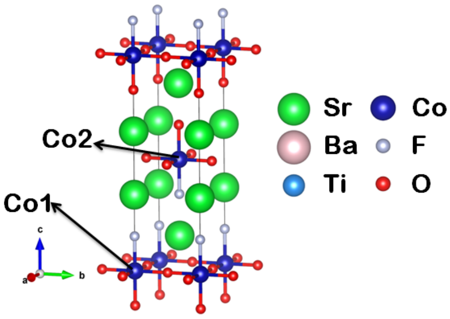

Figure 3.1 Optimized structure of bulk unit cell of SCOF.

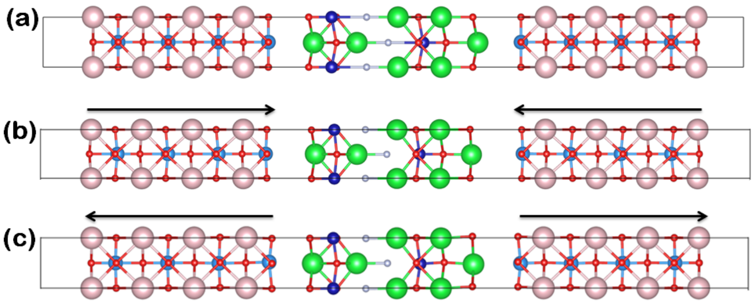

Figure 3.2 Optimized structures three types of BTO-SCOF-BTO multilayer configurations stacked along [001] direction. **(a)** Nonpolar system (NP), where the BTO composition is pseudo-cubic with no polarization, **(b)** polar system (P1), the polarization direction of BTO is toward SCOF, and **(c)** polar system (P2) where the polarization is away from SCOF. Arrows in **(b)** and **(c)** indicate the polarization orientation.

In the second step, the modeled three different BTO-SCOF-BTO multilayer heterostructures stacked along the [001] direction by using the optimized SCOF and BTO structures. The BTO slab was prepared using a $1\times1\times4$ supercell (8 monolayers) of the optimized bulk BTO unit cell. The polarization direction of tetragonal BTO was determined from the relative displacement of ions in the optimized structure. The cubic and tetragonal structure of BTO were used in the nonpolar (NP) and polar states, respectively. The direction of BTO polarization is towards and away from the SCOF in P1 and P2 configurations, as shown in Figures 3.2(b) and 3.2(c), respectively. The structurally stable SrO - TiO_2 interface was chosen in all three heterostructures with the optimized inter-layer distance (Hotta et al., 2007; Shin et al., 2017). A vacuum layer of 8 Å was used in all multilayers unit cells, with a BaO surface termination. The atomic positions of all atoms in the BTO layers on both sides of the heterostructure were kept fixed during the simulation to provide the effect of a charged environment due to a polarized electrode.

3.3.2 Magnetoelectric Coupling Coefficient (α_s)

Here, an investigation of the magnetic properties of BTO-SCOF-BTO was carried out. To start with, the magnetic moments on Co atoms of bulk SCOF was calculated in its optimized geometry. The unit cell of SCOF consists of two Co atoms, both prefer to be in the HS configuration with a magnetic moment 3 μ_B in the ground state structure. However, in BTO-SCOF-BTO heterostructures with different orientations of the BTO polarization, the local environment of the Co atoms has significantly changed, which leads to a change in the spin state of the Co atoms. The theoretically obtained magnetic moment of the two Co atoms in the bulk SCOF structure and the heterostructures with NP, P1, and P2 configurations are tabulated in Table 3.1.

In the bulk phase of SCOF, the high spin of a Co atom can be realized from the electronic configuration of the Co^{3+} ion, where one of the t_{2g} orbitals is completely filled, and the other two t_{2g} along with e_g orbitals are partially filled. The computed total magnetic moment on each Co atom is 3.1 μ_B. Nominally, a Co^{3+} ion would have a d^6 configuration where the magnetic moment in HS state would be expected to be

Table 3.1 *Ab initio* calculated magnetic moments (in μ_B) on the Co atoms in bulk SCOF, and in the NP, P1, and P2 configurations of the heterostructures.

	SCOF	**NP**	**P1**	**P2**
Co1	3.101	3.025	3.068	2.945
Co2	3.101	3.059	-0.051	3.010

4.0 μ_B. Here, however, the calculated moment is reduced due to a strong covalent interaction with the nearest neighbor O and F atoms. A significant charge transfer to the Co atom results from this, which makes the Co-*d* occupancy closer to 7 electrons in each considered configuration. The calculation shows that the magnetic moment of the Co atoms in the NP configuration is not altered, both Co1 and Co2 magnetic moments are in the HS state as for bulk SCOF. However, the total magnetic moment of the unit cell changes for the different polar configurations, i.e. P1 and P2 configurations. The significant change is observed in the P1 alignment for the central Co atom, which is farthest from the SCOF-BTO interface, i.e. Co2 in Figure 3.1.

In the P1 configuration, the magnetic moment on Co2 decreased from 3.059 μ_B to -0.051 μ_B, which demonstrates that the Co2 atom spin has switched from HS ($S = 2$) to LS ($S = 0$) state. Interestingly, in the P2 configuration, the Co2 atom again switched its spin state from LS to HS (3.010 μ_B). Such a large change in the magnetic behavior due to the change of the orientation of the electric polarization leads to a strong ME coupling in the SCOF. The surface ME-coupling coefficient (α_s) has been estimated by using

$$\mu_0 \Delta M = \alpha_s \mathscr{E} \tag{3.1}$$

where μ_0 is the vacuum permeability, ΔM is the change in magnetic flux, and $\mathscr{E}$ is the applied electric field. ΔM was estimated by considering the magnetic moment difference between the P1 and P2 states per unit surface area, i.e., 2.938 μ_B/a^2 (a is the in-plane lattice constant of the P1 and P2 heterostructures, which is the same as an optimized tetragonal BTO lattice constant, i.e. $a = b = 3.9767$ Å, $c/a = 1.0383$). Considering the coercive field of BTO ($\mathscr{E}_c$) of 100 kV/cm, the obtained ME coefficient $\alpha_s \approx 21.65 \times 10^{-10}$ Gcm^2/V (Duan et al., 2008).

It is interesting to compare the obtained result with previously reported α_s values for different systems. Duan *et al.* showed that in Fe/BTO bilayers the magnetic properties depend, too, on the orientation of the BTO ferroelectric polarization and estimated $\alpha_s = 0.01 \times 10^{-10}$ Gcm^2/V (Duan et al., 2006). Similar values were estimated for ultrathin Co and Ni film on a BTO surface and BFO/CoFe$_2$O$_4$ interfaces (Duan et al., 2008; Zavaliche et al., 2005). A significant increase in the ME-coupling constant values were reported for SrTiO$_3$/SrRuO$_3$ (2×10^{-10} Gcm^2/V) (Rondinelli et al., 2008), MnFe$_3$N/BTO (4×10^{-10} Gcm^2/V), Mn$_2$/TiO$_2$ (1.2×10^{-10} Gcm^2/V) (Lu et al., 2015), Co/PbZr$_{0.2}$Ti$_{0.8}$O$_3$ (2×10^{-10} Gcm^2/V) (VlaŠín et al., 2016), Fe$_3$O$_4$/BTO (0.7×10^{-10} Gcm^2/V) (Niranjan et al., 2008) and SrRuO$_3$/BTO (2.3×10^{-10} Gcm^2/V) (Niranjan et al., 2009). The largest value $\alpha_s = 20 \times 10^{-10}$ Gcm^2/V) was reported for a FeO/BTO interface, when a single layer FeO was considered on a BTO surface (Radaelli et al., 2014). The estimated value of α_s for the SOCF/BTO interface exceeds previously reported values, in most cases, by a factor of 10. In comparison to the α_s estimation of FeO/BTO interface (Radaelli et al., 2014), it was found there that the direction of the Fe moment in the FeO layer switches its direction, whereas here in the SCOF layer the central Co switches between HS and LS state configurations.

3.3.3 Electronic Structure

The electronic structure of the system has been studied carefully to understand the spin state switching mechanisms. Thereto, the hybrid functional method was used to obtain an accurate bandgap and relative positions of bands. A 20% Hartree-Fock exchange was used on top of GGA. The thus-calculated bandgap for SCOF in its bulk phase is 2.42 eV. Spin-resolved and atom-projected density of states (DOS) of SCOF in its bulk phase as well as in BTO-SCOF-BTO heterostructures is shown in Figure 3.3.

In all four cases, both the valence band maxima and the conduction band minima are composed of Co $3d$ and O $2p$ states. Note that the bound charge created at the interface due to the polarized BTO may have a significant effect on the local structure of SCOF, especially the anion's position can be expected to be changed due to charge accumulations. The calculated bond lengths and bond angles of the Co2 octahedron in

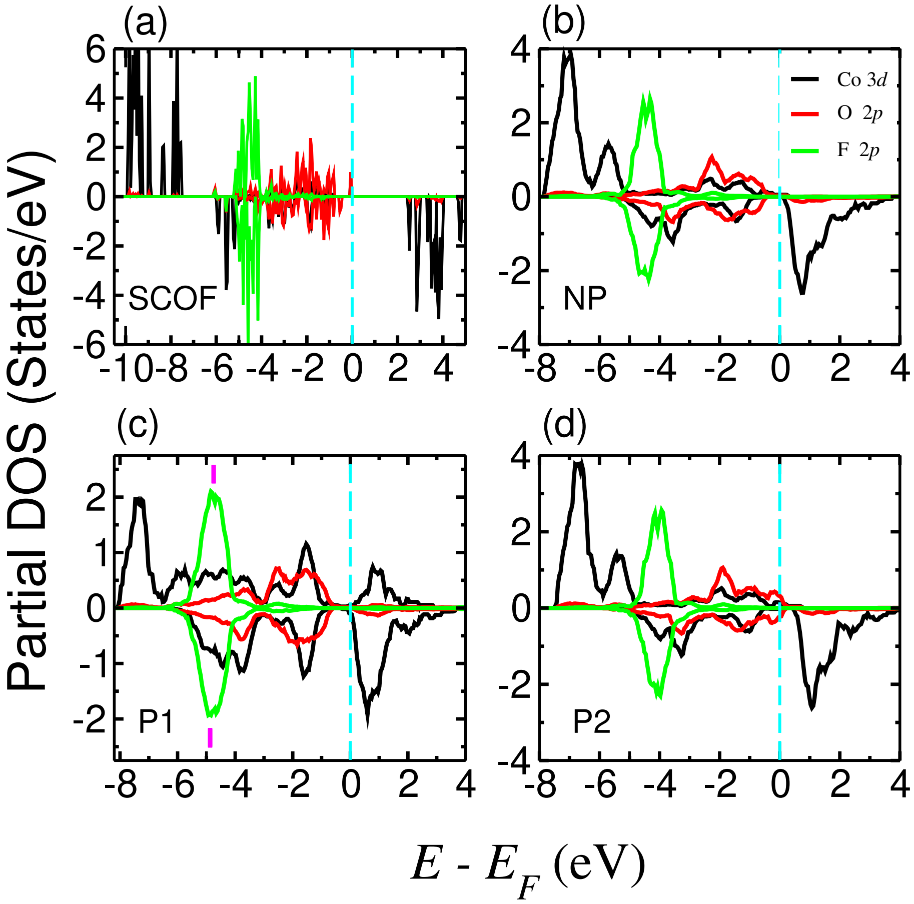

Figure 3.3 Atom projected DOS of Co (black), O (red), and F (green lines) in **(a)** bulk SCOF, **(b)** NP, **(c)** P1, and **(d)** P2 configurations. The solid vertical magenta bars indicate the Co–ligand hybridization which causes the crystal-field splitting in the P1 configuration. Spin-up and spin-down partial DOS are shown by positive and negative values, respectively. The Fermi energy level (E_F) is set at $E = 0$.

the P1 and P2 configurations are shown in Figure 3.4.

In the P1 configuration, the polarization is pointing toward the SCOF, therefore there are positive bound charges at the interface. It has been observed that the Co2–F bond length was reduced by ∼0.2 Å in this configuration compared to the P2. Therefore an increase of covalency in the Co–F bond is expected. Also, positive bound charges at the interface affect the electrons in outer orbitals (d_{xz} and d_{yz} states) which leads to a charge redistribution in the d-orbitals of the Co2 atom. To understand the effect, further calculated the orbital projected DOS of Co2 3d electrons in bulk SCOF and NP, P1, and P2 heterostructures, shown in Figure 3.5.

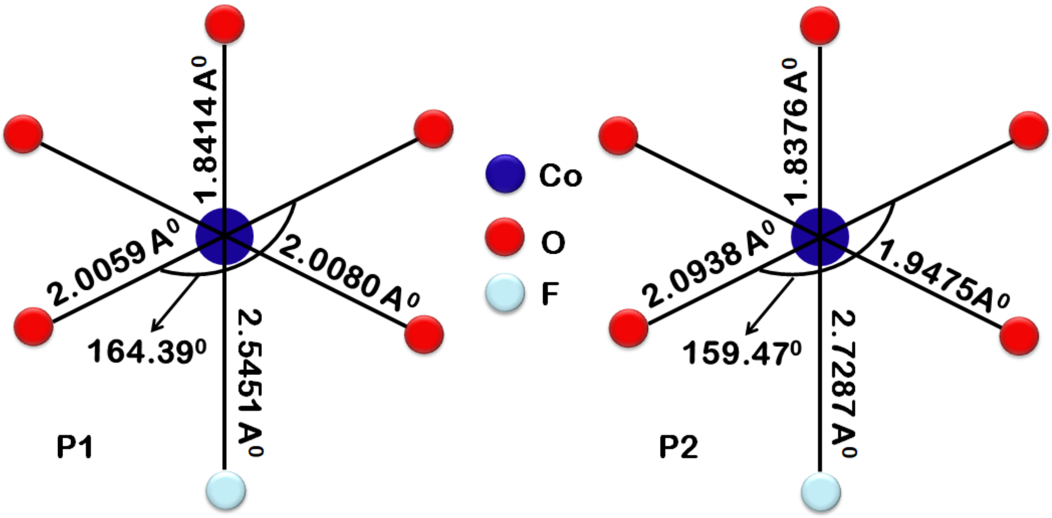

Figure 3.4 Calculated bond angle and bond lengths of the Co2 octahedron in the P1 and P2 configurations. The atoms are labelled by the corresponding colors.

It has been found that three of the t_{2g} orbitals are fully occupied, and the e_g orbitals are completely empty in the P1 configuration, whereas they are partially filled in the bulk configuration. This result can be explained by considering the strong crystal-field effect due to induced polarization and internal strain in SCOF. The $2p$ orbital of the F ligand hybridized more with the Co $3d$ orbitals due to the reduction of Co2–F bond length. Subsequently, the energy level of the Co d_{z^2} orbital is increased (see Figure 3.5(c)). Also, it has been observed that the O–Co2–O bond angle increases, which allows the $d_{x^2-y^2}$ orbital to come closer to the in-plane ligand orbitals and raise its energy level while d_{xy} is away from them. In addition, positive bound charges at the interface lower the energy level of the d_{xz} and d_{yz} orbitals. Hence, the structural distortion in Co2 octahedron enhances the crystal-field splitting where the e_g orbitals of the Co2 atom that were partially occupied in the bulk phase are now formally unoccupied. Empty $d_{x^2-y^2}$ and d_{z^2} orbitals are recognizable in Figure 3.5(c). Therefore the electron configuration of the trivalent Co2 atom is approximately $t_{2g}^{(6)} e_g^{(0)}$ and has the LS state.

On the other hand, in the P2 configuration, the polarization is directed away from SCOF. Therefore, the negative bound charge accumulated at the interface that does not affect much on the local environment of the Co2. As a result, the change in the crystal field is not significant, and the crystal field is very similar to the case of NP

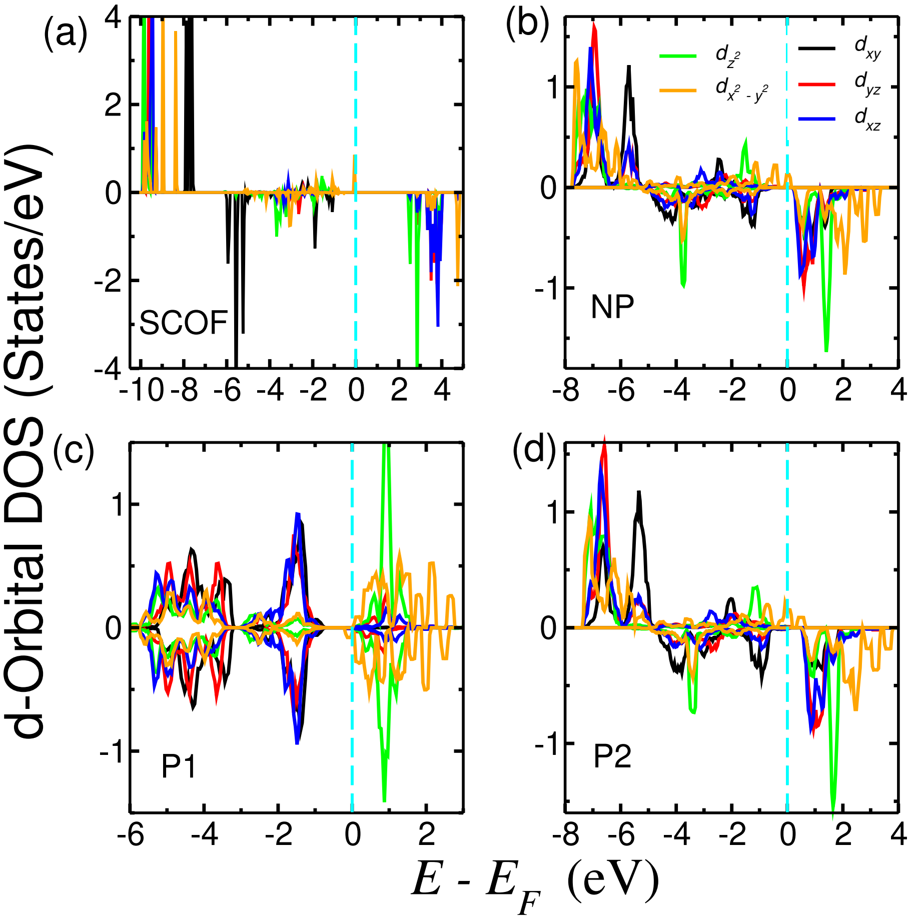

Figure 3.5 The $3d$-orbital projected DOS of the Co2 atom in **(a)** bulk SCOF, **(b)** NP, **(c)** P1, and **(d)** P2 configurations. The $3d$ orbitals are depicted by the different colors and spin-up and spin-down DOS are shown as positive and negative values, respectively.

configuration. Both e_g orbitals of the Co2 atom are now partially field. All d-orbitals in this case are completely filled with majority spin electrons. The minority spin electrons are present only in the d_{xy} orbital (see Figure 3.5(d)). Hence, the electron configuration of Co2 in the P2 heterostructure is $\sim t_{2g}^{(4)} e_g^{(2)}$, and exhibits the HS state. The non-hybridization of the Co2 ion with F ligand orbitals is the witness for the HS state of the Co2 atom in P2 configuration shown in Figure 3.5(d). The relative occupation of majority and minority spin electrons in the $3d$-orbitals in the different spin state configurations are schematically shown in Figure 3.6. A similar trend is observed in bulk SCOF and the NP configuration.

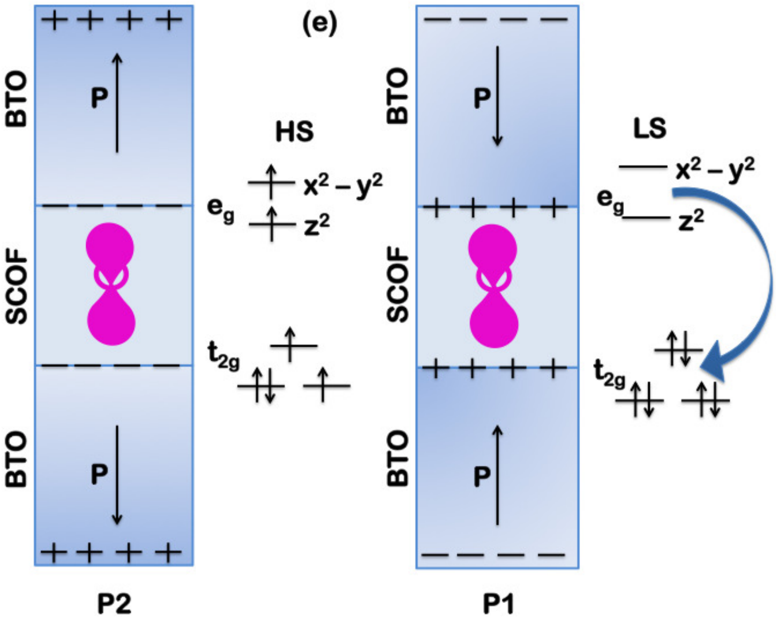

Figure 3.6 Schematic diagram of electron occupancy in the high-spin and low-spin state configuration of Co2.

3.4 Conclusion

To conclude, polarization induced spin state switching and giant magnetoelectric effect has been demonstrated in structurally stable perovskite BTO-SCOF-BTO heterostructures. The calculations show that the magnetic properties of the Co2 atom in a SCOF layer can be tuned by altering the direction of the internal polarization of BTO. Different bound charges at the interface created due to the polar BTO slab influence significantly the energy levels of Co 3*d* orbitals. As a result, the different polarization states in BTO induce a spin state transition of the central Co atom from HS to LS and LS to HS state. The spin state switching of the system due to a polarization change gives rise to a giant ME-coupling constant. The investigation in this study provides a pathway for exploring new polarization-induced spin switching in oxyfluoride SCO materials and subsequently to achieve record magnetoelectric couplings. In the next chapter, the investigation of SCO phenomena in a Hofmann-type like 2D coordination polymer, namely $\mathrm{Fe\{OS(CH_3)_2\}_2\{Ag(CN)_2\}_2}$ complex, by applying external pressure shall be discussed. Further, the pressure-driven spin state switching of the Fe atom in the complex has been observed to be associated with structural transformation.

Chapter 4

Pressure-Driven Structural and Spin State Transition in a Hofmann Clathrate Coordination Polymer

Hofmann-type like organometallic frameworks are well known for their porous crystal structure, exhibit interesting electronic, optical and magnetic properties, therefore could be promising materials for various technological applications. In this chapter, the spin state transition in a newly synthesized Hofmann clathrate coordination polymer, namely $Fe\{OS(CH_3)_2\}_2\{Ag(CN)_2\}_2$ complex by applying hydrostatic pressure as an external perturbation, shall be discussed. This study reveals that under a relatively low isotropic hydrostatic pressure, the complex exhibits a reversible spin switching, whereas it undergoes a structural phase transition when the pressure is anisotropic. The spin state of the Fe atom in the complex transforms from high spin to intermediate spin state under anisotropic compression of the lattice parameters. The coordination polymer complex remains a magnetic semi-conductor after the pressure-driven structural transformation.

4.1 Introduction

Crystalline organometallic hybrid complexes in which metal centers are connected through an organic linker and form porous coordination polymers have gained special research interest (Férey et al., 2005). Due to their enormous porosity and very large internal surface area, they have been extensively studied for the last two decades because of their possible application in gas storage and separation. Besides, the relative easy chemical modification of this class of materials by incorporating guest molecules inside the porous organometallic frameworks has promoted them as interesting functional materials, suitable for many advanced technological applications such as spintronic, catalysis, color chemistry, sensors, drug delivery, biomedical imaging and other medical applications (Zhou et al., 2012; Wang et al., 2018a; Verdaguer and Robert, 2013). Moreover, the extraordinary degree of variability in synthesizing these compounds considering different transition metal ions centers, perturbing the metal-ligand bond length, coordination with different co-ligands etc., provides the excellent knobs to control the spin state of the transition metal and overall magnetic behavior of the systems (Wäckerlin et al., 2012; Demir et al., 2012). It has been reported that even the redoxiation in m-phenylene based di-radicals switches the nature of magnetic coupling (Ali et al., 2013). Among all the metal-organic frameworks, the cyanide-bridged complexes have been studied extensively due to their remarkable magnetic, photomagnetic, electrochemical, and adsorption properties (Sato et al., 1996; Ohba et al., 2009; Niel et al., 2001; Ferlay et al., 1995; Dunbar and Heintz, 1996; Hofmann and Küspert, 1897; Deepa et al., 2009; Torad et al., 2012; Kaye and Long, 2005). In general, the cyanide-bridged bi-metallic coordination polymer complexes (or Hofmann-type like networks) have a molecular structure similar to $[M(L)_2M^{'}(CN)_4]$, where M is the metal atom (for example, Mn^{2+}, Fe^{2+}, Co^{2+}, Ni^{2+}, Cu^{2+}, Zn^{2+}, and Cd^{2+}), $M^{'} = Pd^{2+}$, Pt^{2+}, Ni^{2+} and L = ligand. The ligand could be either unindented or bridged, depending on that it forms 2D or 3D-coordination layers, respectively. Typically, a large space remains in between layers of these complexes that can accommodate guest molecules. In addition to the porosity, a variety of possible conformation of ligands leads to different spin state of metal atoms in the complex. As a result, Hofmann clathrates with suitably chosen ligands could exhibit Spin Crossover (SCO) behavior (Kitazawa et al., 1996; Niel et al., 2001).

A proper understanding of the SCO phenomena in the metal-organic framework demands detailed knowledge of electronic and/or magnetic interactions between transition metal centers and its neighboring ligands. Interestingly, such interaction in the metal-organic framework can be tuned in a controlled way by using an external stimulation. It may often give rise to other very significant cooperative phenomena such as memory effect, first-order structural transition, metal-insulator transition, and long-range magnetic ordering (Boldog et al., 2008; Larionova et al., 2008; Tarafder et al., 2012; Tiana et al., 2014).

Kucheriv *et al.* synthesized a cyanide-bridged coordination polymer (or Hofmann clathrate) complex, $Fe\{OS(CH_3)_2\}_2\{Ag(CN)_2\}_2$ that have a 2D-polymeric structure, and with the information of Fe-N(O) bond lengths, they have reported that the Fe^{2+} atoms in the complex are stabilized at High Spin (HS) state (Kucheriv et al., 2017). Being a porous metal-organic framework, interesting pressure-driven phenomena is expected in this material. However, the detailed electronic structure and magnetic properties of this newly synthesized Hofmann clathrate complex have not been reported so far. In the present study, the electronic structure, magnetic properties, and pressure-induced SCO behavior have been investigated in this newly synthesized compound by using the density functional theory calculations. The SCO has been achieved in the complex by perturbing the system with isotropic hydrostatic pressure. Interestingly, in addition to the usual SCO behavior (reversible switching from HS to IS state), it has been observed that the coordination polymer complex undergoes a structural transition.

4.2 Computational Details

To study the pressure-driven spin state and structural transition in Hofmann clathrate, the density functional theory+U (DFT+U) calculations have been employed using the plane wave based pseudopotential method, as implemented in Vienna Ab-initio Simulation Package (VASP) (Kresse and Furthmüller, 1996). projector-augmented-wave (PAW) potentials were used to represent the electron-ionic-core interaction on the valence electrons (Blöchl, 1994). The Generalized Gradient Approximation (GGA) with the Perdew-Burke-Ernzerhof parameterization was used for the exchange-correlation function (Perdew et al., 1996). The DFT+U technique was used in these calculations to account for the strong electron-electron Coulomb interactions that exist in the open 3d shell of transition metal (Fe) and the missing correlation effect beyond the plain GGA (Dudarev et al., 1998). This approach has given precise spin state results for SCO molecules (Tarafder et al., 2012). The on-site Coulomb (U) and exchange (J) parameters used in the present calculations were chosen to be 5 eV and 1 eV for Fe atom (Tarafder et al., 2012). A 5×3×4 Monkhorst- Pack grid of k-points was used for reciprocal space sampling. The very high energy cutoff 500 eV was considered for the plane wave expansion. The 10^{-5} eV convergence criterion was set for the self-consistent electronic minimization and optimized the geometry until all Hellmann-Feynman forces were smaller than 0.01 eV/Å.

4.3 Results and Discussions

4.3.1 Optimized Crystal structure

To unravel the pressure-driven SCO phenomena in $[Fe\{OS(CH_3)_2\}_2\{Ag(CN)_2\}_2]$, the geometry of the initial crystal structure that has taken from the reported data has been relaxed, in the first step (Kucheriv et al., 2017). The complex has the monoclinic crystal structure ($P2_{1/c}$ space group) with C_{2h}/mm point group symmetry. The basic structural unit cell of the complex consist of a $Fe\text{-}N_4O_2$ block in which the Fe atom is sitting at the center of a distorted octahedron with four N and two O atoms are as corners. Four N atoms in the basal plane are connected with four linear CN^--Ag-CN^- chains, and two axial O atoms are connected to the dimethyl sulfoxide molecules. CN^--Ag-CN^- chains are further connected to the Fe atoms and form a two-dimensional polymeric structure (see Figure 4.1). In the relaxed crystal structure, the Fe atom inside the $Fe\text{-}N_4O_2$ octahedron is in HS state (S=2) and has a magnetic moment 3.781 μ_B.

In the next step, pressure-induced calculations have been performed in the relaxed crystal structure by reducing the volume of the unit cell. The volume of the unit cell has been reduced systematically without distorting the shape (aspect ratios remain constant) to mimic the application of hydrostatic pressure, and each time relaxed the all atomic positions of the unit cell. It has been observed that the magnetic moment of the Fe^{2+} atom abruptly changes from 3.781 μ_B to 1.977 μ_B upon volume reduction. It indicates that the Hofmann clathrate undergoes SCO behavior with the spin state transition of Fe^{2+} atom from HS (3.781 μ_B) to Intermediate Spin (IS) (1.977 μ_B) state by applying an external perturbation. The change in the spin states of TM by perturbing the system

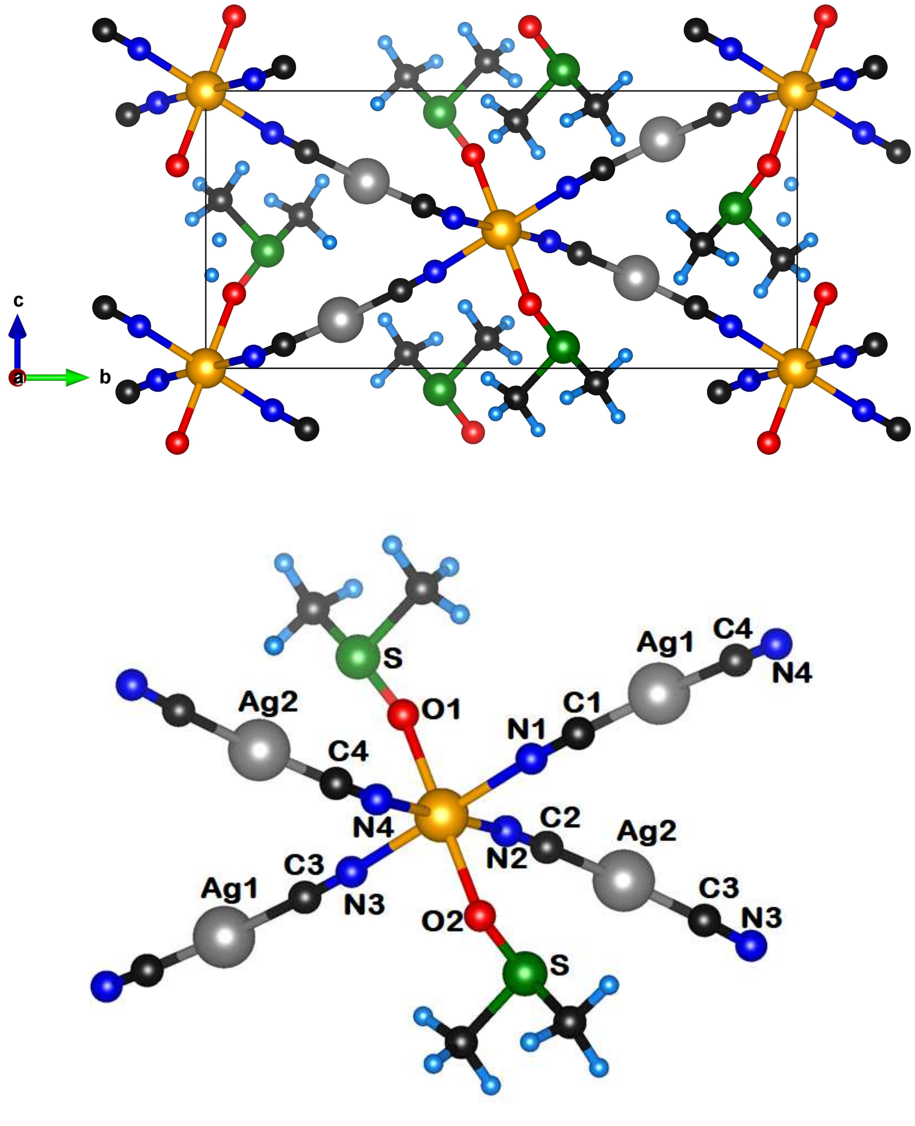
c
a
b
S
Ag1
C4
N4
O1
Ag2
C1
N1
C4
C2
Ag2
N4
N2
C3
Ag1
C3
N3
N3
O2
S

Figure 4.1 The optimized crystal structure of $[Fe\{OS(CH_3)_2\}_2\{Ag(CN)_2\}_2]$ complex. The Fe, N, O, Ag, S, C and H atoms are represented with the orange, blue, red, silver, green, black, and cyan color balls, respectively.

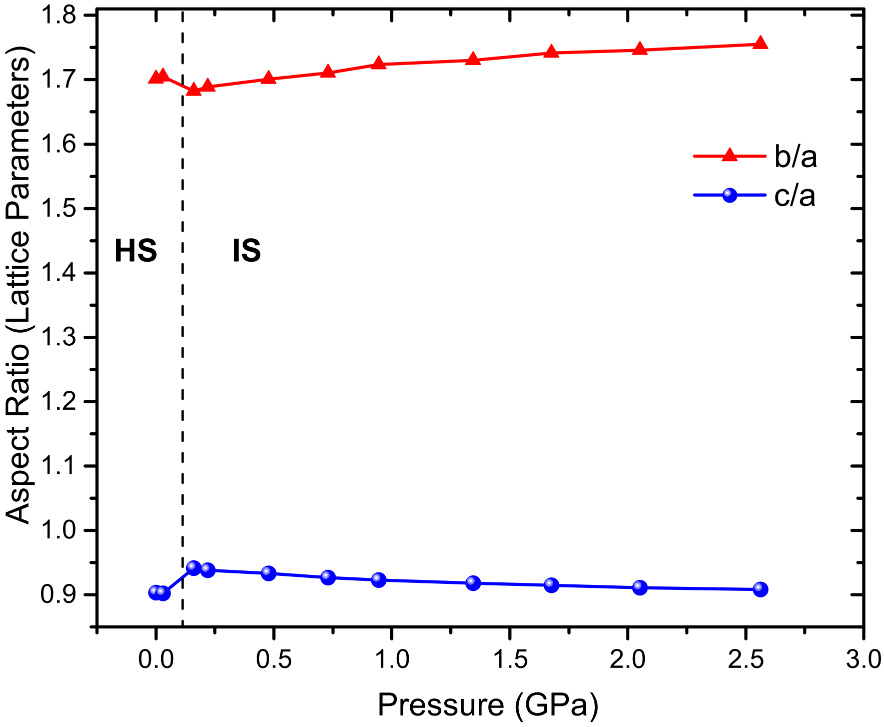

Figure 4.2 Computed variation of the aspect ratio with applied pressure. Red triangle and blue sphere symbols represent the calculated values of the b/a and c/a ratios respectively.

is commonly observed in the Fe^{2+}-based SCO complexes. However, the energy difference between the two different magnetic states in the present complex is found to be remarkably large and about 2.06 eV. One possibility of such a high energy difference is due to a structural transition in the system under pressure. To understand this, the volume-specific total-energy calculations of the complex have been performed for different volumes. In this set of calculations, the atomic positions and the shape of the unit cell are allowed to relax. Interestingly, a sudden change in the aspect ratio of the lattice parameters was observed upon increasing the pressure. The change in aspect ratios with pressure is shown in Figure 4.2. An anisotropic compressibility behavior has been clearly observed during the structural phase transition. A similar set of calculations has also been done considering constant volume as well as the magnetic configuration.

The volume versus total energy of the system in two different magnetic configurations is shown in Figure 4.3. It clearly shows that the different magnetic states of

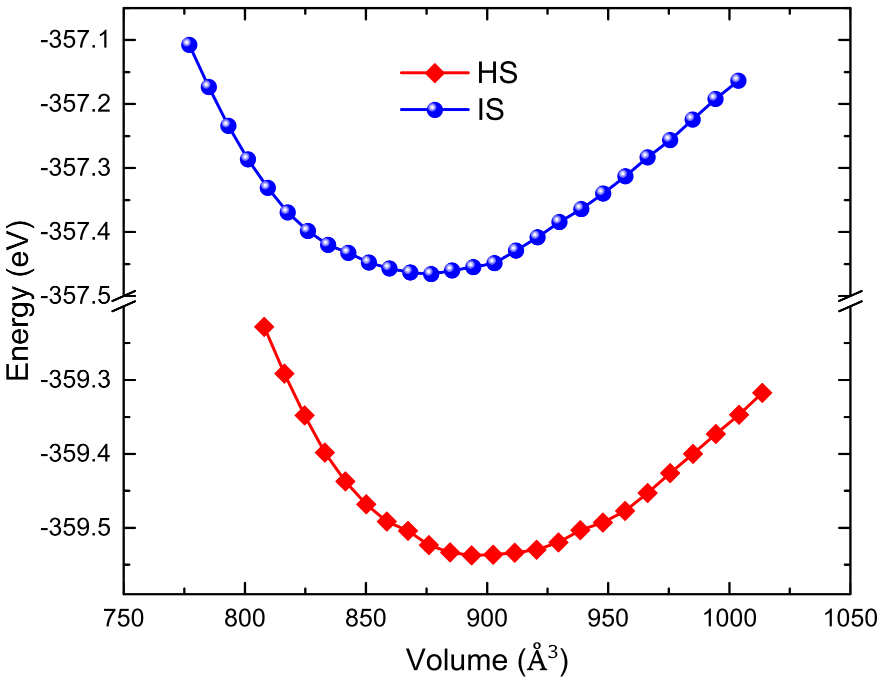

Figure 4.3 The computed total energy of the [Fe{OS(CH_3)$_2$}$_2${Ag(CN)$_2$}$_2$] complex versus variation of volume of the unit-cell volume, showing the energy minima at both the HS and IS states.

the complex have different energy minima, and indicates that the present coordination polymer complex may undergo a structural transition while transiting from HS state to the IS state.

The transition pressure between the two different structures can be obtained from the relative enthalpy difference under different pressure. Thus, the enthalpy difference at different pressures has been calculated and shown in Figure 4.4a. This shows that the critical pressure for the structural transition is $\sim$ 0.09 GPa. An abrupt expansion of the outer-plane lattice (c-axis) and shrinkage of the in-plane lattices (a-, and b-axis) at the transition pressure predicts anisotropic compressibility of the compound. This anisotropic compressibility of the system results in a sudden change in the unit-cell volume. The calculated volume versus pressure data for two different magnetic configurations is shown in Figure 4.4a. The data were fitted to the third-order Birch-Murnaghan isothermal equation of state, given by,

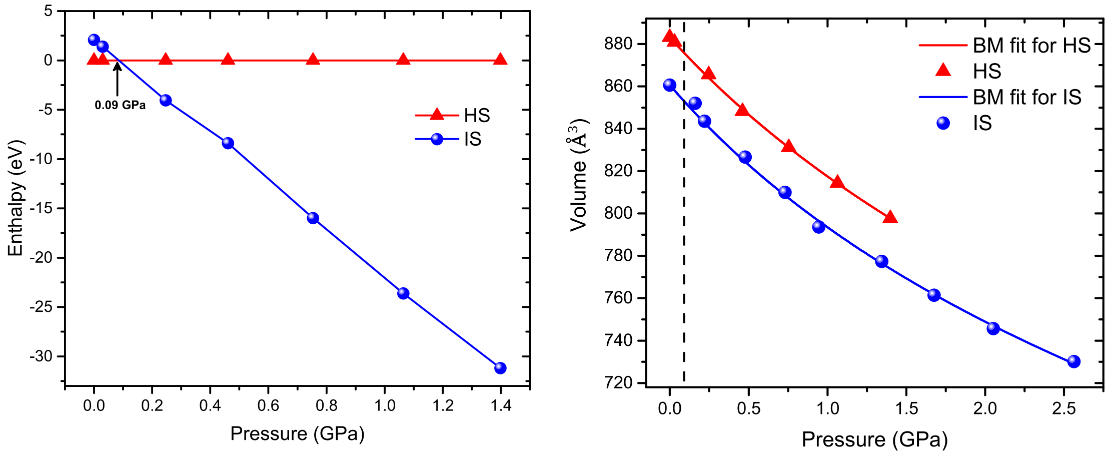

Figure 4.4 Structural phase transition from Monoclinic-I to Monoclinic-II in the unit cell of [Fe{OS(CH$_3$)$_2$}$_2${Ag(CN)$_2$}$_2$] complex. **(a)** static enthalpy difference as a function of pressure for two magnetic configurations HS (red) and IS (blue) of Fe atoms. **(b)** The calculated pressure versus volume of the unit cell at HS (red) and IS (blue) state. The data points are represented with symbols, whereas lines represent the fitted curves obtained from fitting with the Birch–Murnaghan isothermal equation of state.

$$P(V) = \left(\frac{3B_0}{2}\right) \left[\left(\frac{V_0}{V}\right)^{\frac{7}{3}} - \left(\frac{V_0}{V}\right)^{\frac{5}{3}}\right] \left\{1 + \frac{3}{4}(B_0^{'} - 4) \left[\left(\frac{V_0}{V}\right)^{\frac{2}{3}} - 1\right]\right\}$$

where V_0 is the equilibrium volume, the bulk modulus, B_0 is given by $B_0 = -V(\delta P/\delta V)$, and $B_0^{'}$ is the pressure derivative of B_0 evaluated at volume V_0. The bulk modulus has been calculated by fitting the volume versus pressure data to the Birch-Murnaghan equation of state (see Figure 4.4b) and are found to be 10.72±0.28 GPa and 9.9±0.41 GPa for Monoclinic-I and Monoclinic-II respectively, and the calculated pressure derivatives are 4.09±0.45 and 3.72±0.46, respectively. The calculated B_0 is comparable with other reported SCO molecules and also falls in the range of B_0 of other metal-organic frameworks (Mikolasek et al., 2018; Sciortino et al., 2016; Tan and Cheetham, 2011). As illustrated in Figure 4.4b., the transition pressure is marked with a vertical black dashed line; the volume of the unit cell was found to be collapsed by 2.58 % during the structural transition. This confirms the occurrence of pressure-driven structural transition in the Hofmann clathrate complex in addition to the spin state transition. Different amounts of volume collapse were reported in crystalline materials during the phase transition (Xiao et al., 2010; Wang et al., 2016, 2018b; Huang et al., 2017; Solomatova et al., 2016; Bajaj et al., 2018). The percentage of the volume collapse which has been obtained in this study can also be considered as a significantly large value, compared with the reported values of volume collapse during the structural transition (Hunter et al., 2011; Shekar et al., 1996). It is interesting to note that the volume collapse due to the anisotropic compressibility of the lattices and the concomitant spin state transition that is obtained for the present system occurs at a remarkably low transition pressure.

4.3.2 Electronic Structure and Density of States

The origin of the SCO behavior, i.e. the pressure-driven change in the magnetic structure of the Hofmann clathrate has been analyzed through careful electronic structure calculations. The atom projected and orbital density of states (DOS) provide a clear insight into the spin state transition of the Fe atom in the system.

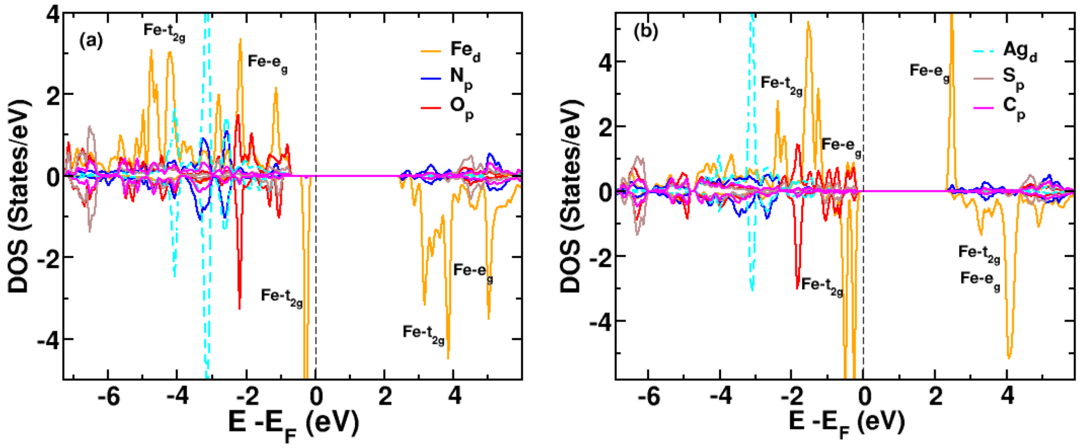

Figure 4.5 Atom-projected partial DOS of the $[\mathrm{Fe}\{\mathrm{OS}(\mathrm{CH}_3)_2\}_2\{\mathrm{Ag}(\mathrm{CN})_2\}_2]$ complex, for **(a)** the Monoclinic-I structure with HS state magnetic configuration, and **(b)** the Monoclinic-II structure with IS state magnetic configuration. The positive and negative values of the DOS corresponding to the spin-up spin-down channel, respectively. The Fermi energy (E_F) is set at zero of the energy.

The spin-polarized atom projected DOS of the HS state (Monoclinic-I) and IS state (Monoclinic-II) configurations of the complex are shown in Figure 4.5a and 4.5b, respectively. The states near the Fermi level are dominated by Fe_{3d} orbitals. The majority and minority spin DOS of the Fe_{3d} states are found to be asymmetric due to the strong spin-polarization. In octahedral coordination, the Fe_{3d} states split into t_{2g} and e_g groups. In the Monoclinic-I phase, both the t_{2g} and e_g group orbitals are found to be completely

Table 4.1 Fe-ligand bond-lengths (in Å) computed for the optimized HS and IS states of the [Fe$\{OS(CH_3)_2\}_2\{Ag(CN)_2\}_2$] clathrate complex, as well as Ag chain bond lengths. The N1 and N4 atoms are also connected to N–C–Ag–C–N chains, while the O1 and O2 atoms are connected to the dimethyl sulphoxide (see Figure 4.1).

	HS state	**IS state**
(a) Fe-N_4O_2 Octahedron		
Fe-N1, Fe-N3	2.1759	1.9602
Fe-N2, Fe-N4	2.1945	2.0514
Fe-O1, Fe-O2	2.1437	2.2718
Average Fe-ligand bond-length	2.1714	2.0944
(b) {N-C-Ag-C-N} Chain		
N1(N2) - C1(C2)	1.1714	1.1706
C1 - Ag1	2.0531	2.0578
Ag1 - C4	2.0523	2.0576
C4(C3) - N4(N3)	1.1714	1.1706
C2 - Ag2	2.0523	2.0576
Ag2 - C3	2.0531	2.0578

occupied in the majority-spin channel only, whereas in the minority-spin channel only one t_{2g} orbital is occupied with spin-down electron and the rest of the t_{2g} along with all e_g orbitals are empty. Thus the spin state of the Fe atom in the Monoclinic-I structure is turned out to be HS state $(S = 2)$ with the computed magnetic moment 3.781 μ_B per Fe atom. In the Monoclinic-II phase, one e_g and three t_{2g} orbitals are filled with majority-spin electrons, whereas the two minority-spin electrons occupy two t_{2g} orbitals, the e_g minority-spin orbitals are completely empty. As a result, the spin state of Fe atom in Monoclinic-II structure becomes the less commonly observed IS state $(S = 1)$, and concurrently the computed magnetic moment of the Fe atom changes from 3.781 to 1.977 μ_B. The calculated band gap of the Hofmann clathrate in the Monoclinic-I (at HS state) and Monoclinic-II (at IS state) is 2.306 and 2.234 eV, respectively. Hence, it is interesting to note that the Hofmann clathrate coordination polymer is predicted to exhibit a semiconductor to semiconductor transition of the system during the structural transition, thus unlike metal-insulator or metal-semimetal transition (Cheng et al., 2015; Delmonte et al., 2018).

To understand the spin state transition of the system, the octahedral coordination of the Fe atom has been investigated carefully. The calculated bond lengths in the Fe-N_4O_2 octahedral coordination and the linear chain of the CN-Ag-CN in the HS and IS state are tabulated in Table 4.1. The average Fe-ligand bond length in the HS state (Monoclinic-I) is 2.17 Å, which changes substantially to 2.09 Å in the case of IS state configuration. Although the Fe-O bond lengths increased from HS (2.14 Å) to IS (2.27 Å) state due to an elongation of the c-axis during the structural transition, the Fe-N bond lengths along CN-Ag-CN chain reduces significantly. As a result, the average Fe-ligand bond lengths reduce from 2.171 Å (in HS) to 2.094 Å (in IS) during the spin state transition. Hence, the shorter Fe-N bond lengths are sufficient to induce the ligand field effect in the 3d-orbitals of Fe atom that could trigger its spin state to change from HS to IS state. This can be confirmed from the Fe-3d orbital DOS shown in Figure 4.6.

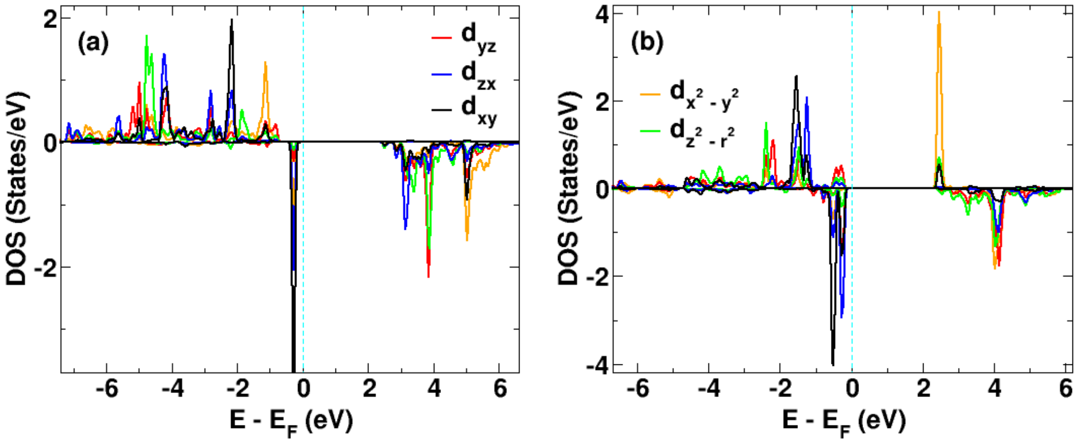

Figure 4.6 The 3d-orbital projected DOS of Fe atom in the $[Fe\{OS(CH_3)_2\}_2\{Ag(CN)_2\}_2]$ complex, for **(a)** the system is in the Monoclinic-I phase, and Fe atom is in HS state, and **(b)** system is in Monoclinic-II phase, and the Fe atom is in the IS state configuration. The positive and negative values of DOS corresponding to the spin-majority spin-minority channel, respectively. The Fermi energy (E_F) is set at zero of the energy.

The comparison of the orbital projected DOS in HS and IS of Fe atom clearly shows the ligand field, which further splits the e_g orbital. As a result one of the e_g orbital ($d_{x^2-y^2}$) in the majority-spin channel becomes higher in energy and move to the conduction band, whereas the electron moves to occupy one of the t_{2g} orbital (d_{zx})of the minority spin channel.

4.4 Conclusions

To conclude, the pressure-driven spin state transition associated with the structural transition in a newly synthesized organometallic framework, namely $Fe\{OS(CH_3)_2\}_2$ $\{Ag(CN)_2\}_2$, have been investigated using DFT+U calculations. The calculated spin-polarized DOS reveal significant changes in the electronic structures, but nonetheless, both monoclinic structures are predicted to be semi-conductors. However, in this study, only the hydrostatic pressure has been considered as external stimuli and estimated the transition pressure for spin state transition and structural transformation in the Hofmann clathrate at 0 K. In the experimental point of view, note that the required pressure for structural transformation is expected to be smaller than the reported value due to high temperature as well as the existence of shear and stress components in the experimental material (or sample) (Xia et al., 1991; Zhang et al., 2010; Shi and Falk, 2007). Moreover, the estimated transition pressure for the spin state transition and structural transformation is ≈ 0.09 GPa, which could be feasible for the experimental laboratory set-up. In addition to this, this work suggests further research to trigger the spin state switching by applying temperature, light irradiation, electric and magnetic field as an external stimulus to explore the new aspects of this compound, as observed in other organometallic frameworks (Khusniyarov, 2016). In the next chapter, the SCO phenomena in a single molecular system shall be discussed. There, the detail description of the structural, electronic, and magnetic properties of Ni(II)-quinonoid complex upon adsorption on a magnetic Co(001) substrate along with the substrate-induced SCO phenomena shall be provided.

Chapter 5

Interfacial Spin Manipulation of Nickel-Quinonoid Complex Adsorbed on Co(001) Substrate

In this chapter, the structural, electronic, and magnetic properties of a recently synthesized Ni(II)-quinonoid (NiQ) complex absorbed on the magnetic Co(001) substrate shall be discussed. The NiQ molecule undergoes a spin state switching from low spin ($S = 0$) state in the gas phase to high spin ($S \approx 1$) state when the molecule adsorbed on the Co(001) surface. A strong covalent interaction of the quinonoid rings and surface atoms leads to an increase of the Ni–O(N) bond lengths in the chemisorbed molecule that supports the spin state switching. The molecule ferromagnetically coupled to the substrate, where the exchange mechanism between the Co surface and metal center (Ni atom) of the molecule is an indirect exchange interaction via the quinonoid ligands that stabilizes the spin moment of the molecule in ferromagnetic alignment with the Co surface magnetization.

5.1 Introduction

The evident increase in the relevance of molecular spintronics in the past two decades is because of its promise for advanced multifunctional spin devices. (Bogani and Wernsdorfer, 2008; Moodera et al., 2014). Especially spin-bearing molecules with one or more transition metal (TM) ions having a partially filled d shell with d^4 to d^7 configurations have drawn particular attention as for many such complexes the spin properties can be manipulated externally. It has been shown that an external perturbation such as pressure, temperature, light irradiation, an electric or magnetic field can aid in reversible switching between different spin states in Spin Crossover (SCO) complexes (Gütlich et al., 2004; Hao et al., 2012). Many magnetic molecules have been synthesized and intensively investigated both theoretically and experimentally in the past years (Coronado et al., 2003; Gatteschi et al., 2006; Benelli and Gatteschi, 2015; Banerjee et al., 2017). The progress made recently in the application of SCO complexes in functional devices has been reviewed lately (Kumar and Ruben, 2017; Molnár et al., 2018). The understanding of the underlying electronic and magnetic interactions on the single-molecule level is, however, still sparse. Intensive research is being carried out in spin detection, manipulation, and transport in organic materials that form an integral part of any advanced spin device.

Growing molecules on magnetic as well as inert surfaces with atomic precision are one of the approaches to develop such devices. Immobilized magnetic metal-organic molecules with tailorable magnetic properties can be deposited on solid substrates to construct building blocks for molecular spintronic devices (Auwärter et al., 2015; Gottfried, 2015). In this process, the magnetic stability of the molecules at higher temperatures can be achieved which is attributed to the substrate-induced magnetic exchange coupling and/or substrate-induced magnetic anisotropy (Scheybal et al., 2005; Gambardella et al., 2009; Miller and Gatteschi, 2011). New magnetochemical properties arise due to the molecule–substrate interaction that comes as an added advantage over traditional spintronics (Raman et al., 2013; Djeghloul et al., 2013; Steil et al., 2013; Bairagi et al., 2015; Barraud et al., 2015). It has been observed that magnetic molecules reacting on a metallic surface may lose their magnetic properties by coupling with the electrodes, even if they remain intact (Sanvito, 2011). Thus, a proper understanding of molecule–substrate interactions is essential before being implemented in its technological application in data storage, sensor, quantum computing, or other single molecular spintronic device applications (Rocha et al., 2005).

In general, non-planar molecules would bind weakly to a metal surface due to steric hindrance, and therefore, planar molecules become suitable candidates in the design of molecular devices involving their deposition metal surfaces as they would strongly bind or self-assemble on the same. Several theoretical, as well as experimental observations, have been reported on the magnetic interactions of transition-metal porphyrins (TM-P) (Scheybal et al., 2005; Wende et al., 2007), transition-metal phthalocyanine (TM-Pc) (Gottfried, 2015; Lodi Rizzini et al., 2012; Girovsky et al., 2017), and cyclohexane-based organic molecules (Gruber and Berndt, 2016) with metal substrates. It has been observed that planar TM-P and TM-Pc molecules are very promising as they show stable magnetic behavior due to exchange coupling to the magnetic substrate. Moreover, their magnetic properties can be tailored by engineering the spin states of the metal center using on-surface magnetochemistry, i.e., chemical perturbation by coordination in the free ligand position or through interlayer modified exchange interaction (Flechtner et al., 2007; Bernien et al., 2009; Wäckerlin et al., 2012; Ballav et al., 2013; Hermanns et al., 2013; Herper et al., 2013). Spin state switching is also observed for a planar metal–organic molecule due to stretching the metal-ligand distance (Bhandary et al., 2013), similar to the bond-length induced switching of SCO molecules (Gütlich et al., 2004).

Kar *et al.* designed a methanol-triggered vapochromism and spin-switching in a Ni(II)-quinonoid (NiQ) complex [Ni(HL)$_2$, H$_2$L = 4-methylamino-6-methyliminio-3-oxocyclohexa-1, 4-dien-1-olate], which is a planar molecule. They showed that the addition of methanol (MeOH) to the molecule leads to a magnetochemical reaction, in which the central Ni atom of the molecule changes its coordination from square-planar to octahedral by axial ligation of two MeOH groups at the Ni site, accompanied by a temperature-robust spin transition from $S = 0$ to $S = 1$ (Kar et al., 2017). This observation suggests that the Ni(II)-quinonoid could be a potential candidate material for application in spintronics devices. However, for applications, a detailed understanding of the molecular adsorption mechanism on a metal surface is essential and, in addition, whether magnetic interface interactions are sufficient to trigger the spin-switching becomes a primary question that has to be answered.

The main objective of the present investigation involved the study of the geometric and electronic structure of the multifunctional NiQ molecule when adsorbed on a Co(001) substrate, its emergent magnetic interactions at the spin-interface, and, specifically, whether an on-surface spin state transition can be achieved. In this regard, a detailed theoretical investigation has been carried out using density functional theory+U calculations to unravel the nature of adsorption, electronic structure, and the magnetic state of the adsorbed NiQ molecule. The present investigation predicts that the NiQ molecule undergoes an on-surface spin state transition to a high spin state when adsorbed on a Co(001) surface.

5.2 Computational Details

The density functional theory (DFT) calculations have been employed to study the magnetic interaction of a NiQ molecule with a ferromagnetic cobalt surface. The calculations were performed using the plane wave, pseudopotential as implemented in Vienna ab initio simulation package (VASP) (Kresse and Furthmüller, 1996) with projector-augmented-wave (PAW) potential (Blöchl, 1994). Generalized Gradient Approximation (GGA) was used with Perdew-Burke-Ernzerhof parameterization for exchange-correlation function (Perdew et al., 1996). The DFT+U technique has been implemented in order to capture the strong electron-electron correlation effect which exists in the partially filled 3d shell of TM and missing correlation effect beyond GGA. This technique is quite promising one to achieve the precise spin state of the molecule. The on-site Coulomb and exchange parameters U and J were chosen as 5.0 eV and 1.0 eV for Ni atom. A $3 \times 3 \times 1$ Monkhorst-Pack k-points was used for reciprocal space sampling. A plane wave kinetic energy cutoff 500 eV was considered. The convergence criterion was set to 10^{-5} eV for the self-consistent electronic minimization. The Ni(II)-Quinonoid molecule has been represented on top of three atomic Co layers within a large supercell of the Co(001) magnetic substrate (8×5 lateral supercell) and applied the boundary conditions to maintain the periodicity of the surface. The geometry of the molecule on the Co surface has been optimized by relaxing the atoms' positions until all residual inter-atomic forces were minimized up to 0.01 eV/Å. Two bottom layers of Co atoms of the substrate were kept fixed during the optimization process to minimize the computational effort.

5.3 Results and Discussions

5.3.1 Optimized Geometry

The square-planar NiQ molecular structure has been modeled according to the reported data (Kar et al., 2017). To start with, the geometry of the isolated NiQ molecule has been optimized in the gas phase. The optimized structure of NiQ molecule is shown in Figure 5.1. The molecule remains planar with the average Ni–O(N) bond lengths of the molecule being 1.868 Å, which is close to the experimental value (1.866 Å).

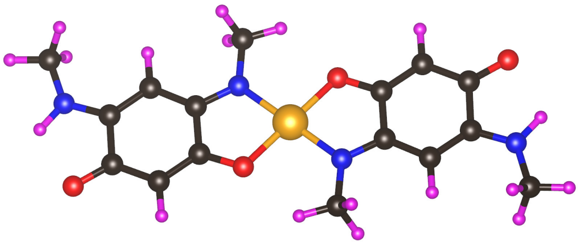

Figure 5.1 The optimized structure of the NiQ molecule. Ni, O, N, C, and H atoms are represented through the orange, red, blue, black, and magenta colored balls, respectively.

Next, the optimized NiQ molecule has been placed on the Co(001) substrate in two different configurations, namely the HOLLOW and TOP adsorption sites, as shown in Figure 5.2 and Figure 5.3, respectively. In the HOLLOW configuration, the molecule adsorbed on the Co(001) surface in such a way that the central Ni atom of the molecule is placed on top of a second layer Co atom (i.e., hollow site) of the Co(001) substrate (see Figure 5.2). The optimized distance between the surface and the Ni atom is 1.778 Å. In this configuration, the Ni–O and Ni–N bond lengths have been stretched themselves in such a way that the O and N atoms of the molecule come closer to the surface Co atoms and form direct chemical bonds with the surface. The average Ni–O(N) bond length is increased by 0.204 Å compared to its gas phase structure.

In TOP configuration, the molecule is placed on the Co(001) surface such that the Ni atom sits exactly on top of a surface Co atom (see Figure 5.3). The optimized molecule substrate separation in this configuration is 2.4864 Å. In the optimized structure, the O atoms at the hollow site are now positioned at the top site as the ligands

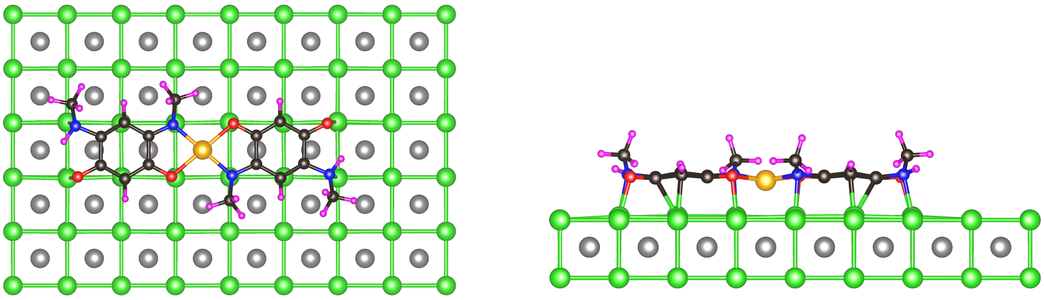

Figure 5.2 Top and side view of the chemisorbed NiQ molecule on the surface of Co(001), in the HOLLOW configuration. The NiQ atoms are represented in the same way as in Figure 5.1, and green and grey coloured spheres represent the Co atoms. To make the Co positions in the second layer (hollow site) clearer, these Co atoms are represented with gray color and their bonds with other layer Co atoms are not shown.

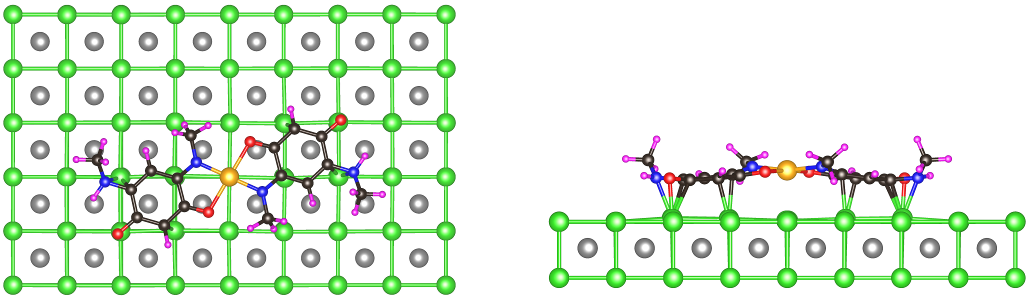

Figure 5.3 Top and side view of the chemisorbed NiQ molecule on the surface of Co(001), in the TOP configuration. The color code of the atoms is done in the same way as in Figure 5.2.

connected to the Ni are forced to stretch. This essentially results in the Ni-O bond length increase, whereas the Ni-N bond length is not significantly altered. This is attributed to the fact that the nearest C atoms that were initially bonded with Co atoms, now prevent the further stretching of Ni-N bonds, making the average bond length to increase by 0.128 Å. These calculations show that the HOLLOW configuration is energetically more favorable, whereas the molecule is structurally distorted more in the TOP configuration. The magnetic moment of the Ni atom, Ni–O(N) bond length in the gas phase and chemisorbed configurations are shown in Table 5.1 and Table 5.2.

The calculations predict a zero magnetic moment (S = 0) for the gas-phase NiQ molecule, consistent with experiments (Kar et al., 2017). Note that, with regard to the

Table 5.1 Ni–O and Ni–N bond lengths (in Å) of NiQ in the gas phase, and chemisorbed in HOLLOW and TOP configurations.

	Gas phase	**HOLLOW**	**TOP**
Ni–O1	1.8562	2.1151	2.1156
Ni–O2	1.8558	2.1158	2.1166
Ni–N1	1.8782	2.0290	1.8778
Ni–N2	1.8799	2.0295	1.8778
Average	1.8683	2.0724	1.9967

Table 5.2 The magnetic moment on Ni and total molecular moment (in μ_B) of NiQ in the gas phase, and chemisorbed in HOLLOW and TOP configurations.

	Gas phase	**HOLLOW**	**TOP**
Ni magnetic moment	0.000	1.178	1.133
Total magnetic moment	0.000	1.561	1.337

obtained S = 0 state, it has been verified that the zero-moment property is robust against variations of the Coulomb U value between 2 and 8 eV. The molecular spin moment changes when the molecule is chemisorbed on the Co(001) surface, to 1.561 and 1.337 μ_B for HOLLOW and TOP site, respectively. Thus, an on-surface spin state switching to a high-spin state can be induced by the adsorption of NiQ on the Co substrate. Compared to the reported magneto-chemical reaction (Kar et al., 2017) in which two MeOH groups bond to Ni in the axial ligand positions, in the on-surface reaction, the molecule bonds one-sided to the top-layer surface atoms. The spin moment on the molecule is less than what would be expected for the high-spin S = 1 state. This is, however, not unexpected due to the extended hybridization of the quinonoid atoms to the surface atoms and the structural distortion.

The physisorption of the planar molecules is also possible on the Co surface (Ali

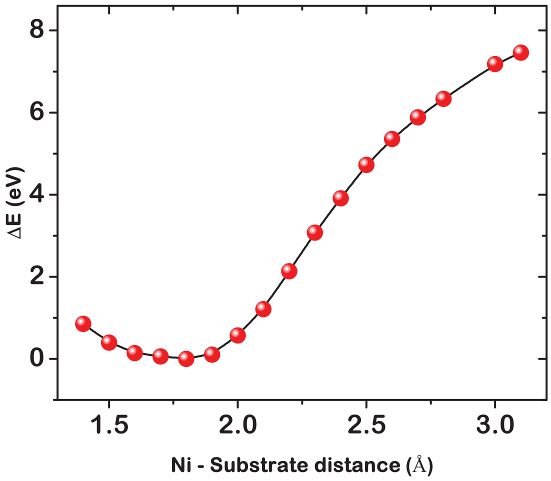

Figure 5.4 Calculated relative total energy (ΔE) versus the molecule–surface distance. The total-energy curve displays its energy minima at 1.8 Å, which corresponds to chemisorption of the NiQ molecule on the Co(001) substrate in HOLLOW configuration.

et al., 2009). Thus, observed for such physisorption of NiQ on Co surface. The distance between the NiQ molecule and Co(001) surface has been changed successively in both HOLLOW and TOP configurations and subsequently calculated the total energy of the systems in each situation. The computed energy versus distance curve for the HOLLOW site absorption is shown in Figure 5.4. The single energy minima at 1.8 Å clearly indicates that only chemisorption of the molecule on Co(001) is possible. Weak physisorption of the molecule has been observed at a distance of 3.5 Å in TOP configuration. However, the calculated energy barrier was very small, and the magnetic interaction was found to be negligible in this configuration. The details of geometric structure and magnetic behavior in physisorption in TOP geometry are given in Appendix A.

5.3.2 Electronic Structure and Magnetic Properties

The distorted molecular geometry in chemisorption leads to a significant change in the electronic energy levels and their spin occupation, which further affects the magnetic properties of the molecule. In the square-planar Ni(II)-quinonoid molecule with d^8 configuration, the four ligands (two oxygen and two nitrogen atoms) are bonded to the central Ni atom in the basal $xy-$plane and provide a crystal-field effect on the Ni $3d$-

orbitals. The Coulomb repulsion, along with strong σ-type hybridization leads to a strong ligand field (LF) that splits the d-orbitals of Ni in degenerate t_{2g} and e_g levels. In the absence of axial coordination, one of the e_g orbitals, i.e., d_{z^2} is relatively lower in energy compared to the other, $d_{x^2-y^2}$. A stronger LF effect is imposed on the orbitals when the Ni–O, and Ni–N bond lengths are shorter due to the strong hybridization and Coulomb repulsion. As a result, all d-electrons occupy the lower, LF-splitting dominated energy levels and yielded a low-spin state ($S = 0$) in the gas phase, where all d-orbitals are entirely occupied, except $d_{x^2-y^2}$ which is completely empty (see Figure 5.5a).

The Bader charges for the chemisorbed NiQ molecule in HOLLOW and TOP configurations have been calculated to account for the charge transfer taking place between the molecule and the substrate. It has been observed that the molecule gains an additional electron charge of 2.267 and 1.959 from the Co surface in the HOLLOW and TOP configuration, respectively. The Bader charge on the Ni atom increases however only by 0.169 and 0.090, respectively.

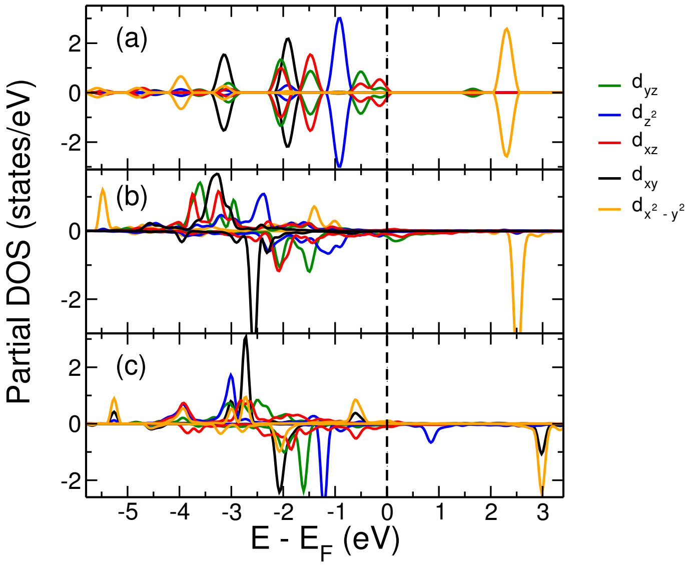

Figure 5.5 d-orbital projected DOS of Ni atom in (**a**) gas phase NiQ; (**b**) chemisorbed in HOLLOW configuration; and (**c**) chemisorbed in TOP configuration. d_{xy}, $d_{yz}, d_{zx}, d_{z^2-r^2}$ and $d_{x^2-y^2}$ are shown as black, green, red, blue and orange line respectively. Positive and negative values, respectively show Spin-up and spin-down DOS.

In the case of molecular chemisorption, electrons in the outer-plane π-orbitals of the quinonoid strongly interact with the surface state electrons and form chemical bonds between the molecule and surface atoms. This results in the stretching of Ni–O(N), which causes a reduction of the LF effect and subsequently reduces the $d_{x^2-y^2}$ orbital energy. In this situation, the intra-atomic exchange interaction becomes essential, and the electrons occupy the Ni-3d orbitals according to Hund's rule. Hence, the $d_{x^2-y^2}$ orbital level, which was completely unoccupied before, is now partially occupied (see Figure 5.5b,c). This explains the change in the spin state of a chemisorbed NiQ molecule governed by the shift in the energy level of the $d_{x^2-y^2}$ orbital, as shown in Figure 5.5.

The magnetic exchange interaction energies E^{ex} in different chemisorption configurations of the molecule are calculated using $E^{ex} = E^{AFM} - E^{FM}$, where E^{AFM} and E^{FM} are the total energies of anti-parallel and parallel spin alignment between the central Ni atom of the molecule and substrate Co atoms, respectively. The calculation shows that the molecule is ferromagnetically coupled with the substrate with coupling energy of 68 and 88 meV for HOLLOW and TOP configurations, respectively.

To understand the spin coupling mechanism, the atom projected density of states (PDOS) of the systems had been investigated carefully. In the HOLLOW configuration, the Ni-ligating O and N atoms are located on top of the surface Co atoms and form chemical bonds with the substrate Co atoms underneath (Figure 5.8). It has been observed that there were overlapping peaks of Co, N, and O projected densities of states marked with vertical arrows in the Figure 5.6a, indicating strong hybridization between out-of-plane orbitals (d_{z^2}, d_{xz}, d_{yz}, and p_z) of Co, O, and N atoms. The total charge density plot, shown in Figure 5.7 (left) as light green hypersurface, also confirms that the orbital overlapping is only between surface Co and molecular ligand's orbitals as there is no direct charge density overlap between the central Ni atom of the molecule and the Co surface atoms. This clearly indicates that the molecule interacts with the substrate only through its ligands, which in turn strongly favors magnetic coupling through the indirect superexchange interaction.

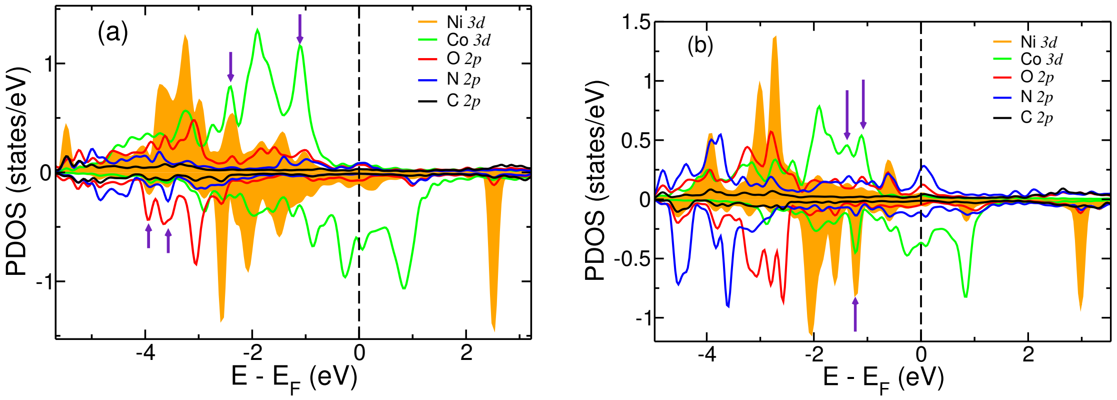

Figure 5.6 Atom-projected partial DOS of chemisorbed NiQ molecule on Co(001): (**a**) NiQ adsorbed in HOLLOW configuration; and (**b**) NiQ adsorbed in TOP configuration. Positive and negative values, respectively show Spin-up and spin-down DOS.

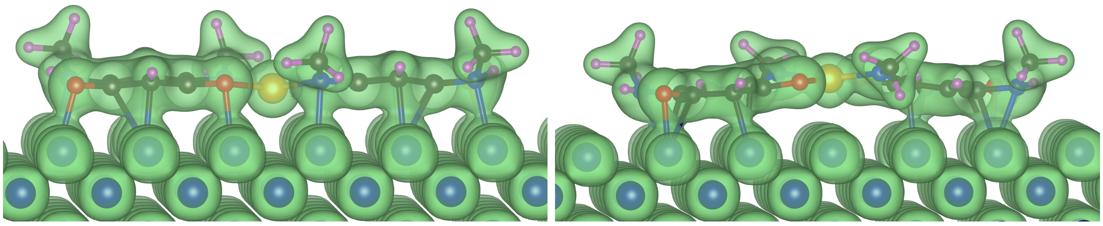

Figure 5.7 Computed charge density (depicted by the light green hypersurface) of NiQ: (**left**) in HOLLOW configuration; and (**right**) in TOP configuration. The charge densities reveal that hybridization between the surface and molecule occurs only through the quinonoid ligands.

The computed total spin moment on the molecule is 1.561 μ_B in the HOLLOW position, whereas 1.178 μ_B spin moment is located on the central Ni atoms (Table 5.1). A small spin-polarization is also observed on the ligand atoms, which further indicates that the exchange coupling path between the magnetic center of the molecule and the spins of Co surface atoms goes through the molecular ligands. To obtain more insight into the nature and path of the magnetic exchange interaction between magnetic centers, the *partial* magnetization density of the system was computed, shown in Figure 5.8, at the energy region where the hybridization between atomic orbitals of Co surface Co and molecular orbitals from N, O, and Ni are dominant, which is predicted from the atom projected DOS (see the overlapping peaks in Figure 5.6a). It is evident from the magnetization density plot that the magnetic exchange interaction between Ni and surface Co atoms is mainly mediated through ligands of the molecule. The negative magnetic moments on O and N atoms, shown through the light blue isosurface in this figure, indicate a 90° ferromagnetic indirect exchange mechanism with the Goodenough–Kanamori superexchange rule. A very weak direct exchange interaction could also be possible when one considers some of the noticeable PDOS peaks of Ni and Co atoms that have overlap, as indicated with vertical bars in the atom projected DOS shown in Figure 5.6a. However, any direct charge or spin-density overlap between Ni and Co atoms was not found in the charge density and magnetization plots.

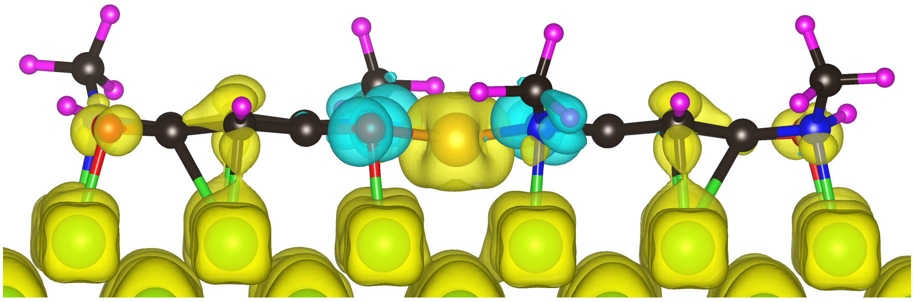

Figure 5.8 Partial magnetization density computed for an energy window indicated with two arrow marks in the spin-down channel of the PDOS plot for the HOLLOW configuration (Figure 5.6a). The magnetization density clearly shows the ferromagnetic coupling between molecule and surface, and also that an indirect superexchange mechanism is more dominant than the direct exchange interaction. The bright yellow and light blue hypersurfaces depict the positive and negative magnetization densities, respectively.

In the case of chemisorption of the molecule in the TOP configuration, the direct O and N atoms bonding to the Ni atom are in the hollow position with respect to the surface atoms and do not directly bond to the surface Co atoms. However, there are other atoms of the quinonoid ligand that chemically bond to the surface. The total charge density plot in Figure 5.7 (right) indicates the non-overlapping nature of the orbital wave functions between the central Ni atom and the surface. However, quinonoid ligand atoms of the molecule strongly interact with the surface Co atoms which are suggested by the overlapping peaks present in the atom-projected PDOS plot (Figure

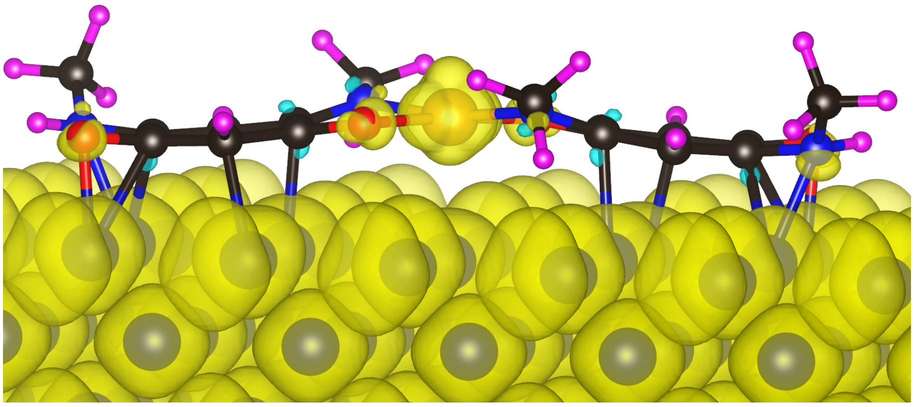

Figure 5.9 Computed total magnetization density of NiQ molecule chemisorbed in the TOP configuration. The magnetization density on ligand N and C atoms points to a ferromagnetic coupling between the molecule and substrate through a direct exchange path. The bright yellow and light blue hypersurfaces depict the positive and negative magnetization densities, respectively.

5.6b) marked with vertical arrows, which indicates the strong hybridization between out-of-plane orbitals (d_{z^2}) of surface Co with O and N $p-$orbitals. The magnetization density calculated for the TOP configuration is shown in Figure 5.9. A small negative magnetization density is present on the ligand atoms, as shown by the light blue isosurface that indicates an indirect exchange interaction between the Ni spin center and the magnetic Co surface atoms, mediated through the ligand.

5.4 Conclusions

To conclude, a SCO from $S = 0$ in the gas phase to a nearly high-spin $S = 1$ state has been observed when the NiQ molecule is chemisorbed on the Co surface. This is attributed due to the covalent interactions between the molecule's ligands and surface. This, in turn, leads to a SCO of the non-magnetic NiQ into a spin-bearing molecule due to the stretching of the Ni–O, and Ni–N bond lengths. It has also been observed that chemisorption at a HOLLOW site is found to be energetically most favorable. An indirect superexchange path through the molecular ligand stabilizes the Ni spin of the molecule parallel to the substrate magnetization direction. In view of the on-going efforts to realize bistable molecules with the reversible spin state that are atomically precisely anchored to substrates, a future research direction is to explore the possibility of achieving spin-switching on non-magnetic metallic substrates. This present investigation not only sheds light on the interactions of a NiQ molecule with a magnetic Co(001) substrate but also suggests a possible pathway to explore planar metal-quinonoid molecules as a spin-bearing interface molecule in future spintronic devices. Further, it will be interesting to study the change in spin state and magnetic anisotropy energy of the TM atom in the chemisorbed molecules by adding an axial ligand, which will be discussed in the next chapter.

Chapter 6

Unprecedented Magnetic Interaction of Chemisorbed Ni^{II}-Dinuclear Quinonoid Molecule on a Co(001) Substrate

In this chapter, an unexpected antiferromagnetic coupling of the Ni-dinuclear molecule to the ferromagnetic Co(001) substrate shall be discussed. The spin state and oxidation state of the molecule switches when the molecule is absorbed on the Co(001) surface. An indirect exchange interaction through the ligands of the molecule stabilizes the spin moment of the molecule in antiferromagnetic alignment with respect to the Co surface magnetization. Further, tailoring the spin state and magnetic anisotropy energy of the molecule through the magneto-chemical method by adding Cl atom as an axial ligand to the magnetic center of the molecule shall also be discussed.

6.1 Introduction

The use of magnetic molecules in spintronics may allow the development of nanoscale devices with improved performance or new functionalities. In this regard, spin-bearing planer molecules are of great research interest for the past two decades to design future spin-based devices (Rocha et al., 2005; Scheybal et al., 2005; Dediu et al., 2009; Bogani and Wernsdorfer, 2008). It has been observed that a wide range of tunable chemical functionalities along with different on-surface magneto-chemical methods allow efficient spin state manipulation of these molecules while adsorbing on the magnetic surface (Bernien et al., 2009; Wäckerlin et al., 2010, 2012; Ballav et al., 2013). Furthermore, the development of the poly-nuclear architectures in which multiple transition metal (TM) centers are covalently linking into poly-nuclear molecules impart the cooperativity and open up the possibility to access more abrupt, hysteric, and multi-state molecular switches (Hogue et al., 2018; Phonsri et al., 2019). Quinonoid molecules have an indispensable role in linking multiple metal centers (Ward, 1996; Kitagawa and Kawata, 2002). Several metal-organic molecules have already been synthesized using quinonoid ligands and studied extensively looking at different applications such as surface chemistry, coordination polymers, molecular switches, and catalysts (Dei et al., 2004; Kim et al., 2013). Recently, Ni-Quinonoid (NiQ) has been reported as a spin crossover complex, where the molecule undergoes a reversible temperature-robust spin state switching due to the magneto-chemical reaction in the molecule after adding the methanol (Kar et al., 2017). In search of new materials to address the magnetic switching at a molecular level, a recent study shows that the NiQ molecule undergoes a substrate-induced spin state switching through strong ferromagnetic spin interactions with Co(001) substrate (Reddy et al., 2019). Also, the magnetic properties of a series of spin-bearing TM-dinuclear quinonoid molecules in which the quinonoid molecule link the two TM atoms have recently been investigated (Reddy and Tarfder, 2020). However, despite technological applications, it is essential to understand the molecular adsorption and its interactions with the magnetic substrates.

In the present work, the magnetic properties of a Ni-dinuclear molecule adsorbed on a Co(001) substrate have been studied using first-principles calculations. An unexpectedly strong antiferromagnetic exchange interaction has been observed between spins of the molecule and substrate, mediated through ligands in the molecule. Further, the spin state of the Ni atom in the adsorbed molecule has been tailored using the magneto-chemical method by adding Cl atom as an axial ligand to the Ni atom. The spin state stability of the Ni atom has been analyzed further by calculating the magnetic anisotropy energy (MAE).

6.2 Computational Details

In this work, the density functional theory (DFT) calculations have been employed by using plane wave pseudopotential method as implemented in Vienna Ab-initio Simulation Package (VASP) (Kresse and Furthmüller, 1996) considering the projector-augmented-plane wave (PAW) potential (Blöchl, 1994). The Generalized Gradient Approximation (GGA) in the form of Perdew-Burke-Ernzerhof (Perdew et al., 1996) parametrization was used for the exchange-correlation functional. Further, the DFT+U technique has been implemented to capture the strong electron-electron correlation, which exists in the partially filled 3d shell and missing correlation in the conventional GGA (Dudarev et al., 1998). This technique has been proven to be a very promising technique to achieve the precise spin state of molecules and low-dimensional magnetic systems (Tarafder et al., 2012; Maldonado et al., 2013). The on-site Coulomb and exchange parameters U and J for the partially filled d orbitals of Ni atom were chosen to be 5.0 and 1.0 eV, respectively (Reddy et al., 2019). A sufficiently large plane-wave cutoff energy of 500 eV was used. The reciprocal space was sampled by using $3\times3\times1$ Monkhorst-Pack k-point grid. The convergence criterion was set to 10^{-5} eV for the self-consistent electronic energy minimization. The Ni-dinuclear molecule has been placed on top of a large Co(001) surface (unit of 9×6 lateral Co(100) surface supercell) and applied boundary conditions to maintain the periodicity of the surface. The ground-state structure of the system was then obtained by relaxing the atomic positions of the atoms in the molecule and the atoms of the top layer in Co substrate. The relaxation process has been continued until all residual inter-atomic forces were minimized to less than 0.01 eV/Å.

6.3 Results and Discussions

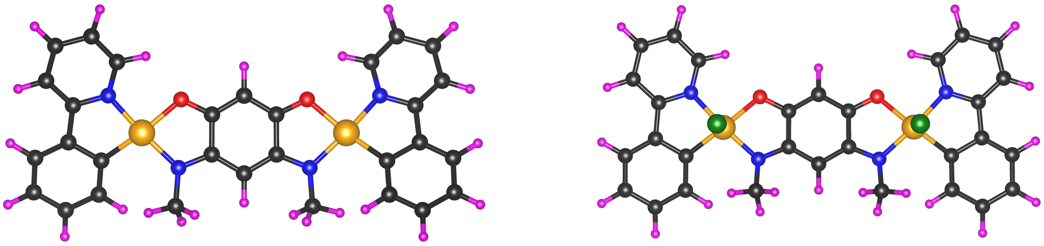

Figure 6.1 Optimized molecular structure of the Ni^{II}-dinuclear molecule in without-Cl **(left)** and with-Cl **(right)** configurations in the gas phase. Ni, O, N, Cl, C, and H atoms are represented by orange, red, blue, green, black, and magenta colored balls, respectively.

The calculations show that the HOLLOW configuration, in which both the Ni atoms are sitting on top of hollow sites position of the surface Co atoms, is energetically the most stable configuration. A similar situation has also been observed in the case of mono-nuclear Ni-quinonoid molecule (Reddy et al., 2019). The optimized geometry of the molecules in the gas phase and the adsorption phase is shown in Figure 6.1 and Figure 6.2, respectively.

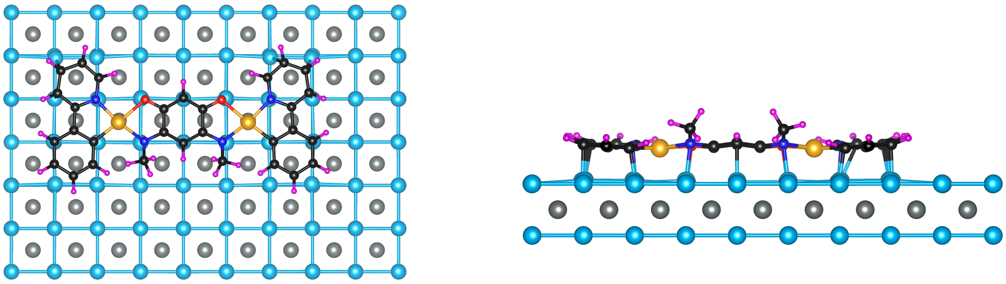

Figure 6.2 Top and side view of the chemisorbed Ni-dinuclear molecule on the surface of Co(001). The Ni, O, N, C, and H atoms in the molecule are represented in the same way as in Figure 1. To make the hollow site Co atom positions clearer, the top and hollow site of the Co atoms are represented by cyan, and grey coloured spheres, respectively, and the bonds of hollow site Co atoms with the other top site Co atoms are not shown.

The optimized molecule in the gas phase has been placed on the magnetic Co(001) substrate, where the TM center of Ni-dinuclear molecule, i.e. Ni atom, on top of the

HOLLOW site of the Co(001) substrate as shown in Figure. 6.2. The optimal distance between the Ni atom in the molecule and surface layer is found to be 1.72 Å, indicates that the molecule is chemisorbed to the Co(001) substrate. The ligand atoms of the molecule tend to make a direct chemical bond with the nearest surface Co atoms in order to stabilize the geometry. As a result, the average Ni-ligand bond lengths have been stretched themselves and increased by ~0.2 Å in the chemisorbed structure (2.1 Å) compare to its gas phase geometry (1.9 Å) (see Table 6.1).

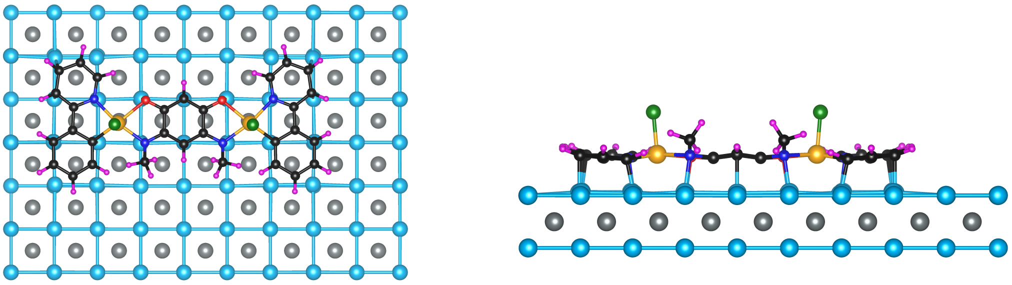

Figure 6.3 Top and side view of the chemisorbed Ni^{II}-dinuclear molecule (with-Cl configuration) on the surface of Co(001). The molecule and substrate atoms are represented in the same way as in Figure 1. and Figure 2.

In the gas phase, the molecule is diamagnetic, which can be well understood from the square planer coordination of Ni^{+2} atom in the molecule. Comparatively shorter Ni-ligand bond lengths introduce a strong ligand field effect on Ni 3d-orbitals that forces all eight d electrons in Ni atom to occupy four lower energy levels, and this leads to stabilized the molecule in the diamagnetic low spin state (S=0) (Reddy and Tarfder, 2020). However, the magnetic structure of the molecule has changed upon adsorption on Co substrate. The obtained magnetic moment on each of Ni atom is ~0.6 μ_B and the total magnetic moment of the molecule is 1.654 μ_B in the Ni^{II}-dinuclear molecule in the adsorbed state. Although the spin moment of Ni^{2+} atom in a square-planar molecule is expected to be switched from S=0 to S=1, the calculation shows that the spin moment on the Ni atom is nearly S=$\frac{1}{2}$. This unusual change in the magnetic moment of the Ni atom could be possible due to an electron transfer between the surface and the molecule. Note that there is a strong hybridization of the bipyridine and quinonoid atoms to the Co surface layer which triggers the substrate-induced spin state switching of the Ni atom

Table 6.1 The Ni-ligand lengths (in Å) and magnetic moment on Ni (in μ_B) (in parentheses, Ni_2 atom values) of the molecule in the gas phase and chemisorbed in without-Cl and with-Cl configurations.

	Gas phase		**Chemisorbed**	
	Without-Cl	**With-Cl**	**Without-Cl**	**With-Cl**
Ni-O	1.930 (1.930)	1.977 (1.975)	2.234 (2.234)	2.307 (2.306)
Ni-C	1.892 (1.892)	1.915 (1.915)	2.018 (2.022)	2.016 (2.017)
Ni-N_1	1.896 (1.896)	1.910 (1.910)	2.059 (2.070)	2.135 (2.138)
Ni-N_2	1.895 (1.895)	1.932 (1.930)	2.068 (2.074)	2.161 (2.163)
Ni-Cl	——	2.300 (2.300)	——	2.230 (2.229)
Average	1.903 (1.903)	2.007 (2.006)	2.096 (2.101)	2.170 (2.171)
Ni magnetic moment	-0.012 (-0.012)	0.680 (0.678)	-0.585 (-0.598)	-1.133 (-1.138)

in the chemisorbed the molecule.

To understand the unusual magnetic behavior of the molecule upon absorption, the d-orbital density of states of Ni atom in the molecule has been plotted and shown in Figure 6.4c. Interestingly, all the 9 d orbitals out of 10 are occupied, only the $d_{x^2-y^2}$-up channel is unoccupied and present in the conduction band, this confirms an extra electron present in the Ni-d orbitals which may transfer from the ligand or surface. The Bader charge analysis shows that overall 3.59 e charges have been transferred to the molecule from the Co surface. There one can conclude that the extra electron in Ni d orbital is transferred from the surface.

Since there is a large electron affinity present in the molecule, it would be interesting to study the effect of chlorination of the molecule. Also, chlorination of this type of molecule is very common that frequently occurs during the synthesis process. The calculations show that both the Ni atoms of the chlorinated molecule are in the S=$\frac{1}{2}$ spin state in the gas phase, which is expected as it is now in Ni^{+3} state. On absorption, the spin state of the Ni atoms in the chlorinated molecules moves to S=1 state, which

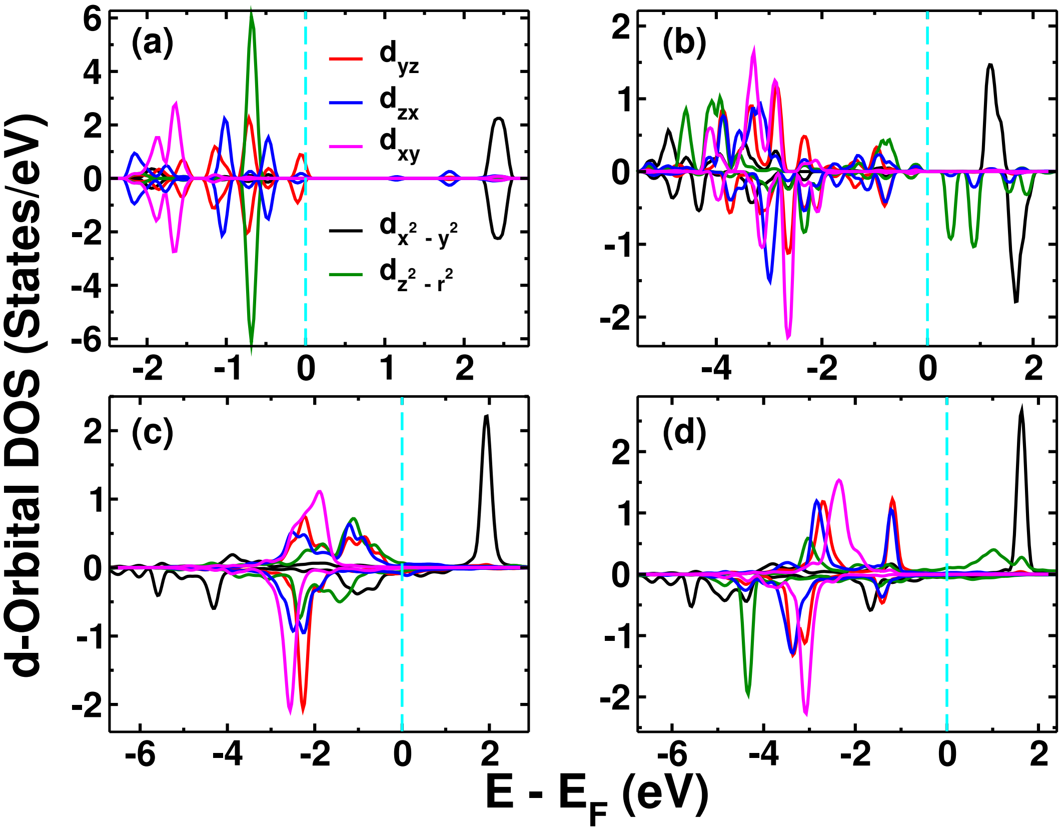

Figure 6.4 d-orbital projected DOS of Ni atom in the gas phase molecule, (a) without-Cl configuration, and (b) with-Cl configuration. (c) and (d) are the d-orbital projected DOS of Ni atom in the chemisorbed molecules on Co(001) in without-Cl and with-Cl configurations, respectively. The Fermi level (E_F) is set at E=0.

indicates that upon adsorption, the change in magnetization of the chlorinated molecule follows the similar root as of unchlorinated one. This can also be confirmed from the d-orbital density of states of Ni atom shown in Figure 6.4d, where in addition to the $d_{x^2-y^2}$-up orbital, the d_{z^2}-up orbital is also in the conduction band.

In the case of the chemisorbed molecule, as mentioned above, the molecule-surface interaction stretches the Ni-ligand bond lengths of the molecule mainly due to the direct chemical bonding between ligands and surface Co atoms. As a result, the molecular geometry got distorted because of the in-plane mechanical strain, which affects d-orbital energy levels. The increased in-plane Ni-ligand bond lengths give rise to the reduction of ligand field effect, which leads to the lowering of the e_g (d_{Z^2}, $d_{x^2-y^2}$) orbital energy. Thus, the electrons occupy the Ni-3d orbitals according to Hund's rule by filling all majority spin levels followed by three levels in the minority spin channel that results to S=1 spin state to the Ni^{+2} atom with electron configuration is $\sim$ t$_{2g}^{(5)}$e$_{g}^{(3)}$. However, due to a strong electron affinity of the molecule attracts electrons from the surface and fill one empty d-orbitals of Ni. As a result, four spin-up and five spin-down d-orbitals are occupied with electrons, leads to the spin state of the Ni atom to $S = \frac{1}{2}$. Thus, the electronic configuration of Ni atoms in the chemisorbed molecule in without-Cl configuration is $\sim$ t$_{2g}^{(6)}$e$_{g}^{(3)}$. In the case of the chlorinated molecule, the only change in the electron distribution is the d$_{z^2}$ orbital electron is used to make the bond with the axial Cl atom and hence the d-electron configuration, in this case, is $\sim$ t$_{2g}^{(6)}$e$_{g}^{(2)}$. Interestingly in both cases, whether the molecule is chlorinated or not, magnetic centers of the molecules are antiferromagnetically coupled with surface magnetization. The magnetic exchange interaction energies (E^{ex}) have been calculated using E^{ex}=E^{FM}-E^{AFM}, where E^{FM} and E^{AFM} are the total energies of parallel and anti-parallel spin alignment between the Ni atom in the molecule and substrate Co atoms, respectively. The calculated E^{ex} values are 0.299 eV, and 0.155 eV for chlorinated and unchlorinated molecules, respectively, indicates very strong magnetic coupling between the molecule and the surface.

The magnetic coupling of the Ni d-shell electrons can occur either by a direct exchange interaction with the out-of-plane orbitals of the Co substrate (Javaid et al., 2010; Oppeneer et al., 2009) or via an indirect exchange interaction through the atomic orbitals of the ligand atoms (Chylarecka et al., 2011; Barth, 2007). Since the Ni atoms are sitting in the hollow position, the possibility of a strong direct exchange interaction (overlap between the d$_{z^2}$ orbital of Ni and out-of-planes orbitals of Co) with the first layer Co atom is less. However, the spin of Ni can strongly interact with the second layer of the Co-atoms. The large broadening of the d$_{z^2}$ of Ni atom indicates that possibility. On the other hand, the AFM coupling can be assigned to an indirect coupling via electrons present in the ligand atoms. To have a clear picture of the coupling process, the magnetization densities have been plotted for both the chlorinated and unchlorinated systems and shown in Figure 6.5.

Note that the ligand atoms, in particular, O atoms of the molecule which make a direct bond with the surface Co atoms gain positive magnetization density. The bonding to the Co out-of-plane orbitals occurs via interaction of the spin-down electron from the

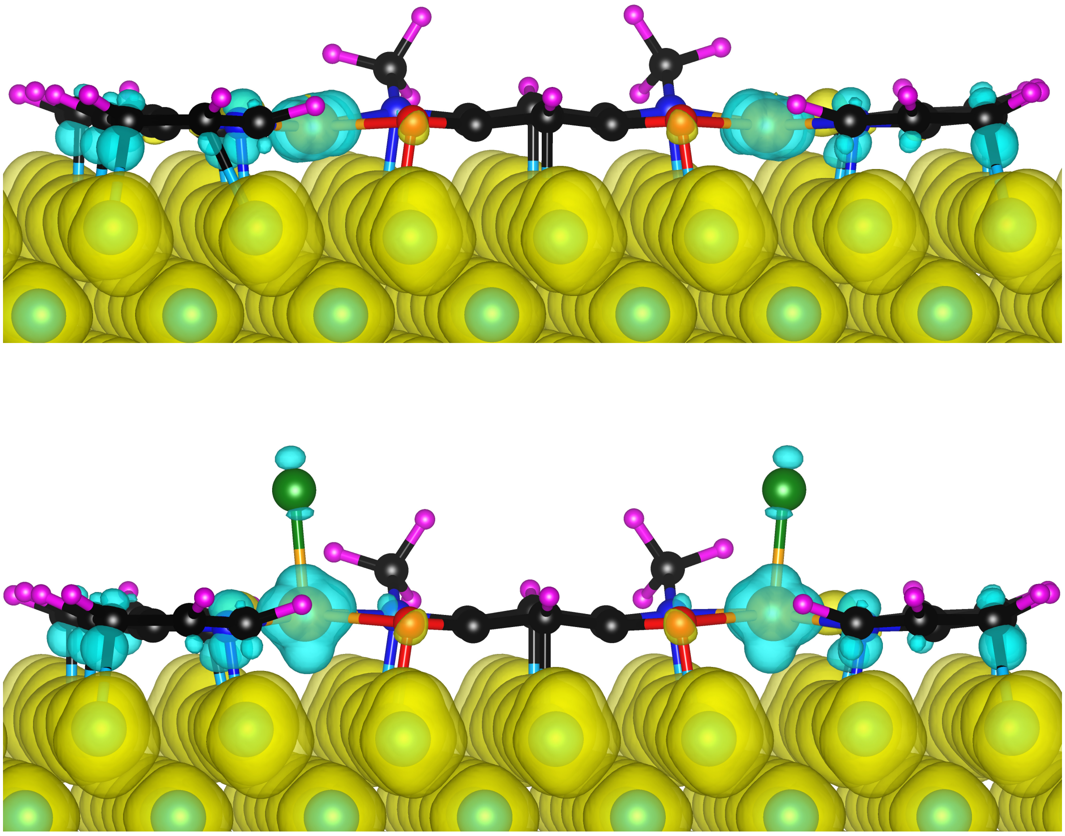

Figure 6.5 Computed magnetization density of chemisorbed molecule in without-Cl configuration (Top) and with-Cl configuration (Bottom). The bright yellow and light blue hypersurfaces represents the positive and negative magnetization densities, respectively.

O p_z orbitals. These O p_z orbital is also forms a π bond with Ni_{3d} orbitals (d_{xz}, d_{yz}). This configuration indicates that there is a 90^o cation-anion-cation interaction scheme can be considered within the Goodenough-Kanamori-Anderson (GKA) modelGoodenough (1963). Two cations involved in the interaction are the Ni ion on one side, and the Co atom from the substrate on the other side, while the O atom provides the anion part of the chain. The formation of the π-bond between the Ni d_{xz},d_{yz} orbitals and the O p_z orbitals leads to an exchange interaction between the spin-up electron from O and the Ni ion. The substrate induced spin-up polarization of the oxygen p electrons, together with Pauli's exclusion principle, force the Ni d_π electron to align their spins anti-parallel to the electrons of the O p_z orbitals. Therefore, the molecule coupled anti-ferromagnetically with the Co substrate. A very similar situation occurs in the case of chlorinated molecule adsorption. In this case, the extra unpaired electron in d_{z^2} orbital is also aligned anti-parallel to the surface Co spin due to intra-atomic FM interactions that induced a parallel spin alignment in the d shell of Ni atom. Note that the exchange interaction gets significantly increased in the presence of Cl atom in the molecule. This is due to the enhancement of the electron affinity of the molecule. Bader charge analysis shows that the chlorinated molecule absorbs more charge (3.95 e) from the surface compare to the bare molecule absorption. Therefore the transferred charge has more contribution to induced magnetization on ligand atoms, which intern enhances the coupling mechanism.

6.3.1 Magnetic Anisotropy Energy

The stability of the antiferromagnetic ordering for Ni-dinuclear molecule have investigated by estimating the magnetic anisotropy energy (MAE). In general, the ligand field splitting in spin-bearing molecules is larger compared to the spin-orbit coupling, therefore, the second-order perturbative approach can be considered to calculate the MAE. Hence, the 3d orbital resolved MAE of the Ni atoms has been estimated based on the second-order perturbation theory (Wang et al., 1993). Considering up to the first-order correction, the MAE can be expressed as

$$MAE = \sum_{\sigma\sigma'} (2\delta_{\sigma\sigma'} - 1)\zeta^2 \sum_{o^\sigma, u^{\sigma'}} \frac{|< o^\sigma \mid L_z \mid u^{\sigma'} >|^2 - |< o^\sigma \mid L_x \mid u^{\sigma'} >|^2}{E_u^{\sigma'} - E_o^\sigma} \tag{6.1}$$

where ζ is the spin-orbit coupling constant has taken as 74.76 meV and 82.82 meV for Ni^{+1} (without-Cl) and Ni^{+2} (with-Cl) of the chemisorbed molecules, respectively (Cole Jr and Garrett, 1970). E_o^σ and $E_u^{\sigma'}$ are the energy levels of the occupied states with spin $\sigma(< o^\sigma \mid)$ and unoccupied states with spin $\sigma'(\mid u^{\sigma'} >)$. From Eq. 1, it can be seen that MAE increases as the denominator decreases. Thus, the relative arrangement of Ni_{3d} orbitals is essential. Thus, the d-orbital DOS have been calculated using 6×6×1 k-points. The calculated magnetic anisotropy energies are shown in Table 6.2. The positive MAE indicates that the easy axis of magnetization is out-of-plane. It is interesting to note that the MAE is drastically reduced due to the chlorination of the molecule.

Table 6.2 MAE of the Ni atoms in the chemisorbed molecule in without-Cl and with-Cl configurations.

	Without-Cl (in meV)	**With-Cl (in meV)**
Ni_1	1.336	0.035
Ni_2	1.449	0.019

6.4 Conclusions

To conclude, the structural and magnetic properties of a Ni-dinuclear molecule upon adsorption on a Co(001) substrate has been studied successfully. The calculations show that the Ni atom in the molecule undergoes on-surface spin state switching when the molecule chemisorbed to the Co surface. The charge injection into the molecule from Co surface redistributes the charge in the Ni d-orbitals that lead to the spin state switching in the Ni-dinuclear molecule. An indirect exchange coupling between Ni and surface Co atoms mainly mediated via the ligands in the molecules with GKA theory that stabilizes the Ni spin of the molecule anti-parallel to the substrate magnetization direction. In addition to this, the spin state of the Ni atom in the chemisorbed molecule has been tailored successfully by adding Cl atom as an axial ligand to the Ni atom, i.e. magneto-chemical method (chemical stimuli). The present findings in this study demonstrate that the oxidation state of the Ni atom in the molecule without-Cl (with-Cl) configuration changes from Ni^{+2} (Ni^{+3}) in the gas phase to Ni^{+1}(Ni^{+2}) when the molecule chemisorbed to the substrate. Moreover, switching the spin state of the Ni atom in the molecule accompanied by altering the MAE opens up possible applications in future molecular spintronic devices.

Chapter 7

Summary and Outlook

The main aim of my Ph.D. research was to study the Spin Crossover (SCO) phenomena in a class of newly synthesized materials. In this regard, I have considered three different classes of materials such as perovskite oxyhalides, metal-organic coordination polymers, and metal-organic square-planar molecules. Using first-principles electronic structure calculations, I have performed detailed investigations of SCO phenomena in these materials triggered by different external perturbations such as pressure, electric field as well as by changing the local environment and I have successfully explained the microscopic origin of the SCO behavior in these systems.

The SCO triggered by an electric polarization was observed in the perovskite Sr_2CoO_3F (SCOF) system, where SCOF has sandwiched between two ferroelectric $BaTiO_3$ (BTO) layers in a hybrid perovskite heterostructure. The investigation shows that the spin state of the Co atom in SCOF can be controlled by altering the polarization direction of the BTO. On the other hand, the spin state of the SCOF switched systematically from a high-spin to a low-spin by changing the relative orientation of the ferroelectric polarization of BTO give rise to a giant magnetoelectric (ME) coupling. The perovskite heterostructure with a giant ME coupling may provide solutions to the current challenges in conventional magnetic storage media, such as achieving high-speed switching, low power consumption, and high operational stability simultaneously. Further, polarization-induced spin switching of Co atom in the SCOF system opens the possibilities to design and develop advanced spintronic devices in which the minute electric field can control the magnetic state.

In the next part of the investigation, the pressure-driven spin state transition in a Hofmann clathrate coordination polymer, namely $\mathrm{Fe\{OS(CH_3)_2\}_2\{Ag(CN)_2\}_2}$, have been studied. This study reveals that under a relatively low isotropic hydrostatic pressure, the complex shows a reversible spin switching, whereas the system also undergoes a structural phase transition when the applied pressure is anisotropic. The spin state of the Fe atom in the complex transforms from high spin to intermediate spin state due to anisotropic compressibility of the lattice parameters. Moreover, the estimated transition pressure for the spin-state transition and structural transformation is ≈ 0.09 GPa, which could be feasible for experimental laboratory set-up.

In the final part of my thesis, I have investigated the substrate-induced magnetic properties of square-planar metal-organic molecules. The detailed structural, electronic, and magnetic properties of Ni-quinonoid and Ni-dinuclear molecules have been studied upon the adsorption of these molecules on the magnetic Co(001) substrate. It has been observed that in both cases molecule undergoes a spin state switching when adsorbed on the Co(001) surface. The exchange interactions between magnetic centers in the system were carefully investigated. Further, the spin state and magnetic anisotropy energy of Ni atom in the Ni-dinuclear molecule adsorbed on a Co(001) substrate has successfully tailored by introducing adatom as an axial ligand to the central Ni atoms in the molecule. The present study introduced the planar metal-quinonoid square-planar molecules in the spin-interface research field, exploring these molecules as spin-bearing interface molecule in future spintronic devices will be an essential topic of research in the future.

Future Prospects

- The detailed investigation of SCOF provides a pathway for exploring polarization-induced spin switching in oxyfluoride based SCO materials. In future studies, manipulation of the cation and anion atoms in these compounds, and also applying other external perturbations such as temperature, electric and the magnetic field, which may induce other exotic material properties such as superconductivity, ferromagnetism, and ME coupling. Thus, it would be interesting to assess the potentiality of mixed-anion perovskite compounds for their applications in spintronic devices.

- It would also be interesting to explore more functional properties of Hofmann clathrate coordination polymer compound. In the future, I would like to investigate the spin state switching in this material by applying temperature, light irradiation, electric and magnetic field as an external stimulus. In addition to this, one can also investigate the host-guest properties within this two-dimensional porous Hofmann clathrate molecule that promise adaptable and versatile structural response as well as multistep SCO and molecular sensing applications.

- The detailed understanding of the spin-interface formed with the metal-organic square-planar molecule and magnetic substrate has tremendous potential to realize the future single molecule-based spintronics and quantum computing applications. Moreover, investigating the spin injection and spin transport properties of the planar metal-quinonoid molecules with magnetic as well as non-magnetic electrodes is an immediate step forward to realize the practical molecular spintronic devices.

Appendix A

Physisorption of Nickel-Quinonoid Complex on Co(001) Substrate

The possible physisorption of the NiQ molecule on Co(001) in the TOP configuration has been studied theoretically. The total energy of the molecule in TOP configuration versus the molecule–substrate distance is shown in Figure A.1. The shallow energy minima at 3.5 Å indicates that physisorption of the molecule is possible. Note that, the Van der Waals interactions were not included (see, e.g., (Dion et al., 2004; Tkatchenko and Scheffler, 2009)) in the present calculation, but these would be required for an accurate description of the physisorption. The shallow minimum obtained at 3.5 Å is hence mainly driven by higher-order electrostatic interactions (Ali et al., 2009). The optimized geometry of physisorbed NiQ on the Co surface is shown in Figure A.1 (right). In the physisorption state, the NiQ molecule preserves mostly its gas-phase properties. The Ni–O and Ni–N bond lengths, the average Ni–O(N) bond length (1.8764 Å), and the magnetic moment on the Ni atom are very close to those of the gas-phase molecule.

The computed charge and magnetization densities are shown in Figure A.2. The charge density plot shows that there is no orbital overlap between the molecule and the substrate, and the magnetization density plot exemplifies the non-magnetic nature of the physisorbed molecule on the substrate.

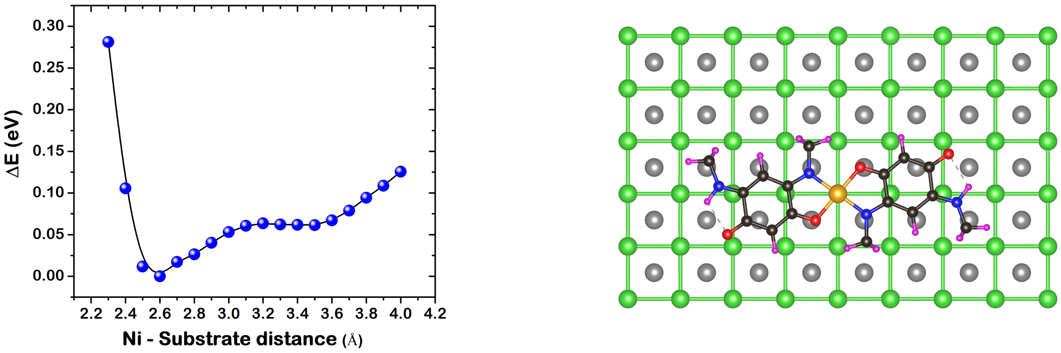

Figure A.1 (**Left**) DFT+*U* calculated relative total energy (ΔE) of NiQ on Co as a function of the Ni atom-substrate distance. The curve clearly shows a shallow energy minima at 3.5 Å, which corresponds to physisorption of the NiQ molecule on Co(001) substrate in TOP configuration. (**Right**) top view of the physisorbed NiQ molecule on the surface of Co(001), in TOP configuration. Ni, O, N, C, H and Co atoms are represented with orange, red, blue, black, magenta and green colored balls. Gray colored balls represent second layer (hollow site) Co atoms.

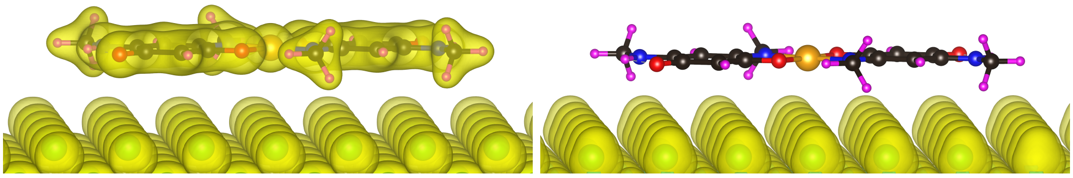

Figure A.2 Calculated charge density (**left**) and magnetization density (**right**) of physisorbed NiQ molecule on Co(001) in the TOP configuration. The computed magnetization density shows that there is no magnetization density present on the molecule.

Bibliography

Ai-Mamouri, M., Edwards, P., Greaves, C., and Slaski, M. (1994). “Synthesis and superconducting properties of the strontium copper oxy-fluoride $SR_2CuO_2F_{2+\delta}$”. *Nature*, 369(6479), 382–384.

Ali, M. E., Sanyal, B., and Oppeneer, P. M. (2009). “Tuning the Magnetic Interaction between Manganese Porphyrins and Ferromagnetic Co Substrate through Dedicated Control of the Adsorption”. *Journal of Physical Chemistry C*, 113(32), 14381–14383.

Ali, M. E., Sanyal, B., and Oppeneer, P. M. (2012). “Electronic Structure, Spin-States, and Spin-Crossover Reaction of Heme-Related Fe-Porphyrins: A Theoretical Perspective”. *Journal of Physical Chemistry B*, 116(20), 5849–5859.

Ali, M. E., Staemmler, V., Illas, F., and Oppeneer, P. M. (2013). “Designing the Redox-Driven Switching of Ferro- to Antiferromagnetic Couplings in Organic Diradicals”. *Journal of Chemical Theory and Computation*, 9(12), 5216–5220.

Anisimov, V. I., Zaanen, J., and Andersen, O. K. (1991). “Band theory and Mott insulators: Hubbard U instead of Stoner I”. *Physical Review B*, 44(3), 943.

Ashcroft, N. W. and Mermin, N. D. (1976). *“Solid State Physics”*. Holt, Rinehart and Winston, New York.

Assirey, E. A. R. (2019). “Perovskite synthesis, properties and their related biochemical and industrial application”. *Saudi Pharmaceutical Journal*, 27(6), 817–829.

Atodiresei, N., Caciuc, V., Lazic, P., and Blügel, S. (2013). “Chemical and van der Waals Interactions at Hybrid Organic-Metal Interfaces”. *www.psi-k.org*.

Auwärter, W., Écija, D., Klappenberger, F., and Barth, J. V. (2015). "Porphyrins at interfaces". *Nature Chemistry*, 7(2), 105–120.

Aviram, A. and Ratner, M. A. (1974). "Molecular rectifiers". *Chemical Physics Letters*, 29(2), 277–283.

Avvisati, G., Gargiani, P., Mondelli, P., Presel, F., Baraldi, A., and Betti, M. G. (2018). "Superexchange pathways stabilize the magnetic coupling of MnPc with Co in a spin interface mediated by graphene". *Physical Review B*, 98(11), 115412.

Bachelet, G., Hamann, D., and Schlüter, M. (1982). "Pseudopotentials that work: From H to Pu". *Physical Review B*, 26(8), 4199.

Baibich, M. N., Broto, J. M., Fert, A., Van Dau, F. N., Petroff, F., Etienne, P., Creuzet, G., Friederich, A., and Chazelas, J. (1988). "Giant magnetoresistance of (001) Fe/(001) Cr magnetic superlattices". *Physical review letters*, 61(21), 2472.

Bairagi, K., Bellec, A., Repain, V., Chacon, C., Girard, Y., Garreau, Y., Lagoute, J., Rousset, S., Breitwieser, R., and Hu, Y.-C. (2015). "Tuning the Magnetic Anisotropy at a Molecule-Metal Interface". *Physical Review Letters*, 114(24), 247203.

Bajaj, N., Bhatt, H., Pandey, K. K., Poswal, H. K., Arya, A., Ghosh, P. S., Garg, N., and Deo, M. N. (2018). "Phase transition in metal–organic complex *trans*-$\mathrm{PtCl_2(PEt_3)_2}$ under pressure: insights into the molecular and crystal structure". *CrystEngComm*, 20(26), 3728–3740.

Ballav, N., Wäckerlin, C., Siewert, D., Oppeneer, P. M., and Jung, T. A. (2013). "Emergence of On-Surface Magnetochemistry". *Journal of Physical Chemistry Letters*, 4(14), 2303–2311.

Banerjee, H., Chakraborty, S., and Saha-Dasgupta, T. (2017). "Design and Control of Cooperativity in Spin-Crossover in Metal-Organic Complexes: A Theoretical Overview". *Inorganics*, 5(3), 47.

Bang, J., Matsuishi, S., Hiraka, H., Fujisaki, F., Otomo, T., Maki, S., Yamaura, J.-i., Kumai, R., Murakami, Y., and Hosono, H. (2014). "Hydrogen ordering and new polymorph of layered perovskite oxyhydrides: $Sr_2VO_{4-x}H_x$". *Journal of the American Chemical Society*, 136(20), 7221–7224.

Barraud, C., Bouzehouane, K., Deranlot, C., Fusil, S., Jabbar, H., Arabski, J., Rakshit, R., Kim, D.-J., Kieber, C., and Boukari, S. (2015). "Unidirectional Spin-Dependent Molecule-Ferromagnet Hybridized States Anisotropy in Cobalt Phthalocyanine Based Magnetic Tunnel Junctions". *Physical Review Letters*, 114(20), 206603.

Barth, J. V. (2007). "Molecular Architectonic on Metal Surfaces". *Annual Review of Physical Chemistry*, 58(1), 375–407. PMID: 17430091.

Barth, J. V. (2009). "Fresh perspectives for surface coordination chemistry". *Surface Science*, 603(10), 1533–1541.

Bartlett, R. J. and Stanton, J. F. (1994). "Applications of Post-Hartree—Fock Methods: A Tutorial". *Reviews in computational chemistry*, 65–169.

Becke, A. D. (1993). "A new mixing of Hartree–Fock and local density-functional theories". *The Journal of chemical physics*, 98(2), 1372–1377.

Bednorz, J. G. and Müller, K. A. (1986). "Possible high T_c superconductivity in the Ba-La-Cu-O system". *Zeitschrift für Physik B Condensed Matter*, 64(2), 189–193.

Benelli, C. and Gatteschi, D. (2015). *"Introduction to Molecular Magnetism – From Transition Metals to Lanthanides"*. John Wiley & Sons.

Bernien, M., Miguel, J., Weis, C., Ali, M. E., Kurde, J., Krumme, B., Panchmatia, P. M., Sanyal, B., Piantek, M., Srivastava, P., et al. (2009). "Tailoring the Nature of Magnetic Coupling of Fe-Porphyrin Molecules to Ferromagnetic Substrates". *Physical review letters*, 102(4), 047202.

Bhandary, S., Brena, B., Panchmatia, P. M., Brumboiu, I., Bernien, M., Weis, C., Krumme, B., Etz, C., Kuch, W., Wende, H., Eriksson, O., and Sanyal, B. (2013). "Manipulation of spin state of iron porphyrin by chemisorption on magnetic substrates". *Physical Review B*, 88(2), 024401.

Bhandary, S., Ghosh, S., Herper, H., Wende, H., Eriksson, O., and Sanyal, B. (2011). "Graphene as a Reversible Spin Manipulator of Molecular Magnets". *Physical Review Letters*, 107(25), 257202.

Binasch, G., Grünberg, P., Saurenbach, F., and Zinn, W. (1989). "Enhanced magnetoresistance in layered magnetic structures with antiferromagnetic interlayer exchange". *Physical review B*, 39(7), 4828.

Blöchl, P. E. (1994). "Projector augmented-wave method". *Physical review B*, 50(24), 17953.

Bogani, L. and Wernsdorfer, W. (2008). "Molecular spintronics using single-molecule magnets". *Nature materials*, 7(3), 179–186.

Boldog, I., Gaspar, A. B., Martinez, V., Pardo-Ibanez, P., Ksenofontov, V., Bhattacharjee, A., Gütlich, P., and Real, J. A. (2008). "Spin-Crossover Nanocrystals with Magnetic, Optical, and Structural Bistability Near Room Temperature". *Angewandte Chemie International Edition*, 47(34), 6433–6437.

Bonhommeau, S., Molnár, G., Galet, A., Zwick, A., Real, J.-A., McGarvey, J. J., and Bousseksou, A. (2005). "One Shot Laser Pulse Induced Reversible Spin Transition in the Spin-Crossover Complex $[\mathrm{Fe}(\mathrm{C_4H_4N_2})\{\mathrm{pt(cn)_4}\}]$ at Room Temperature". *Angewandte Chemie International Edition*, 44(26), 4069–4073.

Bousseksou, A., Molnár, G., Salmon, L., and Nicolazzi, W. (2011). "Molecular spin crossover phenomenon: recent achievements and prospects". *Chemical Society Reviews*, 40(6), 3313–3335.

Briceno, G., Chang, H., Sun, X., Schultz, P. G., and Xiang, X.-D. (1995). "A Class of Cobalt Oxide Magnetoresistance Materials Discovered with Combinatorial Synthesis". *Science*, 270(5234), 273–275.

Brooker, S. (2015). "Spin crossover with thermal hysteresis: Practicalities and lessons learnt". *Chemical Society Reviews*, 44(10), 2880–2892.

Brooker, S. and Kitchen, J. A. (2009). “Nano-magnetic materials: spin crossover compounds *vs.* single molecule magnets *vs.* single chain magnets”. *Dalton Transactions*, 7331–7340.

Brown, E. (1988). “Quinonediimines, monoimines and related compounds”. *The Chemistry of the Quinonoid Compounds*, 2, 1231–1292.

Cambi, L. and Szegö, L. (1931). “Über die magnetische Susceptibilität der komplexen Verbindungen”. *European Journal of Inorganic Chemistry*, 64(10), 2591–2598.

Cava, R. J. (2000). “Oxide Superconductors”. *Journal of the American Ceramic Society*, 83(1), 5–28.

Ceperley, D. M. and Alder, B. J. (1980). “Ground State of the Electron Gas by a Stochastic Method”. *Physical review letters*, 45(7), 566.

Chappert, C., Fert, A., and Van Dau, F. N. (2007). “The emergence of spin electronics in data storage”. *Nature materials*, 6(11), 813–823.

Cheng, J., Kweon, K. E., Larregola, S. A., Ding, Y., Shirako, Y., Marshall, L. G., Li, Z.-Y., Li, X., Dos Santos, A. M., and Suchomel, M. R. (2015). “Charge disproportionation and the pressure-induced insulator–metal transition in cubic perovskite $PbCrO_3$”. *Proceedings of the National Academy of Sciences*, 112(6), 1670–1674.

Chiang, C. K., Fincher Jr, C., Park, Y. W., Heeger, A. J., Shirakawa, H., Louis, E. J., Gau, S. C., and MacDiarmid, A. G. (1977). “Electrical Conductivity in Doped Polyacetylene”. *Physical review letters*, 39(17), 1098.

Chudnovsky, E. M. (1996). “Quantum Hysteresis in Molecular Magnets”. *Science*, 274(5289), 938.

Chylarecka, D., Kim, T. K., Tarafder, K., Müller, K., Gödel, K., Czekaj, I., Wäckerlin, C., Cinchetti, M., Ali, M. E., Piamonteze, C., Schmitt, F., Wüstenberg, J.-P., Ziegler, C., Nolting, F., Aeschlimann, M., Oppeneer, P. M., Ballav, N., and Jung, T. A. (2011). “Indirect Magnetic Coupling of Manganese Porphyrin to a Ferromagnetic Cobalt Substrate”. *The Journal of Physical Chemistry C*, 115(4), 1295–1301.

Cinchetti, M., Dediu, V. A., and Hueso, L. E. (2017). “Activating the molecular spinterface”. *Nature Materials*, 16(5), 507–515.

Clements, J. E., Price, J. R., Neville, S. M., and Kepert, C. J. (2016). “Hysteretic Four-Step Spin Crossover within a Three-Dimensional Porous Hofmann-like Material”. *Angewandte Chemie*, 128(48), 15329–15333.

Cococcioni, M. and De Gironcoli, S. (2005). “Linear response approach to the calculation of the effective interaction parameters in the LDA + U method”. *Physical Review B*, 71(3), 035105.

Cohen, M. L. and Bergstresser, T. (1966). “Band Structures and Pseudopotential Form Factors for Fourteen Semiconductors of the Diamond and Zinc-blende Structures”. *Physical Review*, 141(2), 789.

Cole Jr, G. M. and Garrett, B. B. (1970). “Atomic and molecular spin-orbit coupling constants for 3d transition metal ions”. *Inorganic Chemistry*, 9(8), 1898–1902.

Cornia, A., Mannini, M., Sainctavit, P., and Sessoli, R. (2011). “Chemical strategies and characterization tools for the organization of single molecule magnets on surfaces”. *Chemical Society Reviews*, 40(6), 3076–3091.

Coronado, E., Palacio, F., and Veciana, J. (2003). “Molecule-Based Magnetic Materials”. *Angewandte Chemie Int. Ed.*, 42(23), 2570–2572.

Dagotto, E. (1994). “Correlated electrons in high-temperature superconductors”. *Reviews of Modern Physics*, 66(3), 763.

De Graef, M. and McHenry, M. E. (2012). *“Structure of Materials: An Introduction to Crystallography, Diffraction and Symmetry”*. Cambridge University Press.

Dediu, V. A., Hueso, L. E., Bergenti, I., and Taliani, C. (2009). “Spin routes in organic semiconductors”. *Nature materials*, 8(9), 707.

Deepa, M., Awadhia, A., and Bhandari, S. (2009). “Electrochemistry of poly (3,4-ethylenedioxythiophene)-polyaniline/Prussian blue electrochromic devices containing an ionic liquid based gel electrolyte film". *Physical Chemistry Chemical Physics*, 11(27), 5674–5685.

Dei, A., Gatteschi, D., Sangregorio, C., and Sorace, L. (2004). "Quinonoid Metal Complexes: Toward Molecular Switches". *Accounts of chemical research*, 37(11), 827–835.

Delmonte, D., Mezzadri, F., Orlandi, F., Calestani, G., Amiel, Y., and Gilioli, E. (2018). "High Pressure Induced Insulator-to-Semimetal Transition through Intersite Charge Transfer in $NaMn_7O_{12}$". *Crystals*, 8(2), 81.

Demir, S., Zadrozny, J. M., Nippe, M., and Long, J. R. (2012). "Exchange Coupling and Magnetic Blocking in Bipyrimidyl Radical-Bridged Dilanthanide Complexes". *Journal of the American Chemical Society*, 134(45), 18546–18549.

Deshmukh, M. M., Ohba, M., Kitagawa, S., and Sakaki, S. (2013). "Absorption of CO_2 and CS_2 into the Hofmann-Type Porous Coordination Polymer: Electrostatic versus Dispersion Interactions". *Journal of the American Chemical Society*, 135(12), 4840–4849.

Di Sante, D., Stroppa, A., Jain, P., and Picozzi, S. (2013). "Tuning the Ferroelectric Polarization in a Multiferroic Metal–Organic Framework". *Journal of the American Chemical Society*, 135(48), 18126–18130.

Dion, M., Rydberg, H., Schröder, E., Langreth, D. C., and Lundqvist, B. I. (2004). "Van der Waals Density Functional for General Geometries". *Physical Review Letters*, 92, 246401.

Dirac, P. A. (1930). "Note on Exchange Phenomena in the Thomas Atom". *Mathematical Proceedings of the Cambridge Philosophical Society*, 26(3), 376–385.

Djeghloul, F., Ibrahim, F., Cantoni, M., Bowen, M., Joly, L., Boukari, S., Ohresser, P., Bertran, F., Le Févre, P., and Thakur, P. (2013). "Direct observation of a highly spin-polarized organic spinterface at room temperature". *Scientific Reports*, 3, 1272.

Dommaschk, M., Thoms, V., Schütt, C., Näther, C., Puttreddy, R., Rissanen, K., and Herges, R. (2015). “Coordination-Induced Spin-State Switching with Nickel Chlorin and Nickel Isobacteriochlorin”. *Inorganic chemistry*, 54(19), 9390–9392.

Duan, C.-G., Jaswal, S. S., and Tsymbal, E. Y. (2006). “Predicted Magnetoelectric Effect in $\mathrm{Fe}/\mathrm{BaTiO_3}$ Multilayers: Ferroelectric Control of Magnetism”. *Physical Review Letters*, 97(4), 047201.

Duan, C. G., Velev, J. P., Sabirianov, R. F., Zhu, Z., Chu, J., Jaswal, S. S., and Tsymbal, E. Y. (2008). “Surface Magnetoelectric Effect in Ferromagnetic Metal Films”. *Physical Review Letters*, 101(13), 1–4.

Dudarev, S., Botton, G., Savrasov, S., Humphreys, C., and Sutton, A. (1998). “Electron-energy-loss spectra and the structural stability of nickel oxide: An LSDA $+$ U study”. *Physical Review B*, 57(3), 1505.

Dunbar, K. R. and Heintz, R. A. (1996). “Chemistry of Transition Metal Cyanide Compounds: Modern Perspectives”. *Progress in Inorganic Chemistry*, 283–391.

Eerenstein, W., Mathur, N., and Scott, J. F. (2006). “Multiferroic and magnetoelectric materials”. *nature*, 442(7104), 759–765.

Fechner, M., Zahn, P., Ostanin, S., Bibes, M., and Mertig, I. (2012). “Switching Magnetization by 180$^{\mathrm{o}}$ with an Electric Field”. *Physical Review Letters*, 108, 197206.

Férey, G., Mellot-Draznieks, C., Serre, C., Millange, F., Dutour, J., Surblé, S., and Margiolaki, I. (2005). “A Chromium Terephthalate-Based Solid with Unusually Large Pore Volumes and Surface Area”. *Science*, 309(5743), 2040–2042.

Ferlay, S., Mallah, T., Ouahes, R., Veillet, P., and Verdaguer, M. (1995). “A room-temperature organometallic magnet based on Prussian blue”. *Nature*, 378(6558), 701.

Flechtner, K., Kretschmann, A., Steinrück, H.-P., and Gottfried, J. M. (2007). “NO-Induced Reversible Switching of the Electronic Interaction between a Porphyrin-

Coordinated Cobalt Ion and a Silver Surface". *Journal of American Chemical Society*, 129(40), 12110–12111.

Fong, D. D., Stephenson, G. B., Streiffer, S. K., Eastman, J. A., Aucielo, O., Fuoss, P. H., and Thompson, C. (2004). "Ferroelectricity in Ultrathin Perovskite Films". *Science*, 304(5677), 1650–1653.

Forment-Aliaga, A. and Coronado, E. (2018). "Hybrid Interfaces in Molecular Spintronics". *The Chemical Record*, 18(7-8), 737–748.

Foulkes, W., Mitas, L., Needs, R., and Rajagopal, G. (2001). "Quantum Monte Carlo simulations of solids". *Reviews of Modern Physics*, 73(1), 33.

Gambardella, P., Stepanow, S., Dmitriev, A., Honolka, J., de Groot, F. M. F., Lingenfelder, M., Gupta, S. S., Sarma, D. D., Bencok, P., Stanescu, S., Clair, S., Pons, S., Lin, N., Seitsonen, A. P., Brune, H., Barth, J. V., and Kern, K. (2009). "Supramolecular control of the magnetic anisotropy in two-dimensional high-spin Fe arrays at a metal interface". *Nature Matererials*, 8(3), 189–193.

Gamez, P., Costa, J. S., Quesada, M., and Aromí, G. (2009). "Iron Spin-Crossover compounds: from fundamental studies to practical applications". *Dalton Trans.*, 7845–7853.

Gatteschi, D., Sessoli, R., and Villain, J. (2006). *"Molecular Nanomagnets"*. Oxford University Press.

Gibson, Q. D., Manning, T. D., Zanella, M., Zhao, T., Murgatroyd, P. A., Robertson, C. M., Jones, L. A., McBride, F., Raval, R., Cora, F., et al. (2019). "Modular Design via Multiple Anion Chemistry of the High Mobility van der Waals Semiconductor $Bi_4O_4SeCl_2$". *Journal of the American Chemical Society*, 142(2), 847–856.

Girovsky, J., Nowakowski, J., Ali, M. E., Baljozovic, M., Rossmann, H. R., Nijs, T., Aeby, E. A., Nowakowska, S., Siewert, D., Srivastava, G., Wäckerlin, C., Dreiser, J., Decurtins, S., Liu, S.-X., Oppeneer, P. M., Jung, T. A., and Ballav, N. (2017). "Long-range ferrimagnetic order in a two-dimensional supramolecular Kondo lattice". *Nature Communications*, 8, 15388.

Girovsky, J., Tarafder, K., Wäckerlin, C., Nowakowski, J., Siewert, D., Hählen, T., Wäckerlin, A., Kleibert, A., Ballav, N., Jung, T. A., and Oppeneer, P. M. (2014). "Antiferromagnetic coupling of Cr-porphyrin to a bare Co substrate". *Physical Review B*, 90, 220404.

Goldschmidt, V. M. (1926). "Die Gesetze der Krystallochemie". *Naturwissenschaften*, 14(21), 477–485.

Goodenough, J. B. (1963). *"Magnetism and the chemical bond"*, 1. Interscience publishers.

Gottfried, J. M. (2015). "Surface chemistry of porphyrins and phthalocyanines". *Surface Science Reports*, 70(3), 259–379.

Gruber, M. and Berndt, R. (2016). "Manipulation of Cyclohexene-Based Organic Molecules on Various Metallic Substrates". *Journal of Physical Chemistry C*, 120(33), 18642–18650.

Guo, F.-S., Bar, A. K., and Layfield, R. A. (2019). "Main Group Chemistry at the Interface with Molecular Magnetism". *Chemical reviews*, 119(14), 8479–8505.

Gütlich, P., Garcia, Y., and Goodwin, H. A. (2000). "Spin crossover phenomena in Fe(II) complexesDedicated to Professor F. A. Cotton on occasion of his 70th birthday.". *Chemical Society Reviews*, 29(6), 419–427.

Gütlich, P., Goodwin, H. A., and Garcia, Y. (2004). *"Spin crossover in transition metal compounds I"*. Springer Science & Business Media.

Halcrow, M. A. (2013). *"Spin-Crossover Materials: Properties and Applications"*. John Wiley & Sons.

Halder, G. J., Kepert, C. J., Moubaraki, B., Murray, K. S., and Cashion, J. D. (2002). "Guest-Dependent Spin Crossover in a Nanoporous Molecular Framework Material". *Science*, 298(5599), 1762–1765.

Hamann, D., Schlüter, M., and Chiang, C. (1979). "Norm-Conserving Pseudopotentials". *Physical Review Letters*, 43(20), 1494.

Hao, H., Zheng, X., Song, L., Wang, R., and Zeng, Z. (2012). “Electrostatic Spin Crossover in a Molecular Junction of a Single-Molecule Magnet Fe_2”. *Physical Review Letters*, 108(1), 017202.

Harada, J. K., Charles, N., Poeppelmeier, K. R., and Rondinelli, J. M. (2019). “Heteroanionic Materials by Design: Progress Toward Targeted Properties”. *Advanced Materials*, 31(19), 1805295.

Hauser, A. (2004). “Ligand Field Theoretical Considerations”. In *Spin Crossover in Transition Metal Compounds I*, 49–58. Springer.

Hayward, M., Cussen, E., Claridge, J., Bieringer, M., Rosseinsky, M., Kiely, C., Blundell, S., Marshall, I., and Pratt, F. (2002). “The Hydride Anion in an Extended Transition Metal Oxide Array: $LaSrCoO_3H_{0.7}$”. *Science*, 295(5561), 1882–1884.

Hermanns, C. F., Tarafder, K., Bernien, M., Krüger, A., Chang, Y.-M., Oppeneer, P. M., and Kuch, W. (2013). “Magnetic Coupling of Porphyrin Molecules Through Graphene”. *Advanced Materials*, 25(25), 3473–3477.

Herper, H. C., Bernien, M., Bhandary, S., Hermanns, C. F., Krüger, A., Miguel, J., Weis, C., Schmitz-Antoniak, C., Krumme, B., Bovenschen, D., et al. (2013). “Iron porphyrin molecules on Cu(001): Influence of adlayers and ligands on the magnetic properties”. *Physical Review B*, 87(17), 174425.

Heyd, J., Scuseria, G. E., and Ernzerhof, M. (2003). “Hybrid functionals based on a screened Coulomb potential”. *The Journal of chemical physics*, 118(18), 8207–8215.

Hiroi, Z., Kobayashi, N., and Takano, M. (1994). “Probable hole-doped superconductivity without apical oxygens in $(\mathrm{Ca,Na})_2CuO_2CI_2$”. *Nature*, 371(6493), 139–141.

Hofmann, K. A. and Küspert, F. (1897). “Verbindungen von kohlenwasserstoffen mit metallsalzen”. *Zeitschrift für anorganische Chemie*, 15(1), 204–207.

Hogue, R. W., Singh, S., and Brooker, S. (2018). “Spin crossover in discrete polynuclear iron(II) complexes”. *Chemical Society Reviews*, 47(19), 7303–7338.

Hohenberg, P. and Kohn, W. (1964). “Inhomogeneous Electron Gas”. *Physical review*, 136(3B), B864.

Hotta, Y., Susaki, T., and Hwang, H. Y. (2007). “Polar Discontinuity Doping of the $LaVO_3/SrTiO_3$ Interface”. *Physical Review Letters*, 99, 236805.

Hu, J. M., Li, Z., Chen, L. Q., and Nan, C. W. (2011). “High-density magnetoresistive random access memory operating at ultralow voltage at room temperature”. *Nature Communications*, 2, 553.

Hu, J. M., Li, Z., Chen, L. Q., and Nan, C. W. (2012). “Design of a Voltage-Controlled Magnetic Random Access Memory Based on Anisotropic Magnetoresistance in a Single Magnetic Layer”. *Advanced Materials*, 24(21), 2869–2873.

Huang, S., Kang, D., Wu, X., Niu, J., and Qin, S. (2017). “Pressure-induced structural and spin transitions of Fe_3S_4”. *Scientific reports*, 7, 46334.

Hubbard, J. (1958). “The description of collective motions in terms of many-body perturbation theory. II. The correlation energy of a free-electron gas”. *Proceedings of the Royal Society of London. Series A. Mathematical and Physical Sciences*, 243(1234), 336–352.

Hüfner, S. (1994). “Electronic structure of NiO and related 3d-transition-metal compounds”. *Advances in Physics*, 43(2), 183–356.

Hunter, S., Davidson, A. J., Morrison, C. A., Pulham, C. R., Richardson, P., Farrow, M. J., Marshall, W. G., Lennie, A. R., and Gould, P. J. (2011). “Combined Experimental and Computational Hydrostatic Compression Study of Crystalline Ammonium Perchlorate”. *The Journal of Physical Chemistry C*, 115(38), 18782–18788.

Iacovita, C., Rastei, M. V., Heinrich, B. W., Brumme, T., Kortus, J., Limot, L., and Bucher, J. P. (2008). “Visualizing the Spin of Individual Cobalt-Phthalocyanine Molecules”. *Physical Review Letters*, 101(11), 116602.

Javaid, S., Bowen, M., Boukari, S., Joly, L., Beaufrand, J.-B., Chen, X., Dappe, Y. J., Scheurer, F., Kappler, J.-P., Arabski, J., Wulfhekel, W., Alouani, M., and Beaurepaire,

E. (2010). “Impact on Interface Spin Polarization of Molecular Bonding to Metallic Surfaces”. *Physical Review Letters*, 105, 077201.

Jones, R. O. and Gunnarsson, O. (1989). “The density functional formalism, its applications and prospects”. *Reviews of Modern Physics*, 61(3), 689.

Kar, P., Yoshida, M., Shigeta, Y., Usui, A., Kobayashi, A., Minamidate, T., Matsunaga, N., and Kato, M. (2017). “Methanol-Triggered Vapochromism Coupled with Solid-State Spin Switching in a Nickel(II)-Quinonoid Complex”. *Angewandte Chemie*, 129(9), 2385–2389.

Kaye, S. S. and Long, J. R. (2005). “Hydrogen Storage in the Dehydrated Prussian Blue Analogues $M_3[Co(CN)_6]_2$ $(M = Mn, Fe, Co, Ni, Cu, Zn)$”. *Journal of the American Chemical Society*, 127(18), 6506–6507.

Khusniyarov, M. M. (2016). “How to Switch Spin-Crossover Metal Complexes at Constant Room Temperature”. *Chemistry-A European Journal*, 22(43), 15178–15191.

Kim, S. B., Pike, R. D., and Sweigart, D. A. (2013). “Multifunctionality of Organometallic Quinonoid Metal Complexes: Surface Chemistry, Coordination Polymers, and Catalysts”. *Accounts of chemical research*, 46(11), 2485–2497.

Kitagawa, S. and Kawata, S. (2002). “Coordination compounds of 1,4-dihydroxybenzoquinone and its homologues. Structures and properties”. *Coordination chemistry reviews*, 224(1-2), 11–34.

Kitazawa, T., Gomi, Y., Takahashi, M., Takeda, M., Enomoto, M., Miyazaki, A., and Enoki, T. (1996). “Spin-crossover behaviour of the coordination polymer $Fe^{II}(C_5H_5N)_2Ni^{II}(CN)_4$”. *Journal of Materials Chemistry*, 6(1), 119–121.

Kleinman, L. and Bylander, D. (1982). “Efficacious Form for Model Pseudopotentials”. *Physical Review Letters*, 48(20), 1425.

Kobayashi, Y., Tsujimoto, Y., and Kageyama, H. (2018). “Property Engineering in Perovskites via Modification of Anion Chemistry”. *Annual Review of Materials Research*, 48, 303–326.

Kohn, W. and Sham, L. J. (1965a). "Quantum Density Oscillations in an Inhomogeneous Electron Gas". *Physical Review*, 137(6A), A1697.

Kohn, W. and Sham, L. J. (1965b). "Self-Consistent Equations Including Exchange and Correlation Effects". *Physical review*, 140(4A), A1133.

Kresse, G. and Furthmüller, J. (1996). "Efficient iterative schemes for *ab initio* total-energy calculations using a plane-wave basis set". *Physical review B*, 54(16), 11169.

Kresse, G. and Hafner, J. (1993). "*Ab initio* molecular dynamics for liquid metals". *Physical Review B*, 47(1), 558.

Kucheriv, O. I., Naumova, D. D., Tokmenko, I. I., Polunin, R. A., and Terebilenko, K. V. (2017). "Crystal structure of $\mathrm{poly[tetra}-\mu_2-\mathrm{cyanido}-1:2\kappa^8\mathrm{N}:\mathrm{C}-\mathrm{bis(dimethylsulfoxide}-1\kappa\mathrm{O)diargentate(I)iron(II)]}$". *Acta Crystallographica Section E: Crystallographic Communications*, 73(2), 270–272.

Kumar, K. S. and Ruben, M. (2017). "Emerging trends in spin crossover (SCO) based functional materials and devices". *Coordination Chemistry Reviews*, 346, 176–205.

Lach, S., Altenhof, A., Tarafder, K., Schmitt, F., Ali, M. E., Vogel, M., Sauther, J., Oppeneer, P. M., and Ziegler, C. (2012). "Metal–Organic Hybrid Interface States of A Ferromagnet/Organic Semiconductor Hybrid Junction as Basis For Engineering Spin Injection in Organic Spintronics". *Advanced Functional Materials*, 22(5), 989–997.

Larionova, J., Salmon, L., Guari, Y., Tokarev, A., Molvinger, K., Molnár, G., and Bousseksou, A. (2008). "Towards the Ultimate Size Limit of the Memory Effect in Spin-Crossover Solids". *Angewandte Chemie*, 120(43), 8360–8364.

Lebègue, S., Pillet, S., and Ángyán, J. G. (2008). "Modeling spin-crossover compounds by periodic $\mathrm{DFT}+\mathrm{U}$ approach". *Physical Review B*, 78, 024433.

Leblanc, M., Maisonneuve, V., and Tressaud, A. (2015). "Crystal Chemistry and Selected Physical Properties of Inorganic Fluorides and Oxide-Fluorides". *Chemical reviews*, 115(2), 1191–1254.

Li, H., Xu, Q., Li, N., Sun, R., Ge, J., Lu, J., Gu, H., and Yan, F. (2010). “A Small-Molecule-Based Ternary Data-Storage Device”. *Journal of the American Chemical Society*, 132(16), 5542–5543.

Li, Z.-Y., Ohtsu, H., Kojima, T., Dai, J.-W., Yoshida, T., Breedlove, B. K., Zhang, W.-X., Iguchi, H., Sato, O., Kawano, M., et al. (2016). “Direct Observation of Ordered High-Spin–Low-Spin Intermediate States of an Iron(III) Three-Step Spin-Crossover Complex”. *Angewandte Chemie*, 128(17), 5270–5275.

Liechtenstein, A., Anisimov, V., and Zaanen, J. (1995). “Density-functional theory and strong interactions: Orbital ordering in Mott-Hubbard insulators”. *Physical Review B*, 52(8), R5467.

Liu, X., Hong, R., and Tian, C. (2009). “Tolerance factor and the stability discussion of ABO_3-type ilmenite”. *Journal of Materials Science: Materials in Electronics*, 20(4), 323.

Lodi Rizzini, A., Krull, C., Balashov, T., Mugarza, A., Nistor, C., Yakhou, F., Sessi, V., Klyatskaya, S., Ruben, M., Stepanow, S., and Gambardella, P. (2012). “Exchange Biasing Single Molecule Magnets: Coupling of $TbPc_2$ to Antiferromagnetic Layers”. *Nano Letters*, 12(11), 5703–5707.

Lörtscher, E. (2013). “Wiring molecules into circuits”. *Nature nanotechnology*, 8(6), 381–384.

Lu, C., Hu, W., Tian, Y., and Wu, T. (2015). “Multiferroic oxide thin films and heterostructures”. *Applied Physics Reviews*, 2(2), 021304.

Lumetti, S., Candini, A., Godfrin, C., Balestro, F., Wernsdorfer, W., Klyatskaya, S., Ruben, M., and Affronte, M. (2016). “Single-molecule devices with graphene electrodes”. *Dalton Trans.*, 45, 16570–16574.

Ma, J., Hu, J., Li, Z., and Nan, C. W. (2011). “Recent Progress in Multiferroic Magnetoelectric Composites: from Bulk to Thin Films”. *Advanced Materials*, 23(9), 1062–1087.

Malavolti, L., Mannini, M., Car, P.-E., Campo, G., Pineider, F., and Sessoli, R. (2013). "Erratic magnetic hysteresis of $\mathrm{TbPc_2}$ molecular nanomagnets". *Journal of Materials Chemistry C*, 1(16), 2935–2942.

Maldonado, P., Kanungo, S., Saha-Dasgupta, T., and Oppeneer, P. M. (2013). "Two-step spin-switchable tetranuclear Fe(II) molecular solid: *Ab initio* theory and predictions". *Phys. Rev. B*, 88, 020408.

Mandal, B., Chung, J. S., and Kang, S. G. (2017). "Exploring the geometric, magnetic and electronic properties of Hofmann MOFs for drug delivery". *Physical Chemistry Chemical Physics*, 19(46), 31316–31324.

Mann, B. and Kuhn, H. (1971). "Tunneling through Fatty Acid Salt Monolayers". *Journal of Applied Physics*, 42(11), 4398–4405.

Mannini, M., Pineider, F., Danieli, C., Totti, F., Sorace, L., Sainctavit, P., Arrio, M.-A., Otero, E., Joly, L., Cezar, J. C., et al. (2010). "Quantum tunnelling of the magnetization in a monolayer of oriented single-molecule magnets". *Nature*, 468(7322), 417–421.

Mannini, M., Pineider, F., Sainctavit, P., Danieli, C., Otero, E., Sciancalepore, C., Talarico, A. M., Arrio, M.-A., Cornia, A., Gatteschi, D., et al. (2009). "Magnetic memory of a single-molecule quantum magnet wired to a gold surface". *Nature materials*, 8(3), 194–197.

Manriquez, J. M., Yee, G. T., McLean, R. S., Epstein, A. J., and Miller, J. S. (1991). "A Room-Temperature Molecular/Organic-Based Magnet". *Science*, 252(5011), 1415–1417.

Martin, R. M. (2004). *"Electronic Structure: Basic Theory and Practical Methods"*. Cambridge University Press.

Maruyama, T., Shiota, Y., Nozaki, T., Ohta, K., Toda, N., Mizuguchi, M., Tulapurkar, A. A., Shinjo, T., Shiraishi, M., Mizukami, S., Ando, Y., and Suzuki, Y. (2009). "Large voltage-induced magnetic anisotropy change in a few atomic layers of iron". *Nature Nanotechnology*, 4(3), 158–161.

McConnell, H. M. (1963). “Ferromagnetism in Solid Free Radicals”. *The Journal of Chemical Physics*, 39(7), 1910–1910.

Megaw, H. D. (1962). “Refinement of the structure of $BaTiO_3$ and other ferroelectrics”. *Acta Crystallographica*, 15(10), 972–973.

Mikolasek, M., Manrique-Juarez, M. D., Shepherd, H. J., Ridier, K., Rat, S., Shalabaeva, V., Bas, A.-C., Collings, I. E., Mathieu, F., and Cacheux, J. (2018). “Complete Set of Elastic Moduli of a Spin-Crossover Solid: Spin-State Dependence and Mechanical Actuation”. *Journal of the American Chemical Society*, 140(28), 8970–8979.

Miller, J. S., Epstein, A. J., and Reiff, W. M. (1988). “Ferromagnetic molecular charge-transfer complexes”. *Chemical Reviews*, 88(1), 201–220.

Miller, J. S. and Gatteschi, D. (2011). “Molecule-based magnets”. *Chemical Society Reviews*, 40(6), 3065–3066.

Miller, J. S., Vazquez, C., McLean, R. S., Reiff, W. M., Aumüller, A., and Hünig, S. (1993). “Ferromagnetically coupled decamethylmetallocenium salts of 2,5-dimethyl-N,N’-dicyanoquinonediimine, $[M(C_5Me_5)_2]^{\oplus}[Me_2DCNQI]^{\odot\ominus}, (M = Fe, Mn)$”. *Advanced Materials*, 5(6), 448–450.

Mitchell, R. H. (2002). *“Perovskites: modern and ancient”*. Almaz Press.

Molnár, G., Rat, S., Salmon, L., Nicolazzi, W., and Bousseksou, A. (2018). “Spin Crossover Nanomaterials: From Fundamental Concepts to Devices”. *Advanced Materials*, 30(5), 1703862.

Molnár, G., Salmon, L., Nicolazzi, W., Terki, F., and Bousseksou, A. (2014). “Emerging properties and applications of spin crossover nanomaterials”. *Journal of Materials Chemistry C*, 2(8), 1360–1366.

Moodera, J. S., Koopmans, B., and Oppeneer, P. M. (2014). “On the path toward organic spintronics”. *MRS Bulletin*, 39(7), 578–581.

Moritomo, Y., Akimoto, T., Takeo, M., Machida, A., Nishibori, E., Takata, M., Sakata, M., Ohoyama, K., and Nakamura, A. (2000). "Metal-insulator transition induced by a spin-state transition in $\mathrm{TbBaCo_2O_{5+\delta}}(\delta = 0.5)$". *Physical Review B*, 61(20), R13325–R13328.

Moritomo, Y., Asamitsu, A., Kuwahara, H., and Tokura, Y. (1996). "Giant magnetoresistance of manganese oxides with a layered perovskite structure". *Nature*, 380(6570), 141–144.

Mott, N. F. (1936). "The electrical conductivity of transition metals". *Proceedings of the Royal Society of London. Series A-Mathematical and Physical Sciences*, 153(880), 699–717.

Mukherjee, S., Keitany, G., Li, Y., Wang, Y., Ball, H. L., Goldsmith, E. J., and Orth, K. (2006). "Yersinia YopJ Acetylates and Inhibits Kinase Activation by Blocking Phosphorylation". *Science*, 312(5777), 1211–1214.

Murphy, M. J., Zenere, K. A., Ragon, F., Southon, P. D., Kepert, C. J., and Neville, S. M. (2017). "Guest Programmable Multistep Spin Crossover in a Porous $2-\mathrm{D}$ Hofmann-Type Material". *Journal of the American Chemical Society*, 139(3), 1330–1335.

Ni, Z.-P., Liu, J.-L., Hoque, M. N., Liu, W., Li, J.-Y., Chen, Y.-C., and Tong, M.-L. (2017). "Recent advances in guest effects on spin-crossover behavior in Hofmann-type metal-organic frameworks". *Coordination Chemistry Reviews*, 335, 28–43.

Niel, V., Martinez-Agudo, J. M., Munoz, M. C., Gaspar, A. B., and Real, J. A. (2001). "Cooperative Spin Crossover Behavior in Cyanide-Bridged Fe(II)-M(II) Bimetallic 3D Hofmann-like Networks (M = Ni, Pd, and Pt)". *Inorganic chemistry*, 40(16), 3838–3839.

Niranjan, M. K., Burton, J. D., Velev, J. P., Jaswal, S., and Tsymbal, E. Y. (2009). "Magnetoelectric effect at the $\mathrm{SrRuO_3/BaTiO_3}$ (001) interface: An *ab initio* study". *Applied Physics Letters*, 95(5), 052501.

Niranjan, M. K., Velev, J. P., Duan, C.-G., Jaswal, S. S., and Tsymbal, E. Y. (2008). "Magnetoelectric effect at the $Fe_3O_4/BaTiO_3$ (001) interface: A first-principles study". *Physical Review B*, 78, 104405.

O'Grady, K. and Laidler, H. (1999). "The limits to magnetic recording — media considerations". *Journal of Magnetism and Magnetic Materials*, 200(1-3), 616–633.

Ohba, M., Yoneda, K., Agustí, G., Munoz, M. C., Gaspar, A. B., Real, J. A., Yamasaki, M., Ando, H., Nakao, Y., and Sakaki, S. (2009). "Bidirectional Chemo-Switching of Spin State in a Microporous Framework". *Angewandte Chemie*, 121(26), 4861–4865.

Ohkoshi, S.-i., Imoto, K., Tsunobuchi, Y., Takano, S., and Tokoro, H. (2011). "Light-induced spin-crossover magnet". *Nature chemistry*, 3(7), 564–569.

Ohtani, R., Yoneda, K., Furukawa, S., Horike, N., Kitagawa, S., Gaspar, A. B., Munoz, M. C., Real, J. A., and Ohba, M. (2011). "Precise Control and Consecutive Modulation of Spin Transition Temperature Using Chemical Migration in Porous Coordination Polymers". *Journal of the American Chemical Society*, 133(22), 8600–8605.

Okamura, T., Wu, B., Iguchi, H., Breedlove, B. K., Yamashita, M., Kosaka, W., Miyasaka, H., and Takaishi, S. (2017). "Three dimensional porous Hofmannclathrate$[M^{II}Pt^{II}(CN)_4]_\infty(M = Co, Ni)$ synthesized by using postsynthetic reductive elimination". *Chemical Communications*, 53(48), 6512–6515.

Oppeneer, P., Panchmatia, P., Sanyal, B., Eriksson, O., and Ali, M. (2009). "Nature of the magnetic interaction between Fe-porphyrin molecules and ferromagnetic surfaces". *Progress in Surface Science*, 84(1), 18 – 29.

Ou, X., Fan, F., Li, Z., Wang, H., and Wu, H. (2016a). "Spin-state transition induced half metallicity in a cobaltate from first principles". *Applied Physics Letters*, 108(9), 1–5.

Ou, X., Fan, F., Li, Z., Wang, H., and Wu, H. (2016b). "Spin-state transition induced half metallicity in a cobaltate from first principles". *Applied Physics Letters*, 108(9), 092402.

Panchmatia, P. M., Ali, M. E., Sanyal, B., and Oppeneer, P. M. (2010). "Halide Ligated Iron Porphines: A DFT + U and UB3LYP Study". *The Journal of Physical Chemistry A*, 114(51), 13381–13387.

Parkin, S., Roche, K., and Suzuki, T. (1992). "Giant Magnetoresistance in Antiferromagnetic Co/Cu Multilayers Grown on Kapton". *Japanese journal of applied physics*, 31(9A), L1246.

Pascal, S. and Siri, O. (2017). "Benzoquinonediimine ligands: Synthesis, coordination chemistry and properties". *Coordination Chemistry Reviews*, 350, 178–195.

Payne, M. C., Teter, M. P., Allan, D. C., Arias, T., and Joannopoulos, a. J. (1992). "Iterative minimization techniques for *ab initio* total-energy calculations: molecular dynamics and conjugate gradients". *Reviews of modern physics*, 64(4), 1045.

Pemmaraju, C., Rungger, I., and Sanvito, S. (2009). "*Ab initio* calculation of the bias-dependent transport properties of Mn_{12} molecules". *Physical Review B*, 80(10), 104422.

Pena, M. and Fierro, J. (2001). "Chemical Structures and Performance of Perovskite Oxides". *Chemical reviews*, 101(7), 1981–2018.

Peng, Y.-Y., Wu, S.-G., Chen, Y.-C., Liu, W., Huang, G.-Z., Ni, Z.-P., and Tong, M.-L. (2020). "Asymmetric seven-/eight-step spin-crossover in a three-dimensional Hofmann-type metal-organic framework". *Inorganic Chemistry Frontiers*, 7(8), 1685–1690.

Perdew, J. P., Burke, K., and Ernzerhof, M. (1996). "Generalized Gradient Approximation Made Simple". *Physical review letters*, 77(18), 3865.

Perdew, J. P., Chevary, J. A., Vosko, S. H., Jackson, K. A., Pederson, M. R., Singh, D. J., and Fiolhais, C. (1992). "Atoms, molecules, solids, and surfaces: Applications of the generalized gradient approximation for exchange and correlation". *Physical review B*, 46(11), 6671.

Perdew, J. P. and Zunger, A. (1981). “Self-interaction correction to density-functional approximations for many-electron systems”. *Physical Review B*, 23(10), 5048.

Perrin, M. L., Verzijl, C. J., Martin, C. A., Shaikh, A. J., Eelkema, R., Van Esch, J. H., Van Ruitenbeek, J. M., Thijssen, J. M., Van Der Zant, H. S., and Dulić, D. (2013). “Large tunable image-charge effects in single-molecule junctions”. *Nature nanotechnology*, 8(4), 282–287.

Phillips, J. C. (1958). “Energy-band interpolation scheme based on a pseudopotential”. *Physical Review*, 112(3), 685.

Phillips, J. C. and Kleinman, L. (1959). “New Method for Calculating Wave Functions in Crystals and Molecules”. *Physical Review*, 116(2), 287.

Phonsri, W., Lewis, B. A., Jameson, G. N., and Murray, K. S. (2019). “Double spin crossovers: a new double salt strategy to improve magnetic and memory properties”. *Chemical Communications*, 55(93), 14031–14034.

Pickett, W. E. (1989). “Pseudopotential methods in condensed matter applications”. *Computer Physics Reports*, 9(3), 115–197.

Polyzou, C. D. and Tangoulis, V. (2019). “Downsizing effect on 2-D and 3-D spin crossover metal-organic frameworks”. *Journal of Coordination Chemistry*, 72(3), 389–418.

Radaelli, G., Petti, D., Plekhanov, E., Fina, I., Torelli, P., Salles, B., Cantoni, M., Rinaldi, C., Gutiérrez, D., Panaccione, G., Varela, M., Picozzi, S., Fontcuberta, J., and Bertacco, R. (2014). “Electric control of magnetism at the Fe/$BaTiO_3$ interface”. *Nature communications*, 5, 3404.

Raman, K. V., Kamerbeek, A. M., Mukherjee, A., Atodiresei, N., Sen, T. K., Lazić, P., Caciuc, V., Michel, R., Stalke, D., Mandal, S. K., Blügel, S., Münzenberg, M., and Moodera, J. S. (2013). “Interface-engineered templates for molecular spin memory devices”. *Nature*, 493(7433), 509–513.

Reddy, I. R., Oppeneer, P. M., and Tarafder, K. (2018). “Route to achieving giant magnetoelectric coupling in $BaTiO_3/Sr_2CoO_3F$ perovskite heterostructures”. *Physical Review B*, 98(14), 140401.

Reddy, I. R., Oppeneer, P. M., and Tarafder, K. (2019). “Interfacial Spin Manipulation of Nickel-Quinonoid Complex Adsorbed on Co(001) Substrate”. *Magnetochemistry*, 5(1), 2.

Reddy, I. R. and Tarfder, K. (2020). “Theoretical Investigations of Electronic Structure and Magnetic and Optical Properties of Transition-Metal Dinuclear Molecules”. *ACS Omega*, 5(38), 24520–24525.

Rocha, A. R., Garcia-Suarez, V. M., Bailey, S. W., Lambert, C. J., Ferrer, J., and Sanvito, S. (2005). “Towards molecular spintronics”. *Nature materials*, 4(4), 335–339.

Rondinelli, J. M., Stengel, M., and Spaldin, N. A. (2008). “Carrier-mediated magnetoelectricity in complex oxide heterostructures”. *Nature nanotechnology*, 3(1), 46.

Saha-Dasgupta, T. and Oppeneer, P. M. (2014). “Computational design of magnetic metal-organic complexes and coordination polymers with spin-switchable functionalities”. *MRS bulletin*, 39(7), 614–620.

Sanvito, S. (2010). “Molecular spintronics: The rise of spinterface science”. *Nature Physics*, 6, 562–564.

Sanvito, S. (2011). “Molecular spintronics”. *Chemical Society Reviews*, 40(6), 3336–3355.

Sarkar, S., Tarafder, K., Oppeneer, P. M., and Saha-Dasgupta, T. (2011). “Spin-crossover in cyanide-based bimetallic coordination polymers—insight from first-principles calculations”. *Journal of Materials Chemistry*, 21(36), 13832–13840.

Sato, O. (2016). “Dynamic molecular crystals with switchable physical properties”. *Nature chemistry*, 8(7), 644.

Sato, O., Iyoda, T., Fujishima, A., and Hashimoto, K. (1996). “Photoinduced Magnetization of a Cobalt-Iron Cyanide”. *Science*, 272(5262), 704–705.

Scheybal, A., Ramsvik, T., Bertschinger, R., Putero, M., Nolting, F., and Jung, T. (2005). "Induced magnetic ordering in a molecular monolayer". *Chemical physics letters*, 411(1), 214–220.

Sciortino, N. F., Ragon, F., Zenere, K. A., Southon, P. D., Halder, G. J., Chapman, K. W., Piñeiro López, L., Real, J. A., Kepert, C. J., and Neville, S. M. (2016). "Exploiting Pressure To Induce a "Guest-Blocked" Spin Transition in a Framework Material". *Inorganic chemistry*, 55(20), 10490–10498.

Scott, J. F. (2007). "Applications of Modern Ferroelectrics". *Science*, 315(5814), 954–959.

Scott, J. F. (2012). "Applications of magnetoelectrics". *Journal of Materials Chemistry*, 22(11), 4567.

Scott, J. F. (2013). "Room-temperature multiferroic magnetoelectrics". *NPG Asia Materials*, 5(10), e72–11.

Shekar, N. C., Sahu, P. C., Sekar, M., Yousuf, M., and Rajan, K. G. (1996). "Pressure induced isostructural and structural transitions in $ThAl_2$". *Physica B: Condensed Matter*, 228(3-4), 369–373.

Shi, Y. and Falk, M. L. (2007). "Stress-induced structural transformation and shear banding during simulated nanoindentation of a metallic glass". *Acta materialia*, 55(13), 4317–4324.

Shin, Y. J., Kim, Y., Kang, S.-J., Nahm, H.-H., Murugavel, P., Kim, J. R., Cho, M. R., Wang, L., Yang, S. M., Yoon, J.-G., et al. (2017). "Interface Control of Ferroelectricity in an $SrRuO_3/BaTiO_3/SrRuO_3$ Capacitor and its Critical Thickness". *Advanced Materials*, 29(19), 1602795.

Siegmann, H. (1992). "Surface and 2D magnetism". *Journal of Physics: Condensed Matter*, 4(44), 8395.

Slater, J. C. (1951). "A Simplification of the Hartree-Fock Method". *Physical review*, 81(3), 385.

Solomatova, N. V., Jackson, J. M., Sturhahn, W., Wicks, J. K., Zhao, J., Toellner, T. S., Kalkan, B., and Steinhardt, W. M. (2016). “Equation of state and spin crossover of (Mg,Fe)O at high pressure, with implications for explaining topographic relief at the core-mantle boundary”. *American Mineralogist*, 101(5), 1084–1093.

Solovyev, I., Dederichs, P., and Anisimov, V. (1994). “Corrected atomic limit in the local-density approximation and the electronic structure of *d* impurities in Rb”. *Physical Review B*, 50(23), 16861.

Steil, S., Großmann, N., Laux, M., Ruffing, A., Steil, D., Wiesenmayer, M., Mathias, S., Monti, O. L. A., Cinchetti, M., and Aeschlimann, M. (2013). “Spin-dependent trapping of electrons at spinterfaces”. *Nature Physics*, 9(4), 242–247.

Stepanow, S., Mugarza, A., Ceballos, G., Moras, P., Cezar, J., Carbone, C., and Gambardella, P. (2010). “Giant spin and orbital moment anisotropies of a Cu-phthalocyanine monolayer”. *Physical Review B*, 82(1), 014405.

Stöhr, J. (1995). “X-ray magnetic circular dichroism spectroscopy of transition metal thin films”. *Journal of Electron Spectroscopy and Related Phenomena*, 75, 253–272.

Stöhr, J. (1999). “Exploring the microscopic origin of magnetic anisotropies with X-ray magnetic circular dichroism (XMCD) spectroscopy”. *Journal of Magnetism and Magnetic Materials*, 200(1-3), 470–497.

Stöhr, J. and König, H. (1995). “Determination of Spin- and Orbital-Moment Anisotropies in Transition Metals by Angle-Dependent X-Ray Magnetic Circular Dichroism”. *Physical review letters*, 75(20), 3748.

Stroppa, A., Barone, P., Jain, P., Perez-Mato, J., and Picozzi, S. (2013). “Hybrid Improper Ferroelectricity in a Multiferroic and Magnetoelectric Metal-Organic Framework”. *Advanced Materials*, 25(16), 2284–2290.

Stroppa, A., Jain, P., Barone, P., Marsman, M., Perez-Mato, J. M., Cheetham, A. K., Kroto, H. W., and Picozzi, S. (2011). “Electric Control of Magnetization and Interplay between Orbital Ordering and Ferroelectricity in a Multiferroic Metal–Organic Framework”. *Angewandte Chemie International Edition*, 50(26), 5847–5850.

Sun, L., Diaz-Fernandez, Y. A., Gschneidtner, T. A., Westerlund, F., Lara-Avila, S., and Moth-Poulsen, K. (2014). “Single-molecule electronics: from chemical design to functional devices”. *Chemical Society Reviews*, 43(21), 7378–7411.

Suraj, T. S., Omar, G. J., Jani, H., Juvaid, M. M., Hooda, S., Chaudhuri, A., Rusydi, A., Sethupathi, K., Venkatesan, T., Ariando, A., and Rao, M. S. R. (2020). “Tunable and enhanced Rashba spin-orbit coupling in iridate-manganite heterostructures”. *Phys. Rev. B*, 102, 125145.

Tan, J. C. and Cheetham, A. K. (2011). “Mechanical properties of hybrid inorganic–organic framework materials: establishing fundamental structure–property relationships”. *Chemical Society Reviews*, 40(2), 1059–1080.

Tao, L. L. and Wang, J. (2017). “Giant magnetoresistance and perfect spin filter effects in manganese phthalocyanine based molecular junctions”. *Nanoscale*, 9(34), 12684–12689.

Tarafder, K., Kanungo, S., Oppeneer, P. M., and Saha-Dasgupta, T. (2012). “Pressure and Temperature Control of Spin-Switchable Metal-Organic Coordination Polymers from *Ab Initio* Calculations”. *Physical review letters*, 109(7), 077203.

Tassel, C., Goto, Y., Kuno, Y., Hester, J., Green, M., Kobayashi, Y., and Kageyama, H. (2014). “Direct Synthesis of Chromium Perovskite Oxyhydride with a High Magnetic-Transition Temperature”. *Angewandte Chemie International Edition*, 53(39), 10377–10380.

Tassel, C., Kuno, Y., Goto, Y., Yamamoto, T., Brown, C. M., Hester, J., Fujita, K., Higashi, M., Abe, R., Tanaka, K., et al. (2015). “$\mathrm{MnTaO_2N}$:$\mathrm{PolarLiNbO_3} - type$OxynitridewithaHelicalSpinOrder”. *Angewandte Chemie International Edition*, 54(2), 516–521.

Terakura, K., Oguchi, T., Williams, A., and Kübler, J. (1984a). “Band theory of insulating transition-metal monoxides: Band-structure calculations”. *Physical Review B*, 30(8), 4734.

Terakura, K., Williams, A., Oguchi, T., and Kübler, J. (1984b). "Transition-Metal Monoxides: Band or Mott Insulators". *Physical review letters*, 52(20), 1830.

Tiana, D., Hendon, C. H., and Walsh, A. (2014). "Ligand design for long-range magnetic order in metal–organic frameworks". *Chemical Communications*, 50(90), 13990–13993.

Tkatchenko, A. and Scheffler, M. (2009). "Accurate Molecular Van Der Waals Interactions from Ground-State Electron Density and Free-Atom Reference Data". *Physical Review Letters*, 102, 073005.

Tokura, Y. and Nagaosa, N. (2000). "Orbital Physics in Transition-Metal Oxides". *science*, 288(5465), 462–468.

Torad, N. L., Hu, M., Imura, M., Naito, M., and Yamauchi, Y. (2012). "Large Cs adsorption capability of nanostructured Prussian Blue particles with high accessible surface areas". *Journal of Materials Chemistry*, 22(35), 18261–18267.

Trassin, M. (2015). "Low energy consumption spintronics using multiferroic heterostructures". *Journal of Physics Condensed Matter*, 28(3), 33001.

Troiani, F. and Affronte, M. (2011). "Molecular spins for quantum information technologies". *Chemical Society Reviews*, 40(6), 3119–3129.

Tsujimoto, Y., Nakano, S., Ishimatsu, N., Mizumaki, M., Kawamura, N., Kawakami, T., Matsushita, Y., and Yamaura, K. (2016). "Pressure-Driven Spin Crossover Involving Polyhedral Transformation in Layered Perovskite Cobalt Oxyfluoride". *Scientific Reports*, 6(August), 1–2.

Tsujimoto, Y., Sathish, C. I., Hong, K.-P., Oka, K., Azuma, M., Guo, Y., Matsushita, Y., Yamaura, K., and Takayama-Muromachi, E. (2012a). "Crystal Structural, Magnetic, and Transport Properties of Layered Cobalt Oxyfluorides", $\mathrm{Sr_2CoO_{3+x}F_{1-x}}(0 \leq \mathrm{x} \leq 0.15)$. *Inorganic chemistry*, 51(8), 4802–4809.

Tsujimoto, Y., Yamaura, K., and Takayama-Muromachi, E. (2012b). "Oxyfluoride Chemistry of Layered Perovskite Compounds". *Applied Sciences*, 2(1), 206–219.

Valverde-Muñnoz, F. J., Seredyuk, M., Muñoz, M. C., Znovjyak, K., Fritsky, I. O., and Real, J. A. (2016). “Strong Cooperative Spin Crossover in 2D and 3D $\mathrm{Fe^{II}}$ – $\mathrm{M^{I,II}}$ Hofmann-Like Coordination Polymers Based on 2-Fluoropyrazine”. *Inorganic chemistry*, 55(20), 10654–10665.

Vaz, C. A. F., Hoffman, J., Ahn, C. H., and Ramesh, R. (2010). “Magnetoelectric Coupling Effects in Multiferroic Complex Oxide Composite Structures”. *Advanced Materials*, 22(26-27), 2900–2918.

Vázquez, H., Oszwaldowski, R., Pou, P., Ortega, J., Pérez, R., Flores, F., and Kahn, A. (2004). “Dipole formation at metal/PTCDA interfaces: Role of the Charge Neutrality Level”. *EPL (Europhysics Letters)*, 65(6), 802.

Verdaguer, M. (1996). “Molecular Electronics Emerges from Molecular Magnetism”. *Science*, 272(5262), 698.

Verdaguer, M. and Robert, V. (2013). “Fundamentals, Principles, and Concepts of Molecular Magnetism and Spintronics”. *Comprehensive Inorganic Chemistry II: From Elements to Applications*, 8, 131–189.

Vinzelberg, H., Schumann, J., Elefant, D., Gangineni, R., Thomas, J., and Büchner, B. (2008). “Low temperature tunneling magnetoresistance on $\mathrm{(La,Sr)MnO_3/Co}$ junctions with organic spacer layers”. *Journal of Applied Physics*, 103(9), 093720.

VlaŠín, O., Jarrier, R., Arras, R., Calmels, L., Warot-Fonrose, B., Marcelot, C., Jamet, M., Ohresser, P., Scheurer, F., Hertel, R., et al. (2016). “Interface Magnetoelectric Coupling in $\mathrm{Co/Pb(Zr,Ti)O_3}$”. *ACS applied materials & interfaces*, 8(11), 7553–7563.

Vogt, T., Woodward, P. M., Karen, P., Hunter, B. A., Henning, P., and Moodenbaugh, A. R. (2000). “Low to High Spin-State Transition Induced by Charge Ordering in Antiferromagnetic $\mathrm{YBaCo_2O_5}$”. *Physical Review Letters*, 84, 2969–2972.

von Barth, U. and Hedin, L. (1972). “A local exchange-correlation potential for the spin polarized case. i”. *Journal of Physics C: Solid State Physics*, 5(13), 1629.

Vosko, S. H., Wilk, L., and Nusair, M. (1980). “Accurate spin-dependent electron liquid correlation energies for local spin density calculations: a critical analysis”. *Canadian Journal of physics*, 58(8), 1200–1211.

Wäckerlin, C., Chylarecka, D., Kleibert, A., Müller, K., Iacovita, C., Nolting, F., Jung, T. A., and Ballav, N. (2010). “Controlling spins in adsorbed molecules by a chemical switch”. *Nature communications*, 1, 61.

Wäckerlin, C., Tarafder, K., Girovsky, J., Nowakowski, J., Hählen, T., Shchyrba, A., Siewert, D., Kleibert, A., Nolting, F., Oppeneer, P. M., Jung, T. A., and Ballav, N. (2013). “Ammonia Coordination Introducing a Magnetic Moment in an On-Surface Low-Spin Porphyrin”. *Angewandte Chemie Int. Ed.*, 125(17), 4666–4669.

Wäckerlin, C., Tarafder, K., Siewert, D., Girovsky, J., Hählen, T., Iacovita, C., Kleibert, A., Nolting, F., Jung, T. A., Oppeneer, P. M., and Ballav, N. (2012). “On-surface coordination chemistry of planar molecular spin systems: novel magnetochemical effects induced by axial ligands”. *Chemical Science*, 3(11), 3154–3160.

Wang, C.-C., Ke, S.-Y., Chen, K.-T., Sun, N.-K., Liu, W.-F., Ho, M.-L., Lu, B.-J., Hsieh, Y.-T., Chuang, Y.-C., and Lee, G.-H. (2018a). “Sponge-Like Water De-/Ad-Sorption versus Solid-State Structural Transformation and Colour-Changing Behavior of an Entangled 3D Composite Supramolecuar Architecture, $[\mathrm{Ni_4(dpe)_4(btc)_2(Hbtc)(H_2O)_9}]\cdot3\mathrm{H_2O}$”. *Polymers*, 10(9), 1014.

Wang, D.-s., Wu, R., and Freeman, A. J. (1993). “Magnetocrystalline anisotropy of Co-Pd interfaces”. *Physical Review B*, 48(21), 15886.

Wang, J. J., Meng, F. Y., Ma, X. Q., Xu, M. X., and Chen, L. Q. (2010). “Lattice, elastic, polarization, and electrostrictive properties of $\mathrm{BaTiO_3}$ from first-principles”. *Journal of Applied Physics*, 108(3), 0–6.

Wang, Y., Li, J., and Viehland, D. (2014). “Magnetoelectrics for magnetic sensor applications: status, challenges and perspectives”. *Materials Today*, 17(6), 269–275.

Wang, Y., Ying, J., Zhou, Z., Sun, J., Wen, T., Zhou, Y., Li, N., Zhang, Q., Han, F., and Xiao, Y. (2018b). “Emergent superconductivity in an iron-based honeycomb lattice initiated by pressure-driven spin-crossover”. *Nature communications*, 9, 1914.

Wang, Y., Zhou, Z., Wen, T., Zhou, Y., Li, N., Han, F., Xiao, Y., Chow, P., Sun, J., and Pravica, M. (2016). “Pressure-Driven Cooperative Spin-Crossover, Large-Volume Collapse, and Semiconductor-to-Metal Transition in Manganese(II) Honeycomb Lattices”. *Journal of the American Chemical Society*, 138(48), 15751–15757.

Ward, M. D. (1996). “A Dinuclear Ruthenium(II) Complex with the Dianion of 2,5-Dihydroxy-1,4-benzoquinone as Bridging Ligand. Redox, Spectroscopic, and Mixed-Valence Properties”. *Inorganic chemistry*, 35(6), 1712–1714.

Wende, H., Bernien, M., Luo, J., Sorg, C., Ponpandian, N., Kurde, J., Miguel, J., Piantek, M., Xu, X., Eckhold, Ph. Kuch, W., Baberschke, K., Panchmatia, P. M., Sanyal, B., Oppeneer, P. M., and Eriksson, O. (2007). “Substrate-induced magnetic ordering and switching of iron porphyrin molecules”. *Nature Materials*, 6(7), 516.

Wenk, H.-R. and Bulakh, A. (2016). *“Minerals: Their Constitution and Origin”*. Cambridge University Press.

Wolf, S., Awschalom, D., Buhrman, R., Daughton, J., Von Molnar, S., Roukes, M., Chtchelkanova, A. Y., and Treger, D. (2001). “Spintronics: A Spin-Based Electronics Vision for the Future”. *Science*, 294(5546), 1488–1495.

Wu, H. (2012). “Metal-insulator transition in $Sr_{2-x}La_xCoO_4$ driven by spin-state transition”. *Physical Review B - Condensed Matter and Materials Physics*, 86(7), 3–6.

Xia, H., Ruoff, A. L., and Vohra, Y. K. (1991). “Temperature dependence of the ω-bcc phase transition in zirconium metal”. *Physical Review B*, 44(18), 10374.

Xiao, W., Tan, D., Xiong, X., Liu, J., and Xu, J. (2010). “Large volume collapse observed in the phase transition in cubic $PbCrO_3$ perovskite”. *Proceedings of the National Academy of Sciences*, 107(32), 14026–14029.

Zavaliche, F., Zheng, H., Mohaddes-Ardabili, L., Yang, S., Zhan, Q., Shafer, P., Reilly, E., Chopdekar, R., Jia, Y., Wright, P., et al. (2005). “Electric field-induced magnetization switching in epitaxial columnar nanostructures”. *Nano letters*, 5(9), 1793–1796.

Zenere, K. A., Duyker, S. G., Trzop, E., Collet, E., Chan, B., Doheny, P. W., Kepert, C. J., and Neville, S. M. (2018). “Increasing spin crossover cooperativity in 2D Hofmann-type materials with guest molecule removal”. *Chemical science*, 9(25), 5623–5629.

Zhang, C.-J., Lian, K.-T., Wu, S.-G., Liu, Y., Huang, G.-Z., Ni, Z.-P., and Tong, M.-L. (2020). “The substituent guest effect on four-step spin-crossover behavior”. *Inorganic Chemistry Frontiers*, 7, 911–917.

Zhang, R. F., Legut, D., Niewa, R., Argon, A. S., and Veprek, S. (2010). “Shear-induced structural transformation and plasticity in ultraincompressible ReB_2 limit its hardness”. *Physical Review B*, 82(10), 104104.

Zhou, H.-C. and Kitagawa, S. (2014). “Metal-Organic Frameworks (MOFs)”. *Chemical Society Reviews*, 43, 5415–5418.

Zhou, H.-C., Long, J. R., and Yaghi, O. M. (2012). “Introduction to Metal–Organic Frameworks”. *Chemical Reviews*, 112(2), 673–674.

Zubko, P., Gariglio, S., Gabay, M., Ghosez, P., and Triscone, J.-M. (2011). “Interface Physics in Complex Oxide Heterostructures”. *Annual Review of Condensed Matter Physics*, 2(1), 141–165.

Žutić, I., Fabian, J., and Sarma, S. D. (2004). “Spintronics: Fundamentals and applications”. *Reviews of modern physics*, 76(2), 323.

LIST OF PUBLICATIONS BASED ON THESIS:

- Indukuru Ramesh Reddy, Peter M. Oppeneer, and Kartick Tarafder "Route to achieving giant magnetoelectric coupling in $BaTiO_3/Sr_2CoO_3F$ perovskite heterostructures" *Physical Review B* (2018) 98, 140401.
- Indukuru Ramesh Reddy, Peter M. Oppeneer, and Kartick Tarafder "Interfacial Spin Manipulation of Nickel-Quinonoid Complex Adsorbed on Co(001) Substrate" *Magnetochemistry* (2019) 5(1), 2.
- Indukuru Ramesh Reddy and Kartick Tarafder "Theoretical Investigations of Electronic Structure, Magnetic and Optical Properties of Transition Metal-dinuclear Molecules" *ACS Omega* (2020) 5(38), 24520–24525.
- Indukuru Ramesh Reddy, Peter M. Oppeneer, and Kartick Tarafder "Pressure driven spin-state and structural transformation in a Hofmann clathrate coordiantion polymer" *Journal of Magnetism and Magnetic Materials* (2021) 524, 167637.
- Indukuru Ramesh Reddy and Kartick Tarafder "Unprecedented Magnetic Interaction of Chemisorbed Ni^{II}-Dinuclear Quinonoid Molecule on a Co(001) Substrate" *(Under Review).*

Conference Presentations

- "Spin State Manipulation of Nickel Quinonoid by Chemisorbed to a Co(001) Substrate" in Theory Meets Experiment in Low-Dimensional Structures with Correlated Electrons, July 1-4, 2019 at Prague, Czech Republic. **(Contributed talk)**
- "Pressure driven structural transformation associated with spin-state switching in a Hofmann clathrate" in Spins in Molecular System: Experiment, Theory and Applications (SiM-2019), December 2-4, 2019 at Indian Institute of Science, Bangalore, India. **(Flash talk)**
- "Magnetoelectric Coupling in Barium Titanate/Cobalt oxyhalide heterostructure" in 30th Annual General Meeting of MRSI and the First Indian Materials Con-

clave, February 12-15, 2019 at Indian Institute of Science, Bangalore, India. **(Poster presentation)**

I. Ramesh Reddy

Curriculum Vitae

Door No:65/84 Veligallu (Kaspa)
Galiveedu (M), Kadapa (District)
Andhra Pradesh, India-516267
+91 7382268487
☎ *+91 9591208403*
✉ *reddy.indukururameshreddy@gmail.com*

Personal

Date of Birth	05 July 1993
Gender	Male
Place of Birth	Rayachoty, Andhra Pradesh
Languages	English, Hindi, Telugu, Kannada
Nationality	Indian

Education

2016–	**Ph.D., Physics**, *National Institute of Technology Karnataka*, .
2014–2016	**M.Sc**, *Central University of Karnataka*, Kalaburagi, *77.00%*. Distinction: Physics
2010–2013	**B.Sc.**, *Sri Venkateshwara University*, Tirupati, *81.66%*. Distinction: Mathematics, Physics, Chemistry
2008–2010	**HSC**, *BIEAP*, Andhra Pradesh, *76.1%*. Distinction: Mathematics, Physics, Chemistry
2008	**SSC**, *Andhra Pradesh*, *84.00%*. Distinction

Doctoral thesis

Title	*Spin Manipulation in Functional Materials: Study From First Principles*
Supervisor	Dr. Kartick Tarafder, Assistant Professor, National Institute of Technology Karnataka, India

Master thesis

Title	*Synthesis and Magnetic Properties of NiO Nanoparticles*
Supervisor	Dr. S. Angappane, Scientist D, CeNS, Bangalore, India

Expertise

Simulations:

- Density Functional Theory Calculations using Gaussian, Quantum Espresso, and VASP

Synthesis techniques: Nanoparticle Synthesis using Sol-Gel method

Charecterization:

- X-ray diffraction
- UV-Visible Spectroscopy

Work Experience

- Research Outreach Intiatiove Studentship (ROIS), at Centre for Nano and Soft Matter Sciences, Bangalore 04 January, 2016 – 04 April,2016

Research Interest

- Condensed Matter Physics
- Spintronics

Publications

1 **Indukuru Ramesh Reddy**, Peter M. Oppeneer, and Kartick Tarafder 'Route to achieving giant magnetoelectric coupling in $\mathrm{BaTiO_3/Sr_2CoO_3F}$ perovskite heterostructures' **Physical Review B** (2018) 98, 140401.

2 **Indukuru Ramesh Reddy**, Peter M. Oppeneer, and Kartick Tarafder 'Interfacial Spin Manipulation of Nickel-Quinonoid Complex Adsorbed on Co(001) Substrate' **Magnetochemistry** (2019) 5(1), 2.

3 **Indukuru Ramesh Reddy** and Kartick Tarafder 'Theoretical Investigations of Electronic Structure, Magnetic and Optical Properties of Transition Metal-dinuclear Molecules' **ACS Omega** (2020) 5(38), 24520.

4 **Indukuru Ramesh Reddy**, Peter M. Oppeneer, and Kartick Tarafder 'Pressure driven spin-state and structural transformation in a Hofmann clathrate coordiantion polymer' **Journal of Magnetism and Magnetic Materials** (2021) 524, 167637.

5 **Indukuru Ramesh Reddy** and Kartick Tarafder 'An unexpected spin-state switching and anti-ferromagnetic coupling in a Ni^{II}-dinuclear molecule chemisorbed on a Co(001) substrate' **(Under Review)**

6 Soumitra Payra, Swapna Challagulla, **Ramesh Reddy Indukuru**, Chanchal Chakraborty, Kartick Tarafder, Balaram Ghosh and Sounak Roy 'The Structural and Surface Modification of Zeolitic Imidazolate Framework Towards Reduction of Encapsulated CO_2' **New Journal of Chemistry** (2018) 42, 19205.

7 Sunil Kumar Nechipadappu, **Indukuru Ramesh Reddy**, Kartick Tarafder, and Darshak R. Trivedi 'Salt/Cocrystal of Anti-Fibrinolytic Hemostatic Drug Tranexamic acid: Structural, DFT, and Stability Study of Salt/Cocrystal with GRAS Molecules' **Crystal Growth & Design** (2019) 19(1), 347.

Conferences/Workshops/Seminars

- "Spin State Manipulation of Nickel Quinonoid by Chemisorbed to a Co(001) Substrate" in Theory Meets Experiment in Low-Dimensional Structures with Correlated Electrons, July 1-4, 2019 at Prague, Czech Republic. **(Contributed talk)**

- "Pressure driven structural transformation associated with spin-state switching in a Hofmann clathrate" in Spins in Molecular System: Experiment, Theory and Applications (SiM-2019), December 2-4, 2019 at Indian Institute of Science, Bangalore, India. **(Flash talk)**
- "Magnetoelectric Coupling in Barium Titanate/Cobalt oxyhalide heterostructure" in 30th Annual General Meeting of MRSI and the First Indian Materials Conclave, February 12-15, 2019 at Indian Institute of Science, Bangalore, India. **(Poster presentation)**
- Participated in Indo-US symposium on Recent advances in magnetism and spintronics, February 5-6, 2018 at IIT Bombay, Bombay, India.
- Participated in "Short Course on Flexible Electronics" at IIT Kanpur, June, 2017
- Participated in 8'th Bangalore India Nano 2016 as a student delegate.
- Participated in three day workshop on "KNOW NANO-2016" at Central University of Karnataka, India.

Software Skills

- I have good knowledge of Origin and Latex
- I also have knowledge of Bash Scripting and HPC

Referees

1 Dr.Kartick Tarafder
Assistant Professor
Dept. of Physics, National Institute of Technology Karnataka, India
E-mail:kartick@nitk.edu.in, karticktarafder@gmail.com

2 Prof. Peter M. Oppeneer
Dept. of Physics and Astronomy, Uppsala University, Uppsala, Sweden
E-mail:peter.oppeneer@physics.uu.se

3 Dr. Rajeev Shesha Joshi
Assistant Professor,
Dept. of Physics, Central University of Karnataka, India
E-mail: rajeevsj@cuk.ac.in

4 Dr. S. Angappane
Scientist D
Centre for Nano and Soft Matter Sciences, Bangalore, India
E-mail:angappane@cens.res.in